DISSERTATION

EXPLORING POST-COLD FRONTAL MOISTURE TRANSPORT IN AN IDEALIZED EXTRATROPICAL CYCLONE STUDY

Submitted by

Amanda Marie Sheffield

Department of Atmospheric Science

In partial fulfillment of the requirements

For the Degree of Doctor of Philosophy

Colorado State University

Fort Collins, Colorado

Spring 2016

Doctoral Committee:

Advisor: Susan C. van den Heever

Richard Eykholt
Richard Johnson
Sonia Kreidenweis

ABSTRACT

EXPLORING POST-COLD FRONTAL MOISTURE TRANSPORT IN AN IDEALIZED EXTRATROPICAL CYCLONE STUDY

Moisture transport in extratropical cyclones (ETCs) has been studied in the past in the context of the warm conveyor belt (WCB), a 'conveyor belt' transferring moisture from the warm sector boundary layer to the free troposphere both eastward and poleward of the warm front. Recent research has highlighted a different, potentially important mechanism of transporting water vapor in ETCs by post-cold frontal (PCF) clouds. PCF clouds are typically boundary layer cumulus clouds located in the cold sector of an ETC that transfer moisture to the free troposphere through convective-evaporative processes. Recent studies have suggested that these PCF cumuli may vertically transport nearly equivalent amounts of moisture as the WCB. Therefore, not only are these PCF cumuli important in venting the PCF boundary layer, they also play a role in limiting the amount of moisture available for convergence in the source region of the WCB. This limitation can have important consequences for regional weather and climate through its impact on the timing and location of precipitation, the three-dimensional redistribution of water vapor, and the distribution of clouds within ETCs.

The goal of this study is to investigate the role of PCF clouds in the moisture transport of an ETC, and the impacts of environmental factors such as SST and aerosol loading on this transport role. We have achieved this goal through the use of numerical simulations of such a storm system. Previous studies have utilized model simulations with relatively coarse grid resolutions and convective parameterization schemes. Here, we simulate a wintertime ETC over

the Pacific Ocean using high spatial and temporal resolution, advanced microphysics and explicitly resolved convection.

The results of this research demonstrate that PCF cumuli are found to vertically ventilate BL moisture over an expansive region behind the cold front. The free tropospheric moisture contents and stability profile of the cold sector exert a strong control over the size, depth and frequency of the PCF clouds, and varies with distance from the cold front.

Increased aerosol loading results in the invigoration of the PCF clouds. This is associated with an increase in the upward vertical moisture flux, increased cloud condensate formation, and reduced precipitation rates. Sea surface temperature is found to be a significantly more important factor in the development of PCF cumuli than aerosol loading, where increasing SSTs are associated with increased cloud fraction, cloud top heights, and precipitation rates. The impact of PCF clouds on vertically redistributing water vapor from the cold sector is found to depend in varying degrees on the large-scale advection of water vapor by the ETC system, the surface evaporation rates, the updraft velocities, the precipitation rates, and the cloud fraction within the PCF region.

The pathways of the vertically redistributed water vapor within the ETC were then examined through the use of massless, passive tracers. The results of these experiments show that the water vapor lofted out of the PCF BL by the cumulus clouds is advected hundreds of kilometers eastward within 8-12 hours of release of tracers in the PCF BL. Furthermore, cross frontal transport from behind the cold front to the WCB source region appears to be small, in contradiction to previously hypothesized results. This is due to the fact that the cold frontal boundary provides a zone of strong vertical lifting that does not allow tracers to converge further east.

ACKNOWLEDGEMENTS

First and foremost, I would like to acknowledge my advisor Professor Susan C. van den Heever for helping me produce this work. This research would not have been possible without her and her support and guidance of my academic development. I am additionally grateful to Sue for allowing me to pursue my interests in science policy, communication, and outreach during my time at CSU. I leave CSU not only with a PhD degree and a suite of research experience, but also the skills to communicate and translate the importance and societal relevance of our science due to her support. I would also like to thank the members of the van den Heever research group, past and present, for their assistance, including with the RAMS model. I have been at CSU since the early years of the van den Heever research group and have seen it grow and flourish due to the incredibly talented people in the group.

I next would like to thank my family, especially my husband Jesse. They have been a constant source of encouragement and understanding during this time. Jesse is the best partner in life I could ever have, and is a constant source of support and inspiration.

Lastly, I would like to thank my PhD committee, Sue and Professors Sonia Kreidenweis, Richard Johnson, and Richard Eykholt for their review of my dissertation and its results. Their patience and support over the years, especially in the last year, have been important in formulating these results and my future career.

This work was jointly supported by a fellowship through the Department of Energy (DOE) Office of Science Graduate Fellowship (SCGF) (2011-2013) and by NASA under grant NNX13AQ33G.

TABLE OF CONTENTS

LIST OF TABLES

LIST OF FIGURES

1. INTRODUCTION

Extratropical cyclones (ETCs) serve as major poleward transporters of moisture and energy. They are driven by global baroclinic waves that form due to Earth's need to transfer energy between the tropics and poles (e.g. Hartmann 1994). Consequently, they serve as a primary source of precipitation in the mid-latitudes (Stewart et al. 1998; Catto et al. 2012) and have large impacts on the Earth's radiation budget (Harrison et al. 1990). Past studies (see the reviews of Newton and Holopainen 1990 and Shapiro and Gronas 1999) have focused on the location, timing, and intensity of the precipitation produced by ETCs as many of the most-populated regions around the world are dependent on the distribution of mid-latitude weather and climate for their water resources. Enhancing our understanding of the processing of water by ETCs, and the impacts of the environment on such processing, is therefore important to effective regional water management and planning.

Recent studies have suggested possible shifts in ETC storm tracks with changing climates (Yin 2005; Bengtsson et al. 2006, 2009; Graff and LaCasce 2012; Barnes and Polvani 2013; Graff and LaCasce 2014; IPCC 2013; Feser et al. 2015), with potentially dire consequences for the supply of water to highly populated regions. However, climate models struggle to accurately represent the features of ETCs, including the warm conveyor belt (WCB). For example, Naud et al. (2010) found much lower ETC cloud fractions in a GCM when compared with observations as a result of vertical velocities that were too weak, and Catto et al. (2010) identified differences in the development of ETC features when comparing global reanalyses and GCM output. Ceppi et al. (2012) highlighted how significant biases in short wave cloud forcing in CMIP5 models can alter the location of the midlatitude jet while recent work by Schafler and Harnisch (2015)

found that slight differences occurring in association with various data assimilation methods in the relative humidity of the WCB source region have a large impact on the potential vorticity (PV) structure of developing cyclones. Enhancing our understanding of ETCs, their transport of water and energy, and the processes impacting such transport is therefore needed to better represent these systems in GCMs and hence enhance our predictions of these storm systems, their changes with a changing climate, and the associated shifts in precipitation.

1.1 STRUCTURE OF EXTRATROPICAL CYCLONES

The first conceptual model of an ETC was introduced before the age of dense observational networks on the ground and from space (Bjerknes and Solberg 1922) (figure 1.1). As an observable portion of Earth's synoptic weather patterns, ETCs are responsible for much of the atmospheric variability on this scale (Trenberth 1991). Driven dynamically by planetary and synoptic scale Rossby waves and the jet, ETCs develop warm and cold fronts at air mass boundaries in association with the cyclonic rotation of air around the ETC's low-pressure center (figures 1.1 and 1.2). Various cloud types and precipitation intensities are associated with these frontal air mass boundaries (Hobbs 1978; Hobbs et al. 1980; Matejka et al. 1980; Houze and Hobbs 1982; Ryan 1996; Catto et al. 2012).

A number of synoptic scale flow patterns are associated with ETCs. The WCB (e.g. Browning 1971; Carlson 1980; Browning 1986) is a 'conveyor belt' that transfers water from the boundary layer (BL) in the ETC warm sector to the free troposphere both aloft and poleward of the warm front (Figure 1.2). The mid-to-upper tropospheric WCB trajectory can turn anticyclonically or cyclonically in association with the upper level westerlies or with the rotation of the cylone, respectively. The cold conveyor (CCB) (Schultz 2001) typically originates in the low altitude cold air poleward of and below the warm front, and rises poleward of the cyclone

center, where once again the flow can turn cyclonically or anticylonically. The dry conveyor belt (DCB), or dry intrusion, (Browning 1997) is composed of eastward sinking air trajectories behind the cold front that dry the air equatorward of the ETC center (figure 1.2). Once the DCB reaches the cold front, the flow fans out both poleward and equatorward.

Mesoscale circulations and cloud characteristics are also driven, in part, by the large-scale dynamics of the cyclone (Hobbs et al. 1980), although this relationship is certainly not unidirectional. For example, mesoscale moisture transport and cloud processes can contribute to cyclogenesis (Smagorinsky 1956; Krishnamurti 1968; Tracton 1973; Chang et al. 1982; Reed et al. 1988; Kuo et al. 1991; Davis 1992; Whittaker and Davis 1994; Stoelinga 1996) and frontal evolution (Baldwin et al. 1984; Dudhia 1993; Wernli and Davies 1997; Martin and Otkin 2004; Posselt and Martin 2004; Reeves and Lackmann 2004; Igel and van den Heever 2014) through latent heat release and the production of positive PV anomalies. Interactions across spatial scales are also evident in the BL ventilation associated with these systems in which BL circulation and cloud processes loft water (Boutle et al. 2010; 2011), aerosols (Cotton et al. 1995; Sinclair et al. 2008), and other trace gases (Arnold et al. 1997; Stohl and Trickl 1999; Stohl et al. 2003) to the mid and upper troposphere, where it may be advected by large-scale westerly flow.

1.2 MOISTURE TRANSPORT IN EXTRATROPICAL CYCLONES

Synoptic scale moisture transport from the tropics to subtropics has been studied primarily in the context of ETCs in addition to relatively narrow streams of water vapor called atmospheric rivers (Zhu and Newell 1994; Knippertz and Martin 2007; Knippertz and Wernli 2010; Dacre et al. 2014). While atmospheric rivers can be associated with the synoptic scale flow of ETCs, the availability of moisture for transport by the primary ETC features is dependent on several factors that vary across the expansive ETC cloud system. As an ETC develops, distinct

warm and cold sectors form that are characterized by substantially different large-scale moisture contents and temperature structures. Further evolution of the BL moisture and temperature field occurs in association with surface latent and sensible heat fluxes via enhanced air-surface interactions (Neiman et al. 1990; Berger and Friehe 1995; Gutowski and Jiang 1998; Field and Wood 2007; Boutle et al. 2010). For example, the advection of warm air over a relatively cool ocean surface in the ETC warm sector can result in the transfer of water vapor back to the sea surface through condensation, in a process similar to the formation of dew over land (Boutle et al. 2010). Behind the cold front, the advection of cold air over a relatively warm sea surface promotes latent and sensible heat fluxes from the ocean to the atmosphere. The development of shallow convective clouds in association with the enhanced atmospheric instability in the latter case can strengthen the evaporation of water vapor through low-level gustiness.

While the limited width of atmospheric rivers can cause intense precipitation in localized regions, the WCB (Browning 1971; Carlson 1980; Browning 1986) broadly lifts large quantities of BL water vapor mass from the ETC warm sector over the warm frontal region (figure 1.2). Modeling studies have found that the processing of water vapor by the WCB is highly efficient - at times 100% of the BL water vapor mass entering the WCB trajectory is converted into WCB precipitation (Eckhardt et al. 2004; Boutle et al. 2011) (figure 1.3).

Recent research by Boutle et al. (2010; 2011) (B10; B11) explored the three-way interaction between the sea surface, BL moisture, and ETC dynamics. While sea surface fluxes provide a water vapor source throughout all of the sectors of maritime ETCs, other processes such as vertical advection, horizontal convergence, turbulence, and vertical transport by shallow convection can modify the horizontal and vertical distribution of BL-lower free troposphere moisture content. In a simulation of an idealized ETC, B10 found that the source of BL water

vapor for transport by the WCB (figure 1.4a) was from other ETC regions and converged in the warm sector (figure 1.4b). One source of water vapor feeding this warm sector convergence was found to be the region behind the cold front, or the post-cold frontal (PCF) region. B10 showed that the PCF BL water vapor generated through surface evaporative processes diverges within the BL from the PCF region (figure 1.4b), from where it is transported towards the WCB source region. Turbulence at the BL top was found to be less important in ventilating water vapor vertically out of the BL than this horizontal convergence-WCB process (figure 1.4c).

In addition to the horizontal divergence within the BL, B10 identified another mechanism important to BL water vapor transport that occurs in association with shallow convection (figure 1.4d). PCF cumulus clouds are typically not directly forced by the cold front, and are of smaller vertical extent than the cold frontal convection. They form due to the atmospheric instability arising from the advection of the cold air mass behind the cold front over a relatively warm ocean surface (Neiman et al. 1990; Neiman and Shapiro 1993). While PCF clouds can occur in many locations and seasons, satellite studies have found that they occur more frequently during northern hemisphere winters (Naud et al. 2015a) (figure 1.5). Satellite studies also suggest that these cloud fields precipitate on average between 0.1-0.4 mm hr^{-1} (Naud et al. 2015a) and are likely to contain supercooled water or be mixed phase (Naud et al. 2015b).

PCF cumulus clouds therefore appear to transport large amounts of moisture from the BL to the free troposphere through convective-evaporative processes (Bond and Fleagle 1988; Weusthoff and Hauf 2008; B10; B11). As such, PCF cumulus clouds play a similar role to that of tropical clouds of similar size, such as trade wind cumulus and cumulus congestus clouds, in the redistribution of water vapor and the subsequent moistening of the environment (Johnson et al. 1999).

B10, and later B11, found that the cumulative vertical lofting of water vapor out of the BL by shallow convection in the PCF region (figure 1.4d) to be as nearly as large as the WCB ascent (figure 1.3). And, once ventilated from the BL to the free troposphere, the PCF water vapor is then available to be transported above the BL, including eastward towards the cold front. B11 confirmed this transport mechanism in their GCM simulations of an idealized ETC by releasing surface based, massless tracers. These tracers were advected by both large-scale circulation and the convective parameterization scheme. They found an accumulation of the tracers behind the cold front and above the BL, near 3 km ASL (figure 1.6). The tracers were vertically ventilated by the PCF clouds from where they were transported eastward. Hence, two moisture transport mechanisms are competing in the PCF region according to their study: the vertical transport out of the BL by PCF clouds and the horizontal divergence of water vapor within the BL to the WCB source region.

B10/B11 produced a new conceptual model that emphasizes the relative importance of BL moisture sources in supporting the large-scale ETC moisture transport. Figure 1.7 is a schematic from the Boutle et al. studies representing the flow of moisture within and out of an ETC BL. Black arrows represent horizontal advection within the BL while grey arrows represent sinks of BL moisture. The role of: (1) convergence of readily available moisture from other ETC sectors (such as the PCF) to the WCB source region, and (2) the cumulative PCF shallow convective moisture ventilation in the redistribution of water vapor with an ETC system are evident in this figure.

While B10 made novel discoveries into the transport of water vapor in ETCs, use of a coarse global model (0.4^{o} resolution) along with convective parameterization schemes, meant that they were unable to fully explore the cloud, mesoscale, and BL water vapor transport

mechanisms. For example, they were not able to consider the importance of the cloud microphysical and dynamical processes leading to the PCF cloud updraft structure (and associated vertical water vapor mass flux), the loss of water mass through the production of precipitation, or how these processes might change with changing environments. The focus of the research presented here is on the role of PCF cumulus clouds and their associated processes in transporting water through ETCs. We will examine these transport mechanisms in more detail using a cloud-resolving model (CRM) with high spatial and temporal resolutions. We will also examine the impact of several environmental factors on these cloud-scale mechanisms, including sea surface temperature (SST) and aerosol loading, as both of these factors could be expected to impact the convective-evaporative-precipitation processes of PCF cumulus clouds.

1.3 ENVIRONMENTAL FACTORS IMPACTING EXTRATROPICAL CYCLONES

Several previous studies have examined the role of sea surface temperature (e.g. Field and Wood 2007) and aerosol pollution (e.g. Igel et al. 2013) on synoptic scale features of ETCs. We will examine the impacts of these environmental conditions on some of the cloud scale features. Two factors potentially important to cumulus clouds are: (1) the temperature and moisture of the BL in which they form, which is strongly determined by the SST in maritime cloud systems; and (2) the rate at which they precipitate, which is influenced in part by the aerosol loading of the atmosphere.

A. SEA SURFACE TEMPERATURE

If SSTs increase in the future due to anthropogenic warming, ETCs could be fewer in number and/or more intense (Field and Wood 2007). A consensus on the impacts of a changing climate on ETC strength and frequency has not been reached as ETC development also depends on the meridional temperature gradient (e.g. Inatsu et al. 2003; Bengtsson et al. 2006; Meehl et al.

2007), the sub-tropical jet and midlatitude storm tracks (e.g. Barnes and Polvani 2013), and midlatitude static stability (Frierson 2006). Increased ETC precipitation has also been simulated without increased ETC intensity, occurring simply due to the increase in total atmospheric moisture (Bengtsson et al. 2009). Current climate models are at a disadvantage in capturing ETC processes as cloud feedbacks are a major source of uncertainty (Stephens 2005), and ETC features are difficult to fully capture in models on the scale of climate models (Catto et al. 2010; Ceppi et al. 2012). Future global climate studies need a better understanding of SST-cloud relationships, including those of ETCs.

The impact of SSTs on ETCs has been found to be important due to its direct impact on atmospheric moisture content. SST exerts a strong control on the water vapor content of the BL in accordance with the Clausius-Clapeyron equation, which predicts a 7% increase in saturation vapor pressure per 1 K of atmospheric warming. Climate models have shown that this increase in water vapor does not necessarily equate to the same increase in precipitation. Recent studies have suggested changes to global precipitation of ~2% K^{-1} (Trenberth 2002; Held and Soden 2006) as the global distribution of convective mass flux, horizontal moisture transport, radiative fluxes, and the evaporation-precipitation patterns will also change in association with atmospheric temperature changes.

The impacts of changing SSTs on surface sensible and latent heat fluxes will in turn influence convective and BL processes. Convective processes could subsequently impact these fluxes through subsequent mesoscale low-level gustiness feedbacks. The magnitude of these fluxes varies by ETC and sector and, as discussed above, can influence the moisture interactions between the warm and cold sectors. The influence of SST on clouds at the mesoscale can thus feed upscale. Understanding the impacts of SST on the PCF clouds and their subsequent

moisture supply to the broader scale ETC system will enhance our understanding of the role of PCF clouds in different atmosphere thermodynamical regimes.

B. CLOUD NUCLEATING AEROSOL

Aerosol impacts on ETCs have been examined previously. For example, previous studies have analyzed aerosol indirect effects on a warm front (Igel et al 2013), the intensification of the Pacific storm track within a GCM (Wang et al. 2014), and a simulated continental winter cyclone (Thompson and Eidhammer 2014). These studies have all demonstrated the impact of aerosols on cloud and ice water contents, latent heating, and precipitation processes associated with frontal regions. In the warm frontal region, Igel et al. (2013) found a shift from riming to vapor dominated processes in warm frontal clouds as aerosol concentrations were increased, while Thompson and Eidhammer (2014) attributed a shift in the location of precipitation to aerosol-induced changes in mixed-phased clouds. These previous studies focused primarily on the impact of aerosols on fronts and more broadly within continental cyclones. However, we are interested in the role of maritime PCF clouds on water vapor transport. We will therefore be examining aerosol impacts on these cloud types.

1.4 SCIENTIFIC GOALS

The goal of this study is to examine the role of PCF clouds in the moisture transport of an ETC, and the sensitivity of the moisture transport by these cumulus clouds to changes in various environmental factors, specifically SST and aerosol loading. Previous studies of ETC moisture transport that highlighted the role of the PCF region utilized coarse model resolutions (0.4^{o}) and convective parameterizations to examine an idealized ETC (B10; B11). Here we extend the Boutle et al. studies by examining an idealized case study simulation of a wintertime ETC over

the Pacific Ocean using a CRM with high temporal and spatial resolutions, that incorporates advanced microphysical processes, and that resolves convection on its finest grids.

This study aims to answer the following questions:

1. What are the microphysical, dynamical, and latent heating characteristics of PCF clouds and how do they vary with environmental conditions?
2. What is the impact of SST and cloud nucleating aerosol on the BL ventilation of water vapor in the PCF cloud region of ETCs?
3. How is water vapor that is ventilated by the PCF region transported throughout ETCs?

The outline of this dissertation is as follows: first, we will describe the case study and cloud resolving model setup and experiments (Chapter 2). Then, results from the model simulations will be presented. We will first examine the average PCF cloud microphysical and dynamical characteristics, including the sensitivity of these characteristics to changes in SST and aerosol loading (Chapter 3), followed by an assessment of the cumulative impacts of PCF clouds on the PCF regional water vapor budget (Chapter 4). Then, using passive massless tracers we will determine how PCF ventilated moisture is transported within an ETC and compare this to moisture ventilation of other ETC sectors (Chapter 5). Lastly, we will provide a discussion and conclusion of the results of this dissertation (Chapter 6).

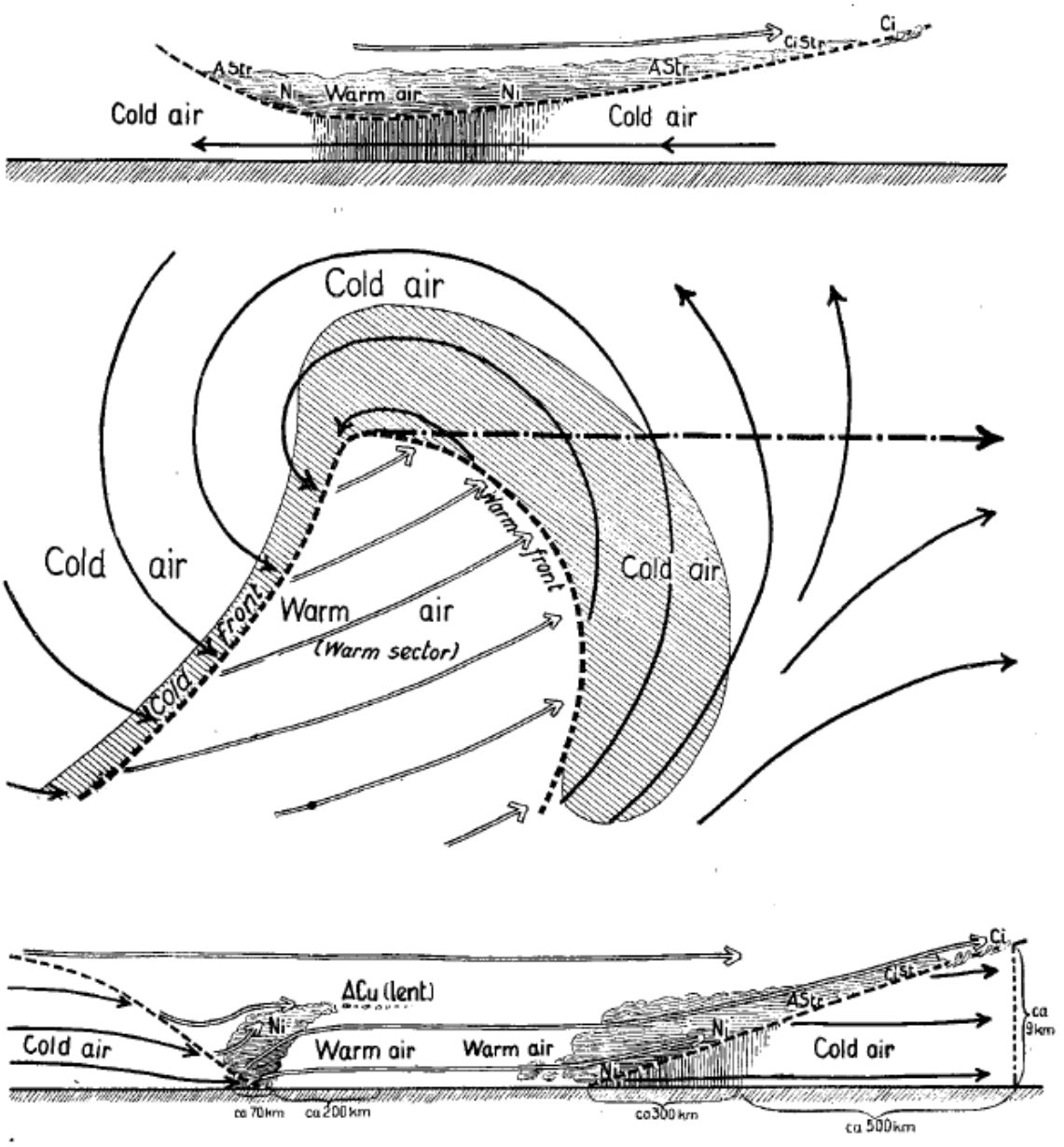

Figure 1.1: Illustration of frontal clouds and precipitation in the Norwegian Cyclone Model, as conceptualized in Bjerknes and Solberg (1922).

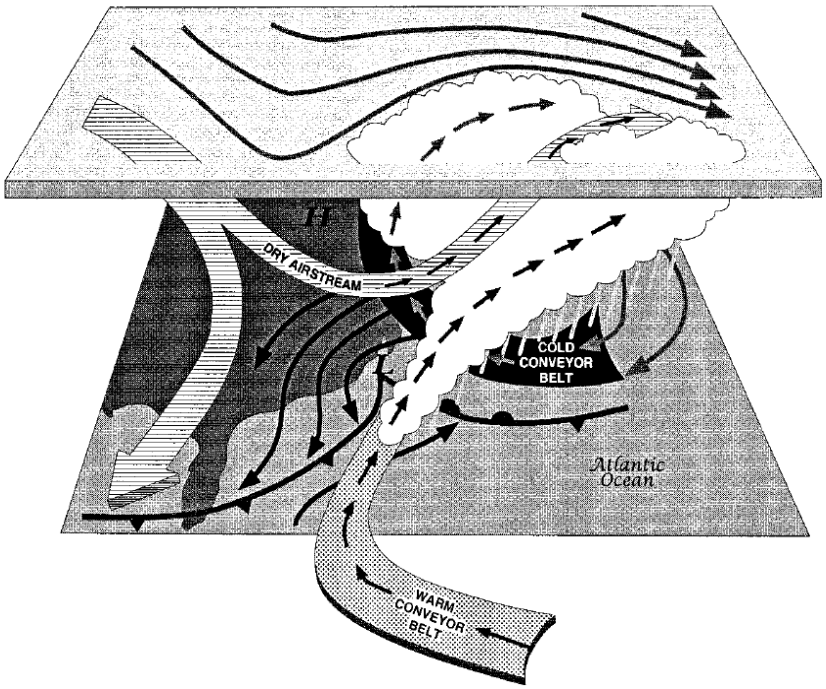

Figure 1.2: The conveyor belt model of airflow through a northeast US snowstorm (from Schulz 2001, adapted from Kocin and Uccellini (1990) and based on the Carlson (1980) conceptual model).

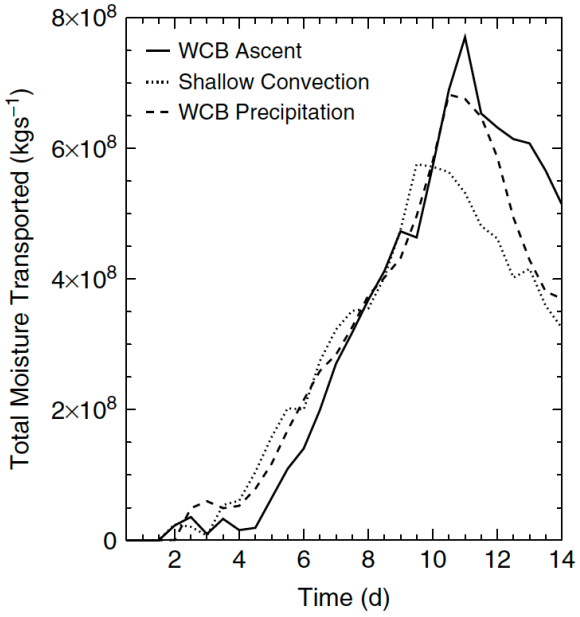

Figure 1.3: Time series of total moisture ventilated from the boundary layer of a simulated ETC by the warm conveyor belt ascent (solid) and shallow convection (dotted). Also shown is the surface precipitation rate from the warm conveyor belt (dashed) (after Boutle et al. 2011).

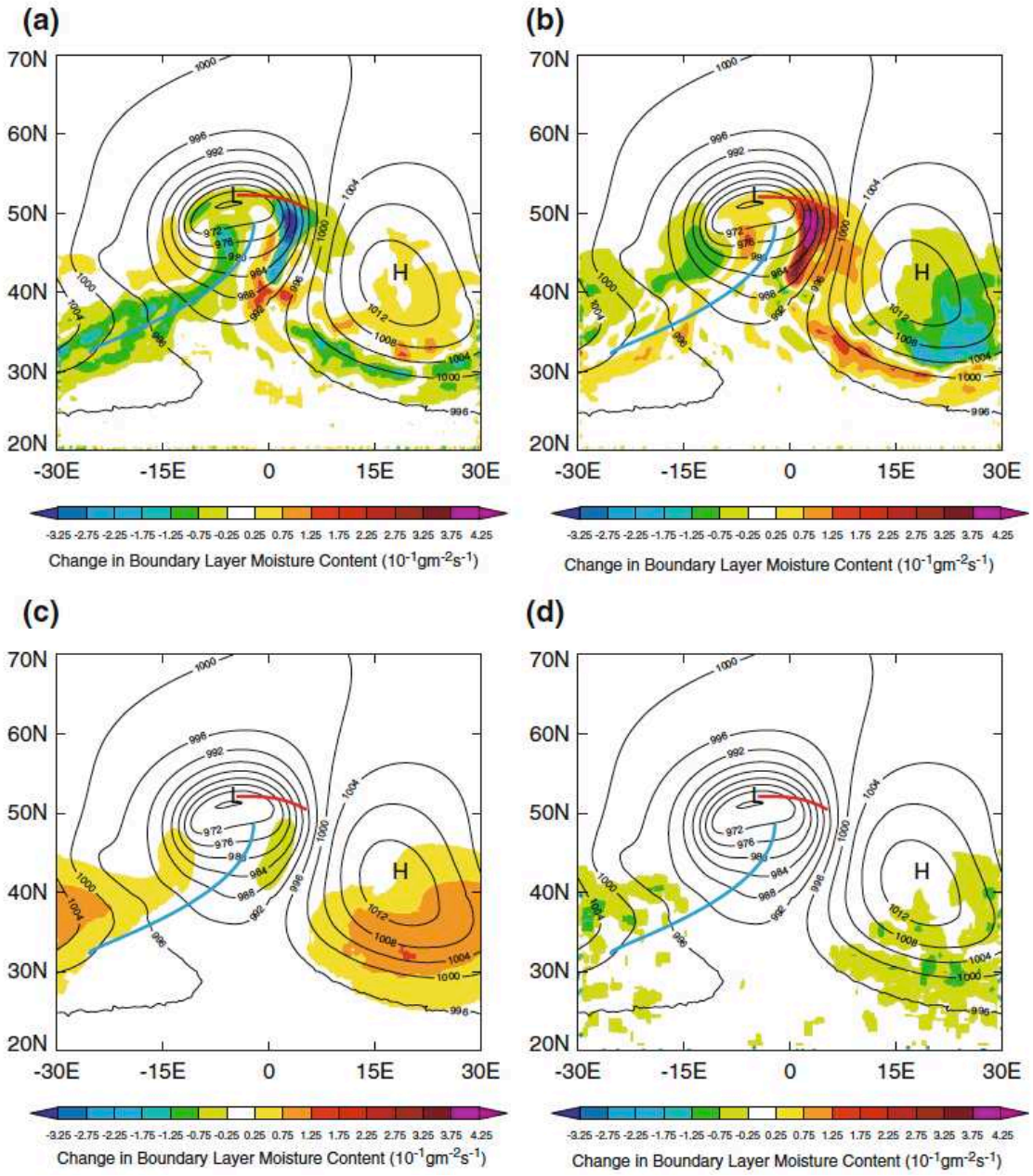

Figure 1.4: Tendencies in boundary layer (BL) moisture content (shaded) at day 7 of an idealized extratropical cyclone (ETC) simulation due to (a) vertical advection across the BL top, (b) horizontal divergence within the BL, (c) net vertical transport by BL turbulence, and (d) vertical transport by shallow convection. The pressure at mean sea level is shown by the black contours (contour interval of 4 hPa) (after Boutle et al. 2010).

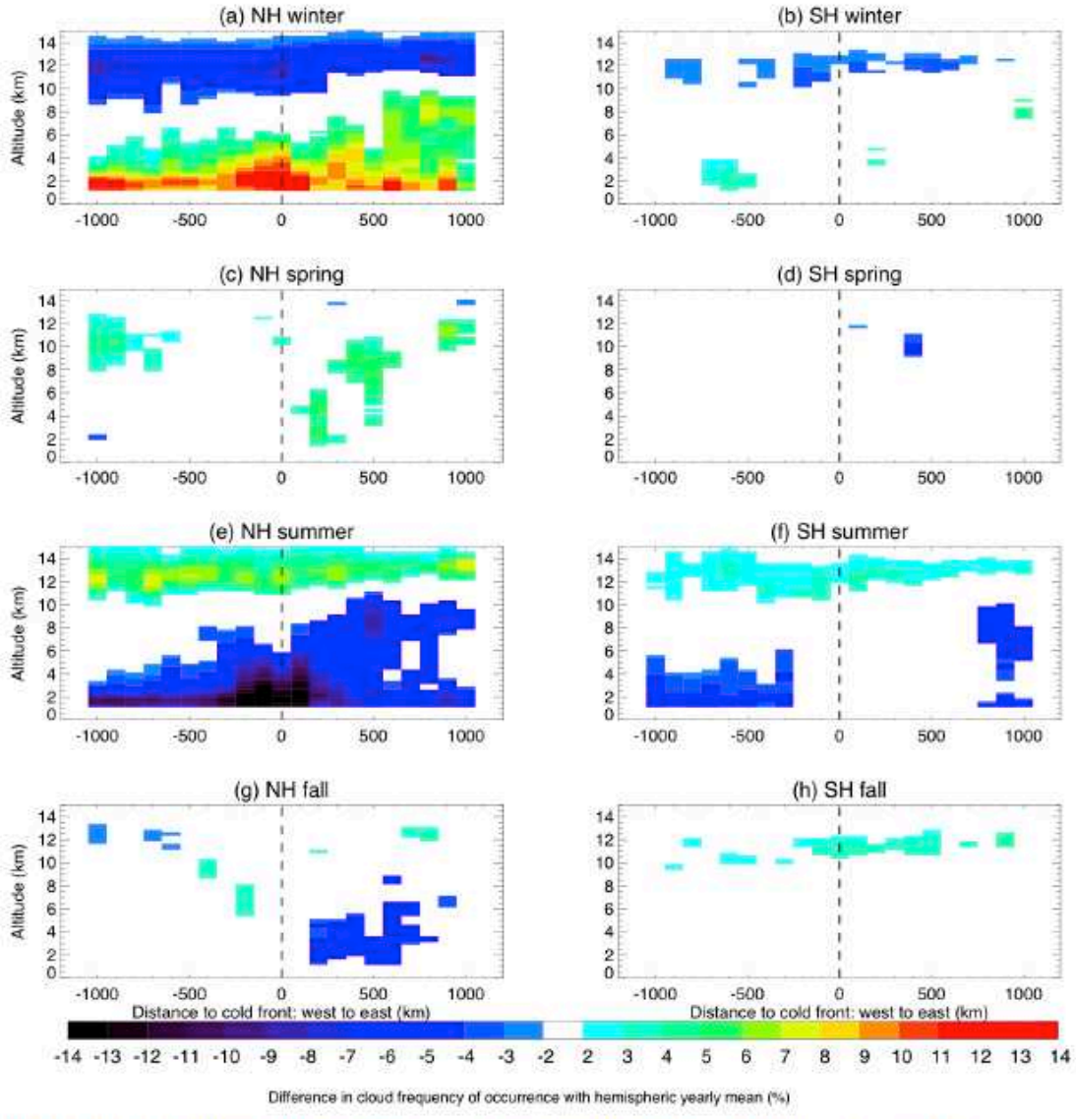

Figure 1.5: Difference in cloud frequency occurrence between the mean per season (winter, spring, summer, fall) and the yearly mean per hemisphere, for northern (NH) (a,c,e,g) and southern (SH) (b,d,f,h) hemispheres. The vertical dashed lines indicate the location of the surface cold front. Notice the increased frequency of NH winter lower atmosphere cloud frequency, including to the west of the cold front (after Naud et al. 2015a).

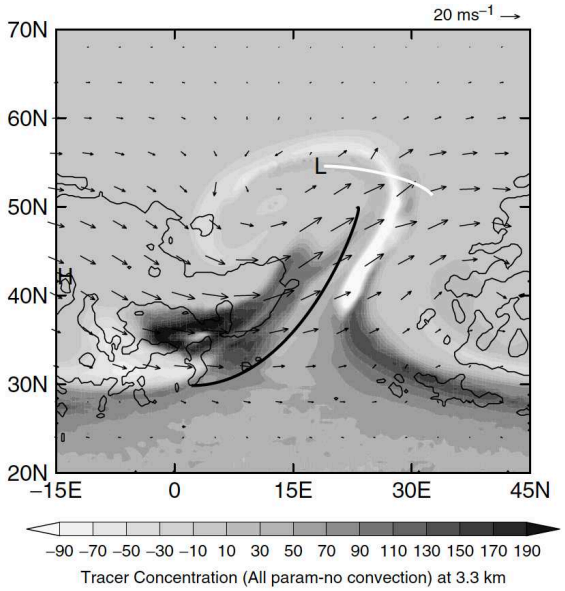

Figure 1.6: Tracer concentration (arbitrary unit) ventilated by convection at 3.3 km (shading), with wind vectors at 3.3 km, at day 9 of an idealized ETC convective parameterization simulation. Regions of cumulus-capped boundary layers are marked by thin black lines, with the warm/cold fronts also shown by thick white/black lines (after Boutle et al. 2011).

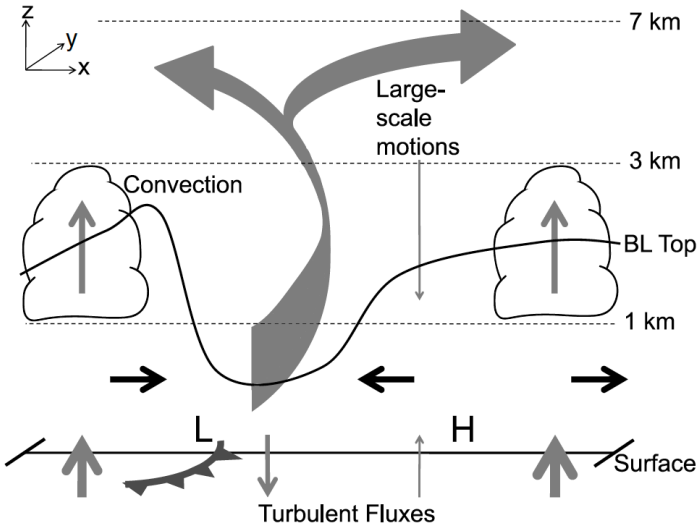

Figure 1.7: A schematic representing the flows of moisture within the cyclone boundary layer. Grey arrows represent sources and sinks of boundary layer moisture and black arrows represent advection within the boundary layer. The arrow thickness provides a qualitative indication of the relative strength of the various flows. L and H denote the low- and high-pressure centers respectively, with the cold front also marked. The approximate height of features is marked, along with the height of the boundary layer (after Boutle et al. 2011).

2. THE ETC CASE STUDY AND MODEL SETUP

2.1 CASE STUDY SELECTION AND SYNOPTIC OVERVIEW

The wintertime ETC case study selected for this study occurred in mid-January 2010 over the northern hemispheric portion of the Eastern Pacific Ocean. A wintertime case study was chosen as PCF clouds are found to occur more frequently in the northern hemisphere winter (Naud et al. 2015a). A visible satellite image of the ETC simulated here is shown in Figure 2.1. The storm formed in the western-to-central Pacific Ocean near 30^{o}N on 10 January 2010, and persisted for several days before reaching the western coast of the United States on 16 January 2010. The typical 'comma head' shaped cloud associated with ETCs is evident in Figure 2.1 and was associated with a strong 300-hPa jet (80-90 m s^{-1}) on the eastern edge of an upper level trough (figure 2.2a). Well-defined cold and warm fronts developed in association with this storm (figure 2.2b), and an extensive field of PCF cumulus clouds occurred behind the cold front (figure 2.1).

Sources of aerosol particles over the Pacific Ocean include those from Asian dust events and anthropogenic pollution (Kaufman et al. 2002; Sassen 2002; Fan et al. 2014; Ralph et al. 2015). The ocean may also act as a source of aerosols impacting these storms, especially in regions of high wind speed near the ETC center (Woodcock 1953; Lewis and Schwartz 2004; Grandey et al. 2011). Obtaining observations of the aerosol loading that occurred during this case study proved difficult. The location of the storm over the ocean means that ground-based aerosol observations are not available. While satellite observations from platforms such as MODIS (Salomonson et al. 1989) do provide aerosol optical depth (AOD) (Remer et al. 2005) over the ocean, they can only provide this information accurately for cloud free atmospheres. MODIS

AODs in the regions surrounding the observed storm were on the order of 0.2 (figure 2.3), however, it is once again emphasized that these concentrations are only representative of the ambient, cloud-free environmental conditions, and not necessarily of the number of aerosols actually entering the storm system. The difficulty in obtaining aerosol observations for these case study simulations is, however, somewhat offset by the fact that the aerosol sensitivity tests conducted for this study were performed over a range of aerosol concentrations in order to assess how such storms respond to both clean and polluted conditions.

2.2 MODEL SETUP

The cloud-resolving model chosen for this study is the Colorado State University Regional Atmospheric Modeling System (RAMS, Cotton et al. 2003; Saleeby and van den Heever 2013). RAMS has been used previously to conduct cloud-resolving simulations of ETCs (Igel et al. 2013; Igel and van den Heever 2014), as well as for simulating the aerosol impacts on cumulus and stratocumulus clouds (Saleeby et al. 2010; van den Heever et al. 2011; Saleeby et al. 2015; Sheffield et al. 2015). RAMS' advanced microphysics consists of a bin-emulating two-moment bulk scheme that predicts mixing ratio and number concentration of seven hydrometeor species. Microphysical processes represented by the scheme include cloud nucleation, ice nucleation, vapor deposition, evaporation, collision-coalescence, melting, freezing, sedimentation, and secondary ice production (Meyers et al. 1997; Saleeby and van den Heever 2013). The bin-emulating scheme uses offline tables created using a Lagrangian parcel model to determine the activation of aerosol particles based on a range of environmental conditions including the vertical velocity, temperature, aerosol concentration, and aerosol size (Heymsfield and Sabin 1989; Feingold and Heymsfield 1992). Other processes also utilize the results of the

parcel model and associated look-up tables including collision-coalescence, riming, and sedimentation.

Two different sets of RAMS simulations will be examined here. The first set included a multi-grid simulation of the ETC case described above, along with several SST and aerosol sensitivity simulations. The second set of simulations utilized a high-resolution single grid simulation of the ETC and included several sources of surface passive tracers to compare PCF convective transport with other regions of the synoptic scale ETC.

A. SST AND AEROSOL SENSITIVITY SIMULATIONS

Each model run in the first set of simulations utilized three nested grids (figure 2.4) and were identical to one another except for the environmental aerosol concentration and/or the magnitude of the SST throughout the domain. The outermost grid encompassed a significant portion of the northern hemisphere Pacific Ocean (256 x 170 grid points) and was run at 25 km resolution. Convection was parameterized using a generalized Kuo (1974) scheme (Molinari 1985). The remaining two grids were one-way nested and convection permitting. One-way nesting was used in order to prevent overemphasis of a specific region of the ETC. The second grid (642 x 477 grid points) had a horizontal grid resolution of 5 km and encompassed the ETC from initiation through mature development. The ETC was simulated for 36 simulation hours using only these two grids. This initial time period allowed for the initiation and development of the synoptic scale processes of the ETC. Once the system began to mature, a finer resolution third grid was included over the PCF region. This innermost grid (702 x 597 grid points) was centered on 34^{o}N, -153^{o}W. The horizontal resolution was set to 1 km. The cold front was initially located within this grid, but quickly exited the domain due to the eastward motion of the ETC, thus providing a scenario in which only PCF clouds were found in the third grid domain

and thereby facilitating the analysis of these cloud systems. Each model grid had 45 vertical levels, stretching from the surface to ~20 km with 10 levels in the lowest 1 km. The outermost grid was initialized using ECMWF reanalysis data (ERA-interim, 1.5^{o} resolution), and the lateral boundary conditions were nudged every 6 hours using these data.

All three grids were then simultaneously run for an additional 18 simulation hours, thus allowing the ETC and PCF region to mature. As the third domain over the PCF region was stationary, PCF clouds passed from west to east through the domain, and the atmospheric thermodynamic profiles varied in time. The PCF analysis presented in the following chapters will therefore first focus on the environment and clouds immediately behind the cold front, followed by the analysis of those clouds that occurred several hundreds of kilometers behind the cold front. The size of the Grid 3 domain (greater than 700 km in the east-west direction) facilitates such analysis.

Four simulations were completed in which various combinations of aerosol concentration and SSTs were utilized (table 2.1). The same background available ice nuclei (IN) concentration was used (0.01 cm^{-3} at the surface, decreasing exponentially with height) in all simulations. The number concentration of the aerosols available to serve as cloud condensation nuclei (CCN) was set to represent either clean or polluted conditions (figure 2.5). The aerosol number concentration at the surface was set to 120 cm^{-3} in the clean case and 1200 cm^{-3} in the polluted case. Above the surface, both the clean and polluted aerosol number concentrations decreased exponentially with height.

Aerosol sources or sinks were not utilized. This means that the aerosol number concentration (**N**) available serves as an upper nucleation limit in each grid box throughout the duration of the simulation. Based on predicted ambient conditions, a fraction of **N**, up to a

maximum of **N**, will activate. As the simulation progresses, the fraction of **N** actually activated will increase or decrease based on the newly, predicted ambient conditions. These ambient conditions could promote additional nucleation (up to **N** total activated aerosol) or instead cause evaporation (decrease the activated fraction of **N**). In this way, the ETC has **N** aerosols available at each time step for activation. Such an approach is useful because no new sources of aerosol were needed after the initiation of these long duration ETC simulations. However, shortfalls of this approach include the inability to examine the impacts of a specific source, such as the advection of pollution into a region.

Three different SST setups were used. First, a horizontally varying SST over the Pacific Ocean based on the January SST climatology provided with RAMS was used. The horizontal SST field (longitude vs. latitude) for Grid 2 is shown in figure 2.6. In the two SST sensitivity experiments this spatially varying climatological SST dataset was once again used, however the SST was uniformly increased or decreased by 2 K at all maritime locations. The horizontal gradients in SST therefore remained unchanged. This range of SSTs was chosen based on climate change warming trends and projections found in the most recent IPCC report (2013). While this SST sensitivity range is relatively large, in the chosen deviations in SST from the climatological SST allows for an assessment of the breadth of impacts due to SST. In addition, possible shifts in the ETC storm track could also vary the SSTs over which ETCs are forming. While the simulations here are not specifically addressing shifting storm tracks, the set of SST sensitivity simulations here can also be considered for such scenario. The initial simulation (CL in table 2.1) was completed using the lower aerosol concentration and the January climatological SSTs. The four experiments in table 2.1 then represent various combinations of these two aerosol concentrations and three SSTs. Comparison between the simulations will often be shown in

subsequent sections as a difference from the clean, climatological SST simulation (CL) which we refer to as the CONTROL simulation.

B. PASSIVE TRACER TRANSPORT SIMULATIONS

Similar simulations to those described in the previous section were then utilized to explore convective lofting and the horizontal advection of surface-based passive tracers, with slight modifications to the grid setup. RAMS was once again used, but this time with only one high-resolution, convection-permitting grid. This single grid was similar in size to Grid 2 in the previous set of simulations, and hence was large enough to contain the entire ETC through its mature development. However, this new single grid had an increased horizontal resolution of 2 km (1100 x 1500 grid points). The same number of stretched vertical levels (45) in the previous set of experiments was used. The aerosol distribution setup was the same in the simulations described in section 2.2A, and two of the four aerosol-SST simulations listed in Table 2.1 were once again performed using this grid, i.e., the CL and the +2KCL simulations. Only two SST experiments with passive tracers were performed as SST from the first set of experiments was found to be a relatively strong controlling factor of PCF clouds and their ventilation of the BL. Modifications to PCF clouds due to the presence of aerosol was found primarily to the precipitation processes. However, as the tracers being utilized are passive tracers, precipitation processes will not influence their distribution. Examination of the eastward and poleward transport of passive tracers released at the surface by the ETC and their lofting into the upper level synoptic scale ETC motions would thus be expected to be relatively similar between the CL and PO simulations (table 2.1).

Nudging at the lateral grid boundaries was no longer performed using ECMWF reanalysis data. Instead, a separate RAMS ETC simulation was completed on a larger grid

(similar to grid 1 in the simulations in sections 2.2A) using a 10 km horizontal resolution (640 x 425 grid points), and that encompassed a significant portion of the northern Pacific Ocean. The output from this simulation was then used to laterally nudge the 2-km grid simulation used for this analysis.

Using this single grid, simulations were run for 36 simulation hours after being initialized at 00UTC 12 January 2010. Six massless passive tracers were then placed in the single domain. These six tracers do not interact with each other, are available to be transported throughout the domain by advection, turbulence, convective motions, and diffusion without impacting the ETC cloud development, and are analyzed separately. No removal of the passive tracers from the domain occurs except at the grid domain edges, where the tracers can be advected out of the domain (Klemp and Wilhemson 1977).

Passive tracers were initiated at the surface in 5 different regions of the ETC. Figure 2.7 shows the initial location of these tracers. Two surface tracers were released in the PCF region (labeled as P1 and P2), while two additional surface tracers were released ahead of the cold front in the warm sector and ahead of the warm front (labeled as W3 and W4, respectively). A fifth tracer was released from the surface in the region to the northwest of the ETC center (labeled as TR5). The initial layer that each tracer was released from spans 100 km in the east-west direction and 250 km in the north-south direction and was initialized at the lowest model level. These passive tracers will be used to identify pathways of moisture transport, or similarly aerosol transport, within the ETC. These five tracers were not replenished with time.

An additional passive tracer (labeled as the SFC-TRACER) was released at the surface throughout the entire domain. After each time step the surface concentration of SFC-TRACER at the lowest model level was set to its initial value. Reinitializing the SFC-TRACER source at the

lowest model level will either reduce the number of tracers at the surface if the tracer transport is towards the surface, keep it the same if no tracer transport occurred, or replenish what tracers are lost to vertical lofting or mixing. As in the B11 studies, this setup is intended to emulate the transport of water vapor from the lowest atmospheric levels as winds and convection move water vapor throughout the domain, and the ocean surface acts as a continuous water vapor source. We chose not to vary the surface concentration based on variations in environmental characteristics.

Transport of all six passive tracers will first be examined for the CL simulation, followed by a comparison of the SFC-TRACER transport within the CL and +2KCL simulations.

Table 2.1: List of simulation names by description of the sea surface temperature and aerosol concentration used.

	Aerosol Concentration	
SSTs	**100 cm^{-3}**	**1000 cm^{-3}**
Climatology	CL	PO
Low (-2 K)	-2KCL	
High (+2 K)	+2KCL	

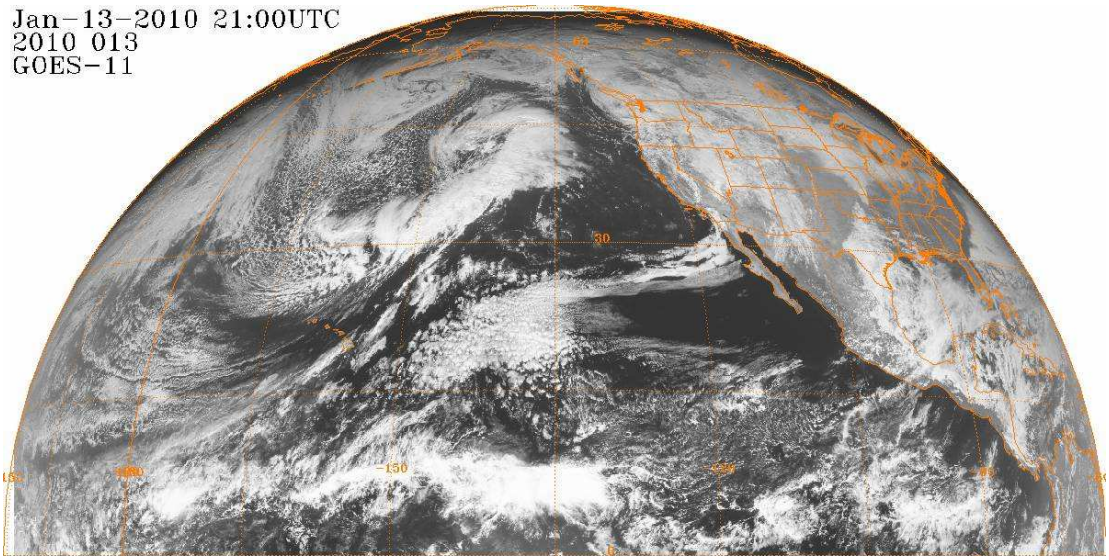

Figure 2.1: Visible satellite image from GOES-11 for 13-Jan-2010 at 2100UTC over the Eastern Pacific Ocean. (http://www.ncdc.noaa.gov/gibbs/availability/2010-01-13)

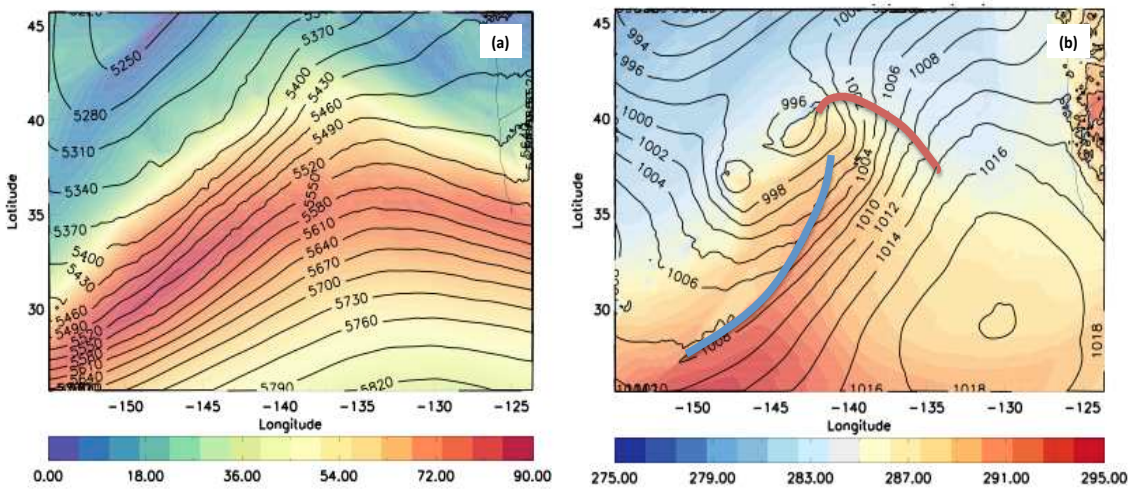

Figure 2.2: Plots of (a) 300-hPa wind speed (shaded; m s^{-1}) and 500-hPa geopotential height (contoured; m), and (b) surface potential temperature (lowest model level: 40 m above the sea surface) (shaded; K) and sea level pressure (contoured; hPa) from grid 2 analysis of the clean (CL) simulation at 14 January 2010 00UTC (simulation hour 48). Approximate locations of the warm front (thick red line) and cold front (thick blue line) are drawn on panel (b).

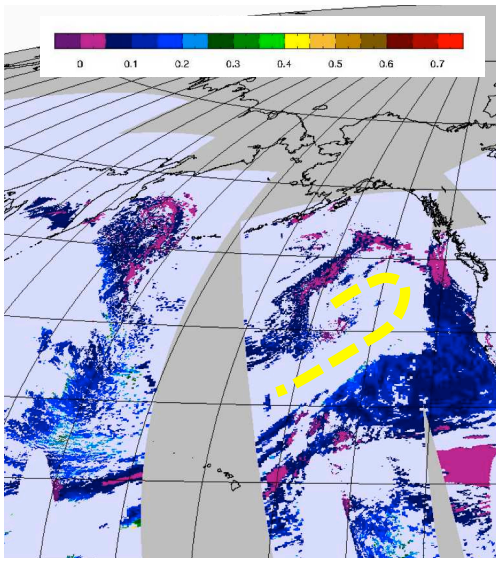

Figure 2.3: Aqua MODIS Level 2 Aerosol Optical Depth (AOD) over land and ocean for 13 January 2010. The image is focused on the northern-eastern Pacific Ocean. Retrievals are not accurate when clouds are present and thus are removed from the image. The ETC used this case study is found near the west coast of the United States and its' general location is marked by a dashed yellow line.

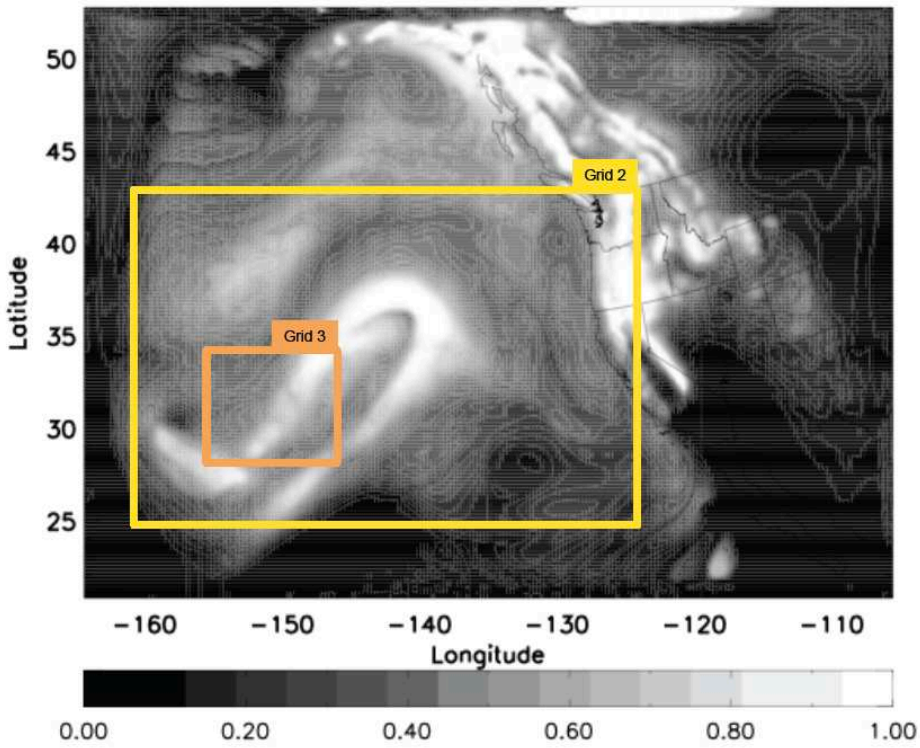

Figure 2.4: Cloud fraction of the outermost grid (25 km resolution) from the CL simulation after 48 hours (14 January 2010 00UTC), overlaid with the locations of the two finer resolution, nested grids (5km and 1 km). All grids setups were the same for the simulations outlined in Table 1.

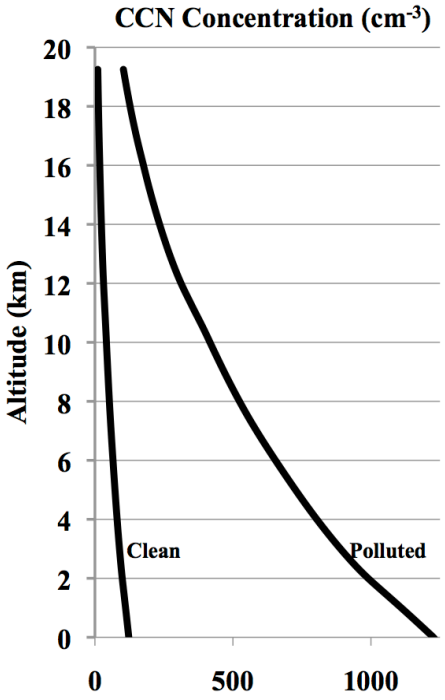

Figure 2.5: Cloud condensation nuclei (CCN) concentration (cm^{-3}) profiles for the clean and polluted ETC simulations found in table 2.1.

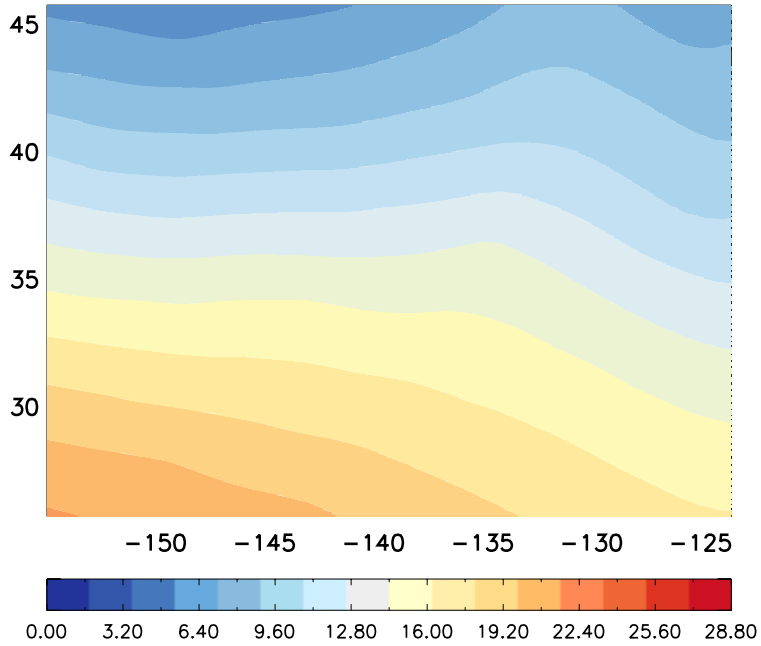

Figure 2.6: The horizontal distribution (longitude vs. latitude) of SST (^{o}C) from Grid 2 for the CL simulation.

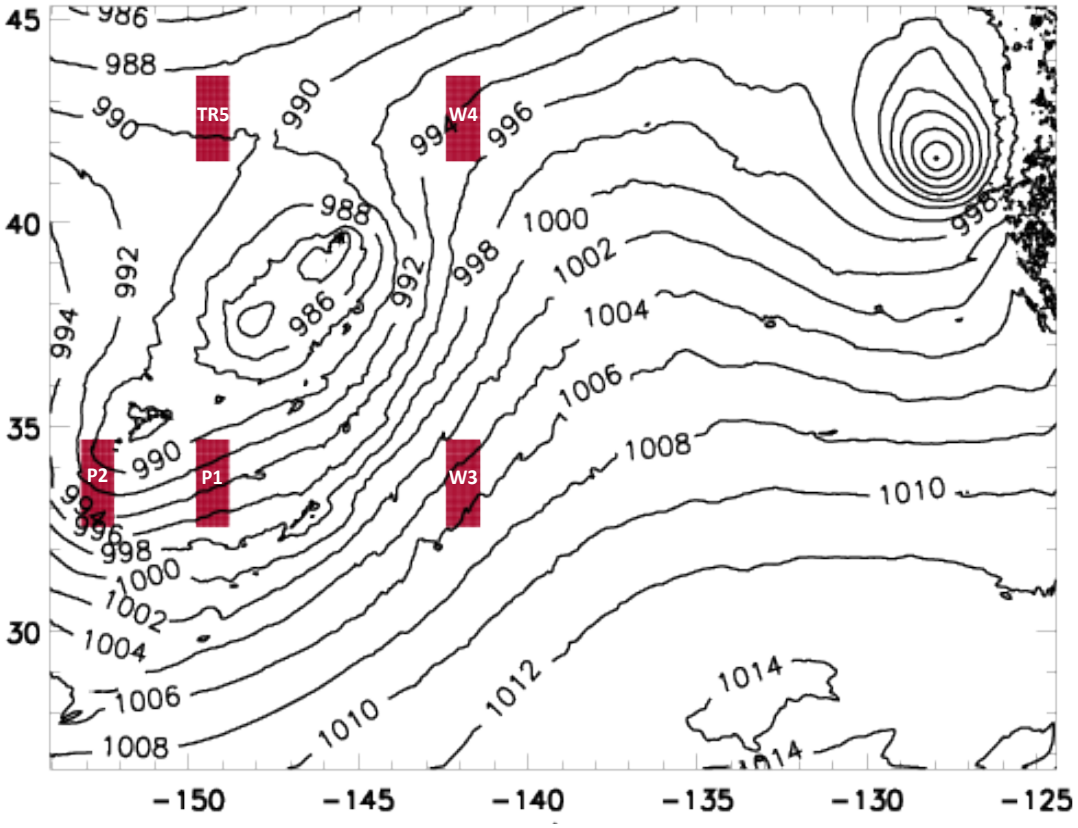

Figure 2.7: Horizontal plan view of the location of the initial surface locations of the tracers (shaded in red) initiated at five different locations near the ETC, overlaid with sea level pressure (black contour, hPa). A sixth tracer (SFC-TRACER) was released from the surface and continuously replenished as discussed in section 2.2B.

3. POST-COLD FRONTAL CLOUD CHARACTERISTICS

3.1 INTRODUCTION

Previous studies of ETC moisture transport that have highlighted the role of PCF clouds used relatively coarse model resolutions (0.4^{o}) and convective parameterization schemes to examine idealized ETCs (B10; B11). As such, these prior simulations are unsuitable for examining the characteristics of PCF clouds on the cloud scale, including their variations with environmental conditions. Here, we will extend the B10 and B11 studies by utilizing a high resolution CRM that is convection permitting to examine the microphysical, dynamical, and latent heating characteristics of PCF clouds. These simulations and subsequent analysis will allow us to better understand PCF cloud structure and properties, including latent heating and updraft speeds, and hence their vertical water vapor mass flux properties. The subsequent set of sensitivity simulations, in which the available cloud nucleating aerosol number concentration (CCN) and sea surface temperature (SST) are altered will then advance our understanding of how these two factors not only influence the microphysical and dynamical characteristics of PCF clouds, but also the vertical flux of moisture from the BL to the free troposphere by PCF clouds, and the subsequent regional advection of moisture within the storm system. In this study, we will be referring to the BL as both the sub-cloud and shallow cloud layers capped by the BL inversion.

First, the development of the wintertime ETC and the PCF region from the CL simulation will be examined. As a reminder, the CL simulation (table 2.1) utilized clean aerosol conditions and climatologically averaged SSTs. The sensitivity of the ETC, in particular the PCF region, to SST and available cloud nucleating aerosol will then be analyzed. We will be referring to the shallow BL PCF cumulus clouds simulated here as PCF cumulus clouds that are limited by the

BL inversion and the deeper PCF cumulus clouds that reach the mid-troposphere as PCF congestus clouds.

3.2 CL SIMULATION CHARACTERISTICS

A. EXTRATROPICAL CYCLONE CHARACTERISTICS

Figure 3.1 shows plan views of the cloud fraction on Grid 1 for (a) 36, (b) 42, and (c) 48 simulation hours of the CL simulation. This ETC storm developed over the Pacific Ocean in the southwest portion of the domain (figure 3.1a), and moved eastward and poleward as it matured and developed (figure 3.1b,c). The simulated ETC developed in a manner similar to the observed ETC. Figure 3.2 shows infrared (IR) satellite images from GOES-11 from the same time periods as those shown in figure 3.1. IR imagery was chosen for comparison, as visible satellite imagery was not available at 12UTC 13 Jan 2010 due to this time period being before sunrise over that region. Both the simulated and observed ETC show an expansive cloud field north of 30^{o}N (figures 3.1, 3.2), with clouds extending to the southwest in the classic comma head shape. A field of shallow cumulus clouds can be seen in the observations to the northwest of the cold front (figure 3.2). While not visible in figure 3.1 due to the coarseness of this grid, a field of shallow clouds is simulated in the finest grid of the CL and other sensitivity experiments, and will be shown in the following sections.

Figure 3.3 shows the simulated synoptic conditions (Grid 2) associated with this storm at the same times shown in figure 3.1. Grid 2 contains the entire ETC and is convection resolving at 5 km resolution. The ETC formed in association with the subtropical jet, with wind speeds of 80 – 90 m s^{-1} (figure 3.3a,c,e). The primary warm and cold fronts are evident in the surface potential temperature (K) and sea level pressure (hPa) fields (figure 3.3b,d,f). A weak secondary cold front develops to the west of the primary cold front, and is most prominent in the most mature stage

(figure 3.3f). The central pressure of the ETC deepened after the first 24 hours of the simulation (figure 3.4a), reaching a low value of ~991 hPa. Pressures from 991-994 hPa were sustained throughout the mature stage of this storm (36 – 54 hours). The ETC produced ~2.8 mm of domain accumulated precipitation in 24 hours (figure 3.4b).

The primary purpose of this study is to explore PCF moisture transport in an ETC and not the model's ability to reproduce the exact particular features of this wintertime ETC. However, we have clearly shown that the CL simulation captures the simulated life cycle and large-scale characteristics of the ETC well when compared to the available real-time observations. We can therefore now examine the characteristics of the simulated ETC and PCF region with confidence.

B. THERMODYNAMIC PHASES

The local atmosphere varies thermodynamically in the expansive region behind the cold front due to the synoptic scale forcing associated with the ETC. This variation can influence the characteristics of the PCF clouds that occur, including their microphysical and dynamical properties. Here we identify two different environmental phases in the PCF region based on the mid-tropospheric and BL temperature structure and moisture fields. In later sections, differences in the PCF cloud characteristics across these two phases will be examined.

The two environmental phases will be referred to as PHASE-1 and PHASE-2. Figure 3.5 shows an example from the highest resolution grid (Grid 3) of the horizontal and vertical distribution of PCF clouds, and the corresponding relative humidity and potential temperature fields during each of these phases (14UTC 13 Jan 2010 and 00UTC 14 Jan 2010, respectively). Vertical profiles of the Grid 3 clear air average water vapor mixing ratio (g kg^{-1}) for each phase are shown in figure 3.6.

PHASE-1 occurs immediately behind the primary cold front (figure 3.5a,b,c). Here, the remnants of the cold front (thick blue line on figure 3.5a) are evident in the southeastern portion of the domain, and the field of PCF cumulus clouds maybe seen to the west and northwest of the front (figure 3.5a). The PCF atmosphere is primarily composed of a moist BL overlaid by a dry free troposphere (figures 3.5b, 3.6). The free troposphere is driest closest to the cold front, and represents the impacts of the subsiding dry conveyor belt (DCB) (e.g. Browning 1997). Shallow cumulus clouds form slightly further northwest of this dry zone (figure 3.5a,c). Their vertical development is constrained by the strong inversion ($d\theta/dz$~4 K (0.5-km)$^{-1}$) located near 2 km above sea level (ASL) (figures 3.5c). The height of the inversion increases to ~3 km ASL at the western grid boundary (figure 3.5c). In PHASE-1, these BL cumulus clouds cover over 35% of the domain (figure 3.7a). A few deep convective clouds do occur during PHASE-1 (figure 3.7a) and extend to the mid troposphere (~7-8 km ASL). The primary cold front propagates to the southeast and out of Grid 3 early in PHASE-1. The PCF clouds also propagate to the southeast behind the cold front.

PHASE-2 occurs in association with large-scale free tropospheric moisture advection and reduced static stability (figure 3.5d,e,f). The moistening of the free troposphere is by a relatively small amount (figure 3.6) but evident from several hundred kilometers behind the cold front and extends vertically up to about 8 km ASL (figures 3.5e, 3.6). Although the water vapor mixing ratio in the mid-troposphere is increasing by a small amount, the average water vapor mixing ratio in the BL decreases more substantially, by ~1.5 g kg^{-1} compared with PHASE-1 (figure 3.6). This could be due to large-scale horizontal advection and/or PCF cloud transport out of the BL. The troposphere cools, including the BL (figure 3.5f). The freezing level (0^{o}C level) (FL) in PHASE-1 occurs at ~1.75 km ASL, while the cooler atmosphere in PHASE-2 is associated with

a lowering of the FL to ~1.5km. The strong BL inversion that was present during PHASE-1 is now weaker (~ 2.5 K $(0.5\text{-km})^{-1}$) (figure 3.5e,f), and BL convective clouds start to develop to greater heights. The shallow cloud fraction is now ~10% less than that in PHASE-1 (figure 3.7b). This occurs as cloud structure shifts to deeper congestus clouds in association with the weaker inversion and moistening of the mid-troposphere (figures 3.5e,f). While PCF clouds remain present in PHASE-2, the development of the weak secondary cold front may be impacting the atmospheric thermodynamics of this phase. In summary, the transition to PHASE-2 is associated with a weaker inversion, fewer PCF cumulus clouds, and a greater number of deeper cumulus/cumulus congestus clouds, the evidence of which may be seen in the greater cloud fraction between 3.5 and 5 km (figure 3.7b).

C. CLOUD MICROPHYSICAL CHARACTERISTICS

In this section we will examine the cloud microphysical characteristics of PCF cumulus clouds in both PHASE-1 and PHASE-2 of the CL simulation. Understanding the cloud microphysical structure and it's link to environmental conditions is important for understanding the formation of the cloud updraft and the resultant vertical water vapor mass flux, and also the formation of precipitation as this serves as a sink of water vapor. The PCF high-resolution domain (Grid 3) was utilized for 18 simulation hours following the maturation of the ETC during the first 36 simulation hours. Here we examine the vertical profiles of several temporally- and spatially-averaged cloud microphysical characteristics and processes over PHASE-1 (14 - 22UTC 13 January 2010) and PHASE-2 (22UTC 13 January 2010 – 06UTC 14 January 2010). The first two hours after the third grid was utilized were not included in the PHASE-1 average time period due to the presence of the primary cold front. 5-minute model output was used to

generate the averages discussed below, and cloudy points were identified where total condensate was greater than 0.1 g kg^{-1}.

Even though PHASE-1 is composed primarily of shallow cumulus clouds, deeper congestus clouds do occasionally occur (figure 3.7). Hence, shallow and deeper clouds are included in both PHASE-1 and PHASE-2 average vertical profiles. By virtue of their infrequency, fewer cloudy points are utilized in the deep cloud averages in the mid-to-upper troposphere (4-8 km ASL). Near 1-3 km ASL, the averages represent both shallow and deep clouds. In addition, the use of total condensate to define cloud results in the incorporation of precipitation points below cloud base.

Figure 3.8 shows the spatially- and temporally-averaged vertical profiles of cloud water, rain/drizzle, and total ice (pristine ice, snow, aggregates, graupel, hail) mixing ratios (g kg^{-1}) for PHASE-1 (a-c) and PHASE-2 (d-f). Dashed lines on panels (a) and (d) indicate the approximate altitudes of cloud base (black), the freezing level (blue), and the BL inversion (red), which vary with phase. From this point forward, rain is used to refer to both rain and drizzle. In both PHASE-1 and PHASE-2, average cloud base height is near 1 km ASL and peak cloud water mass is found near 2 km ASL (figure 3.8a,d). The PCF clouds in these simulations are primarily cumulus clouds (figure 3.5), which are capped by the BL inversion. Some of the deepest cumulus to congestus clouds are mixed phase (figure 3.8c,f) in both PHASE-1 and PHASE-2, which is in keeping with the observations of Naud et al. (2015b). The PHASE-1 and PHASE-2 average cloud condensate profiles are similar in basic structure, although some notable differences are evident. The average cloud mixing ratio is similar in association with the PCF cumulus clouds, in both phases (figure 3.8a,d). In the upper levels however, greater masses of average rain, cloud, and ice (figure 3.8) occur in the fewer, deeper PCF congestus clouds in PHASE-1 compared to

the more numerous PCF congestus clouds in PHASE-2 that form in the less stable atmosphere. In the shallow cumulus clouds that do not form large amounts of ice, surface precipitation is forming primarily through rain processes. In the deeper clouds that do form ice, nearly all ice melts before reaching the surface and converts to rain. Greater surface precipitation mass occurs in PHASE-1 (figure 3.8b,c,e,f).

These profiles of cloud, rain, and total ice mixing ratios can be explained through an examination of the microphysical processes occurring within these systems. Figure 3.9 shows the spatially- and temporally-averaged vertical profiles of the rate (g kg^{-1} 5-$minute^{-1}$) of most of the microphysical processes impacting PCF clouds for both PHASE-1 and PHASE-2, including (a) the nucleation of cloud droplets and net evaporation-condensation onto cloud droplets and raindrops, (b) the nucleation of ice particles and net sublimation-deposition onto all ice hydrometeors, (c) cloud to rain water conversion through collision-coalescence, (d) the riming of cloud water by ice, (e) the accretion of rainwater onto ice, and (f) the melting of ice.

PCF clouds initially form as a result of the convective instability generated as a result of the cold air mass behind the cold front moving over a relatively warm ocean surface (figure 3.5). As an air parcel is lifted and reaches saturation, cloud-nucleating aerosol activate. Cloud base is ~1 km ASL in both PHASE-1 and PHASE-2 (figure 3.8a,d). As the cloud grows vertically, cloud droplets will continue to grow through vapor deposition followed by collision-coalescence processes. The cloud tops are primarily limited to 2.5-3 km ASL by the inversion layer. The average FL is found to be near 1.5-1.75 km ASL (depending on the horizontal distance to the cold front, i.e. the environmental phase). The strongest PCF clouds may break through the BL inversion layer, become mixed phase, and reach the upper levels. During PHASE-1, the BL inversion is stronger than in PHASE-2, which combined with the large BL water vapor contents

and suppression of deeper clouds results in a greater number of PCF cumulus clouds while only a few stronger PCF congestus clouds are able to surpass the inversion.

Cloud water mass peaks at ~ 2.5 km ASL in these clouds (figure 3.8a,d), just above the altitude of peak vapor depositional growth (figure 3.9a). Peak rates of vapor depositional growth are approximately four times greater than the other microphysical processes examined in figure 3.9. Raindrops form through collision-coalescence, and serve as a sink to cloud droplets (figure 3.9c). This process maximizes between 3.5-4 km ASL and explains the maximum in average rain mixing ratio at this level (figure 3.8b,e). While ice does form in the PCF cumulus clouds, the amount of ice is much less than that of the cloud water and rain (figure 3.8). Cloud and rain formation processes are therefore most critical to their development. The average rain mixing ratio of the shallow cumulus clouds will be less than of those of the deeper congestus clouds that are able to form rain and ice more effectively through their vertical motion and lifting.

Ice processes occur primarily in the deeper PCF congestus clouds between 4-8 km ASL including ice nucleation and vapor depositional growth of ice particles (figure 3.9b). Ice hydrometeors continue to grow through the riming of cloud droplets (figure 3.9d) and accretion of rainwater (figure 3.9e). Both of these latter processes peak near ~4 km ASL, depleting the readily available cloud water and rainwater mass near this level.

Average ice mass is largest above 4 km ASL, in association with the deeper congestus towers. Near cloud base, a smaller magnitude peak in ice mass occurs near 1 km ASL (figure 3.8c,f). This is due to the accretion of rain onto precipitating ice near the FL (figure 3.9e) before ice melting is maximized near 0.5 km ASL (figure 3.9f). Average rain mass increases below cloud base due to this melting (figure 3.8b,e). Most of the ice mass melts before reaching the surface (figure 3.8c,f), and evaporation of rainwater can be seen below cloud base (3.9a).

Differences in these microphysical processes between PHASE-1 and PHASE-2 results in less average cloud and rain water mass in PHASE-2 (figure 3.8). More cloud water is forming through warm phase processes (figure 3.9a) over a greater depth in PHASE-1 due to the availability of water vapor in the moister deeper BL (figure 3.6a). Subsequently, this leads to increased rainwater formation through collision-coalescence in PHASE-1 cumulus clouds (figure 3.9c). In the deeper congestus, more cloud water is lofted near 3-5 km (figure 3.8a) where collision-coalescence and conversion to rain continues (figure 3.9c). On average, more rain mass forms within cloud near 3-4 km ASL compared to PHASE-2 (figure 3.8b,e) and more rain is then available for accretion by ice (figure 3.9e). Above this altitude, ice begins to form through heterogeneous nucleation and to vapor depositionally grow (figure 3.9b). Ice mass also increases from riming of cloud water (figure 3.9d). Overall, the increase in average rain mass of the shallower PCF cumulus clouds combined with a similar increase in the rain and ice mass in the fewer, stronger deeper congestus clouds that are able to break through the BL inversion, results in a greater average precipitation mass at the surface in PHASE-1 compared to the PHASE-2 clouds.

Figure 3.10 shows a time series of the Grid 3 average instantaneous precipitation rate (mm hr^{-1}), including non-precipitating grid points, for both PHASE-1 (simulation hour 36-46) and PHASE-2 (simulation hour 46-54) of the CL simulation. As shown above, PCF precipitation is primarily composed of rain. The average simulated PCF regional precipitation rates of 0.1-0.4 mm hr^{-1} are highly comparable to those observed from the A-train (Naud et al. 2015a). The peak precipitation rate near simulation hour 38 is due to the remnants of the cold front in Grid 3. The larger average precipitation rates in PHASE-1 are a function of the significantly larger PCF

cloud fraction that develops in association with the moister BL (figure 3.7), as well as the greater average rain mass associated with each of these BL cumulus (figure 3.8d).

The PCF cloud microphysical processes are linked to the latent heating structure, which then impacts the cloud dynamics through changes to cloud buoyancy. The cloud updraft is responsible for vertically lofting cloud condensate that can subsequently evaporate or form precipitation hydrometeors. The strength of the updrafts is also integral to the flux of water vapor from the BL to the free troposphere. In clouds of this size, latent heating has been shown to be important in determining updraft speed (e.g. Sheffield et al. 2015) and will be examined here.

Figure 3.11 shows the average rates of latent cooling and latent warming (K 5-minute^{-1}) associated with vaporization and freezing. Here, latent warming/cooling due to vaporization processes includes the nucleation of cloud droplets and ice particles and vapor depositional growth or evaporation/sublimation of cloud droplets, raindrops, and ice particles. Latent warming/cooling due to freezing includes contributions from any freezing that takes places during the riming of cloud water and accretion of rainwater and conversely from the melting of ice. These heating and cooling rates are then separately spatially- and temporally-averaged for both PHASE-1 (figure 3.11a-d) and PHASE-2 (figure 3.11e-h).

In both phases, the peak rates of latent warming due to vaporization at 1 and 4 km ASL coincide with the peak rates in nucleation and vapor depositional growth of cloud droplets and ice particles (figure 3.11b,f) while the largest latent cooling occurs near the BL inversion due to cumulus cloud evaporation and below cloud base due to raindrop evaporation (figure 3.11a,e). Latent warming occurs in association with freezing due to riming of cloud water near 4 km ASL and accretion of raindrops in the deeper congestus near 1 and 4 km ASL (figure 3.11d,h) while melting near and below cloud base controls the latent cooling signal (figure 3.11c,g).

The vertical profiles of the spatially- and temporally-averaged cloud updraft speed (m s^{-1}) from (a) PHASE-1 and (b) PHASE-2 (figure 3.12) correspond to the vertical distribution of the net latent warming profiles. The greatest average updraft speeds in these clouds occur above cloud base where cloud droplets are readily forming and growing by vapor deposition, releasing large amounts of latent heat thereby enhancing to cloud buoyancy (figure 3.11b,f). In the deeper PCF congestus clouds, the updraft gets a second boost aloft near 4 km ASL where ice formation is largest due to vapor depositional growth of ice (figure 3.11b,f). Freezing in association with the riming of cloud water and accretion of rain releases latent heat (figure 3.11d,h) and also contributes to the updrafts at 3-4 km, but is an order of magnitude less than those processes associated with vaporization. These microphysical processes are greater in PHASE-1 due to the warmer moister BL, which leads to stronger updrafts over deeper layers both in the cumulus and congestus modes. Fewer deep congestus clouds occur in PHASE-1 due to the strength of the BL inversion. It is only the strongest cumuli that go onto form congestus that are incorporated into the average at 3-6 km ASL and access the mixed phase contribution to cloud buoyancy, which is greater in PHASE-1.

In summary, the PCF clouds in these simulations are characterized by cumulus clouds that form as a result of convective instability and turbulent mixing below the inversion layer that arises due to the flow of cold air over a relatively warm ocean. These clouds remain constrained by the inversion layer but occasionally develop to congestus when they are able to penetrate through the stable layer. In the PCF region of the ETC examined here, the cloud depths are typically 1-1.5 km and the FL occurs 500-750 m above cloud base. If PCF clouds remain shallow, warm phase processes play the predominant role in their development. However, if they deepen, the freezing of cloud droplets through riming and subsequent vapor depositional growth becomes

important. PHASE-1 immediately follows the passage of the cold front and is characterized by a moist BL overlaid by a strong BL inversion and a dry free troposphere. Shallow clouds occur predominantly during this phase (cloud fractions of ~35%), and only a few stronger congestus clouds extend to the mid-troposphere. PHASE-2 is evident several hundred kilometers behind the primary cold front and is characterized by a cooler upper air mass. The PHASE-2 BL is drier and capped by a weaker inversion, which leads to a reduced number of PCF cumulus clouds while allowing for an increasing number congestus clouds. Average cloud condensate and subsequently precipitation mass is greater in the PCF clouds of PHASE-1, which, combined with an increased cloud fraction, results in greater precipitation rates.

In the next chapter, we will examine how these cloudy updrafts contribute to the overall vertical water vapor mass flux of the PCF region. The average cloud updraft speed maxima located at ~2 km ASL and 4 km ASL will have important consequences for the water vapor mass flux in association with both the magnitude of the vertical velocity and the vertical distribution of the water vapor mass. The next sections will examine how SST and aerosols alter the magnitudes of these cloud microphysical characteristics and subsequently the updraft and surface precipitation rates.

3.3 SEA SURFACE TEMPERATURE SENSITIVITY EXPERIMENTS

First we will examine how PCF cloud characteristics vary due to increased SST by examining the CL, -2KCL, and +2KCL simulations. Generally, the ETC system intensifies when the magnitude of SST increases (figure 3.13a,b), as expected (e.g. Field and Wood 2007). With increasing SSTs, the central pressure lowers and the ETC accumulated precipitation increases. The central pressure varies by 2-8 hPa and the accumulated precipitation differences vary by as much as 50-100%. SST is therefore an important control of the ETC system, and exerts its

control through impacts on atmospheric instability, the moisture supplied to the ETC, the associated latent heating structure, and subsequent development of potential vorticity and cyclogenesis (e.g. Posselt and Martin 2004).

There can be large societal impacts from these SST-induced changes to precipitation, including when and where precipitation occurs. SST-induced intensification of the ETC in these simulations resulted in a slight shift in the location of the ETC low pressure center to the north and east indicating a minor increase in the overall ETC speed of propagation (not shown). While not the focus of the study here, this propagation pattern, combined with any changes in precipitation intensity, could have large implications for the timing and storm intensity at landfall at the western US.

The PCF region develops in generally the same way in the CL and +/-2KCL simulations in that a drier free troposphere overlays a moist BL in PHASE-1, followed by a small free tropospheric moistening due to large scale advection in PHASE-2 (e.g. figure 3.14 for the +2KCL simulation). The BL is deeper over warmer SSTs (figure 3.14c,f) and increased water vapor contents are found in the BL (not shown). The average atmospheric temperature profile of the PCF BL region over warmer (cooler) SSTs increases (decreases) by ~1 K through the depth of the profile in both phases (figure 3.15), which results in the higher BL moisture contents as predicted by the Clausius-Clapeyron equation. The FL also rises with increasing SST (figure 3.15).

Differences in the vertical distribution and frequency of PCF cumulus clouds occur as a result of varying the SST. The PCF cloud fraction for the -2KCL and +2KCL experiments for (a) PHASE-1 and (b) PHASE-2 is shown in figure 3.16. The peak in PCF cumulus clouds occurs at a higher (lower) altitude (figure 3.16) due to the increased (decreased) height of the BL inversion

associated with the warmer (cooler) surface. In PHASE-1, warmer SSTs promote a shift to more frequent congestus clouds at the expense of shallow clouds while cooler SSTs reduce all cloud fractions compared to the CL simulation (figure 3.16a). Corresponding trends occur in PHASE-2 (figure 3.16b), where the shift to deep convection from shallow convection is intensified with increasing SSTs. The cloud fraction increases in magnitude on the order of 3-7% for the deeper congestus clouds, depending on phase and cloud depth, with a corresponding decrease in the shallow cumulus cloud fraction. Thus, warmer SSTs produce a warmer, moister, and deeper PCF BL and promote more frequent deeper congestus clouds.

Figures 3.17-3.21 are similar to figures 3.8-3.12, respectively, but now show the results from the CL, +2KCL, and -2KCL simulations. Additional panels have been added to show the differences between the simulations. PCF cloud base is dependent on the SST-altered atmospheric profile. For example, cloud base over increasing SSTs is slightly higher (figure 3.17a,d,g,j). As shown by the Clausius-Clapeyron equation, saturation vapor pressure varies with temperature. For an atmospheric temperature profile that is shifted to warmer temperatures, a larger vapor pressure is required to achieve the saturation vapor pressure and hence form cloud. In order to have a lifted condensation level (LCL) at the same altitude over warm SSTs as over cooler SSTs, an increase in water vapor mixing ratio is therefore needed. While increased water vapor mixing ratios are found over the warmer SSTs, this cannot completely compensate for the increased saturation vapor pressure associated with the increased temperature, and thus the LCL and cloud base occur at a higher altitude. This shift in the cloud base will impact the development of the PCF clouds. Caution has to be taken when comparing the average cloud microphysical profiles in figures 3.17-3.21 due to the slight shift in the vertical location of the

cloud microphysical processes in association with the differences in vertical temperature structure.

Clouds forming in the warmer and moister BL are associated with more vigorous updrafts (figure 3.18). In both phases, the average updraft speed between 1-3 km ASL is greater in the PCF cumulus clouds over the warmest SSTs. A warmer BL results in a greater updraft speed as PCF clouds initially form, which combined with a moister BL promotes more cloud water formation. At a first glance, the average PCF cloud condensate profiles in figure 3.17 show the opposite, where clouds forming over warmer SSTs generally have less cloud water. However, PCF cumulus clouds occurring over warmer SSTs produce more rain water (figure 3.17b,e,h,k) and have greater ice contents (figure 3.17c,f,i,l). The cloud water that is produced is efficiently converted to rain through collision-coalescence (figure 3.19c,i,o,u), thereby reducing the average cloud water mixing ratio in PCF cumulus clouds. Vapor depositional growth differences also occur (figure 3.19a,g,m,s).

In the deeper congestus clouds, the invigorated updrafts over warmer SSTs loft more cloud water and rainwater. Less cloud water is available to be frozen to nucleate ice, subsequently resulting in decreased rates of nucleation and vapor depositional growth of ice (figure 3.19b,h,n,t). However, the ice that does form readily grows by riming of cloud water (figure 3.19d,j,p,v) and accretion of rainwater (figure 3.19e,k,q,w). This results in a greater average ice mass near 2-6 km ASL (figure 3.17c,f,i,l) for increasing SSTs.

The increased ice mass falls towards the surface as precipitation, and this, together with the increased average rain mass from the warm rain process, results in greater amounts of precipitation mass near cloud base (figure 3.17). As SST increases, the warmer BL produces melting at higher altitudes (figure 3.19f,l,r,x). This exposes the precipitation to evaporative

processes for longer time periods. Thus, while more rain water and ice are produced with increasing SST, the enhanced evaporation of precipitation (figure 3.19a,g,m,s) offsets this increase somewhat. The average surface precipitation is therefore not significantly different between the CL and +2KCL simulations (figure 3.17b,e,h,k).

Examining the average vertical profiles of latent warming/cooling for these clouds show the signatures for these microphysical processes (figure 3.20). Latent heating increases with increasing SST in association with the initial greater nucleation and vapor depositional growth of cloud water (figure 3.20b,f,j,n) before the efficient warm rain process. The reduced vapor nucleation and vapor depositional growth of ice results in less latent warming above 4 km ASL (figure 3.20b,f,j,n). Additional latent heating is also evident in association with the riming of cloud water and accretion of ice (figure 3.20d,h,l,p) being greater in the warm SST cases due to the greater availability of liquid water. In addition, the ice that forms in clouds over warmer SSTs melts at a higher altitude (figure 3.20c,g,k,o), allowing more latent cooling from rain evaporation near the surface (figure 3.20(a,e,i,m).

The overall grid domain average precipitation rate (figure 3.21) is also a function of the cloud fraction (figure 3.16). Increasing SSTs promoted the shift to deeper congestus clouds at the expense of shallower cumulus clouds. This increased the number of precipitating grid points. This can be seen in the condensate fraction below cloud base in figure 3.16, which is due to the presence of precipitation. Therefore, over warmer SSTs, while the increased evaporation of precipitation below cloud base offsets the increase in rain and ice mass, the change in the frequency of deeper versus shallow clouds constrained this effect. Hence, we see increased average PCF precipitation rates over warmer SSTs (figure 3.16). This effect is strongest in PHASE-1, where the cloud microphysical differences and cloud fraction are greater than in

PHASE-2. The weakening of the BL inversion in PHASE-2 already promotes the development of deeper clouds, thereby reducing cumulus cloud fractions compared to PHASE-1.

In summary, with warmer SSTs, a warmer, moister, and deeper PCF BL forms. This leads to more deeper, congestus type PCF clouds through invigorated updrafts. In the PCF cumulus clouds the invigorated updraft promotes an efficient warm rain process. Subsequent ice formation, riming of cloud water, and the accretion of rainwater by ice occur above the BL in the deeper congestus clouds, thereby promoting greater rain and precipitating ice amounts in these clouds. A warmer, deeper BL partially offsets this increase in precipitation through enhanced precipitation evaporation below cloud base, but the shift to more frequent congestus at the expense of shallow cumulus counterbalances this leading to an overall increase the average surface precipitation rate in the PCF region with increasing SST. Therefore, total PCF surface precipitation rates increase with increasing SST through invigorated PCF clouds but is somewhat constrained by precipitation evaporation and the shift in cumulus cloud fractions.

3.4 CLOUD NUCLEATING AEROSOL SENSITIVITY EXPERIMENTS

Now we examine the impacts of variations in cloud nucleating aerosol number concentration on the PCF cloud characteristics. This will be achieved by comparing the CL and PO simulations.

The intensity of the ETC storm system is found to change little with increased cloud nucleating aerosol concentration. The central pressure varies by ~1-2 hPa and the Grid 2 accumulated surface precipitation is reduced by 3-8% (figure 3.22). Clearly the variations in SST tested here exert much more significant impacts on the storm intensity and total precipitation, although shifts in the location of more intense precipitation due to aerosol may be occurring as found by previous studies (e.g. Igel et al. 2013; Thompson and Eidhammer 2014).

As both the CL and PO simulations utilized the same SST dataset, environmental impacts on cloud development will occur due to any differences between PHASE-1 and PHASE-2 (as discussed in section 3.2) and to the presence of aerosol. In both PHASE-1 and PHASE-2, increasing the available aerosol concentration increases both the number of BL cumulus and deeper congestus clouds (figure 3.23). However, these changes are less than those induced by SST, except for the increase in PHASE-1 congestus clouds. In PHASE-1, this indicates that aerosol-induced changes to the PCF cumulus clouds promote not only a higher frequency of cumulus clouds constrained by the BL inversion, but also increases the ability of PCF congestus clouds to grow above the BL by a factor of 2. This trend is weaker in PHASE-2, where the weaker BL inversion and less stable free troposphere already promote the development of deeper clouds.

Figures 3.24-3.28 are similar to figures 3.17-3.21 but instead show the cloud microphysical characteristics for the CL and PO simulations, including differences between the cloud microphysical average profiles. Cloud base in the PO simulation is near 1 km ASL, similar to PCF clouds in the CL simulation (figure 3.24a,d,g,j). Classic aerosol indirect effects (AIEs) due to increasing cloud nucleating aerosol concentration occur in these simulated PCF clouds. Increasing aerosol concentrations results in an increase in average cloud water mass (figure 3.24a,d,g,j) in the PCF cumulus clouds, and a decrease in the mass of rain formed (figure 3.24 b,e,h,k). And, as these clouds grow deeper to PCF congestus clouds, an increasing amount of ice is generated (figure 3.24c,f,i,l).

The processes related to the AIEs occur in the following way: PCF clouds develop in a more polluted but similar thermodynamic environment, more of the excess supersaturation is able to be utilized by the increased number of aerosol that are available to be activated (e.g.

Twomey 1974; Reutter et al. 2009). This results in an increased number of cloud droplets that are smaller in size. The aerosol-induced shift in the cloud droplet size distribution (DSD) alters the ability of these clouds to convert cloud droplets to raindrops as a more homogeneous cloud DSD reduces the efficiency of collision-coalescence (e.g. Albrecht 1989). As a result, the warm rain process is suppressed. This is evident in the polluted PCF clouds as the average cloud mass is increased (figure 3.24a,d,g,j) and the rain mass is reduced (figure 3.24b,e,h,k) as the collision-coalescence processes becomes less efficient (figure 3.25c,i,o,u). The average cloud water mass of the polluted PCF cumulus clouds is enhanced by greater cumulative vapor depositional growth near cloud base (figure 3.25a,g,m,s) as the larger net surface area of the population of more numerous, smaller cloud droplets increases condensation. This result has also been found in previous studies of tropical cumulus congestus clouds (Sheffield et al. 2015).

The suppression of the warm rain process results in a greater availability of cloud water to be lofted above the FL if the cloud grows beyond the BL inversion, which increases the average ice mass in the PO congestus clouds (figure 3.24c,f,i,l). Ice hydrometeors can continue to grow through vapor deposition (figure 3.25b,h,n,t), the riming of cloud water (figure 3.25d,j,p,v), and the accretion of rainwater (figure 3.25e,k,q,w). In the uppermost portions of the congestus clouds (4-7 km ASL), vapor deposition onto ice is enhanced compared to the CL simulation due to the fact that there are more particles that have a larger cumulative surface area for such growth (figure 3.25b,h,n,t). The riming rates are also greater in the polluted cases due to the more readily available cloud water (figure 3.25d,j,p,v) while the reduced average rain mass consequently reduces the amount of rain accretion by ice (figure 3.25r,k,q,w).

The amount of precipitation that reaches the surface is a function of both the rain and precipitating ice mass that melts/evaporates and/or reaches the surface. The melting of the

increased ice mass (figure 3.25f,l,r,x) offsets the reduced rain mass formation, however the surface precipitation mass is still less in the PO PCF clouds (figure 3.24b,e,h,k) due to a lack of collection of cloud droplets by the precipitating rain. Hence, the increased ice contents arising due to the less efficient conversion of cloud droplets to raindrops cannot overcome the decreasing amounts of the rain produced due to the suppression of warm rain processes in these PCF polluted clouds.

The changes in these microphysical processes will have an impact on the latent heating structure of these clouds (figure 3.26). In the more polluted PCF clouds, an increase in the warm phase latent heating is found as more cloud water is formed (figure 3.26b,f,j,n). Decreased evaporation of rainwater due to the fact that less rainwater is produced in the polluted cloud reduces the amount of latent cooling at the surface (figure 3.26a,e,i,m). Increased freezing following the enhanced riming of cloud water in the polluted cases aloft increases the latent warming, but is partially offset by the reduced heating source associated with the decreased accretion of rain (figure 3.26d,h,l,p). Melting contributes to latent cooling at lower levels (figure 3.26c,g,k,o), which is increasing with the increasing average ice mass of PO clouds.

In association with the latent heating profiles, greater average updrafts (figure 3.27) are found in the PO clouds from the invigoration due to latent heating in the warm phase while the updrafts are weaker in the deeper congestus clouds primarily due to condensate loading and reduced latent heating contributions (figure 3.24). The cloud fraction examined in figure 3.23 shows an increase in the frequency of PCF cumulus clouds near the BL inversion due to the suppression of the warm rain process and enhanced PCF congestus clouds due to the warm and cold phase aerosol-induced invigoration. While the per cloud surface precipitation rates were reduced, the PCF grid domain average precipitation rate (figure 3.28) is not consistently less in

the PO simulated PCF region compared to the CL simulation. In the shallowest PCF clouds, the warm rain process is suppressed which can reduce the number of precipitating PCF cumulus clouds. The increase in PCF congestus type clouds from aerosol induced updraft invigoration produce precipitation through mixed phase processes that can counterbalance this impact.

In summary, the sensitivity of the cloud microphysics of these PCF clouds to increased aerosol directly impacts the magnitude of the average updrafts and the amounts of surface precipitation produced by these clouds. In the more polluted PCF clouds, more cloud water and ice form due to the suppression of the warm rain process in keeping with traditional AIEs (e.g. Tao et al. 2012). Updraft speeds are invigorated through enhanced latent heating, leading to more sustained, stronger, and frequent PCF congestus clouds. Lofting of increased amounts of cloud water in the congestus clouds allows for the formation of more ice. Reduced average surface precipitation occurs in these polluted PCF clouds as the warm phase suppression is not completely offset by the enhanced ice mass. The warm phase invigoration of the PCF cumulus clouds assists in increasing the number of clouds that reach the upper levels (figure 3.23), a process shown to occur in the tropics by Sheffield et al. (2015).

3.5 DISCUSSION

In this chapter, we characterized the microphysical characteristics of CRM simulated PCF cumulus clouds of a wintertime ETC. Understanding their cloud structure, development, and frequency is a necessary step in understanding how they process water vapor through cloud condensate formation and the vertical flux of water vapor in the PCF region, which is tied to the overall moisture transport within an ETC. PCF clouds in this wintertime ETC are primarily composed of shallow (1-2 km in depth) mixed phase cumulus clouds that occasionally extend into the troposphere (4-8 km ASL). Immediately following the primary cold front, these clouds

develop in a moist BL that is overlaid by a dry free troposphere (PHASE-1). Several hundred kilometers behind the cold front as the BL inversion weakens and the atmosphere becomes less stable, deeper convection occurs more readily (PHASE-2).

Warm phase processes primarily control PCF cumulus clouds in both phases. In PHASE-1, the warmer, moister BL promoted a greater PCF cumulus cloud fraction with greater average cloud mixing ratios. The strongest PCF congestus clouds were able to reach the free troposphere. In PHASE-2, the weaker inversion and a drier BL allowed for the development of more frequent PCF congestus clouds while reducing the overall number of PCF clouds. The increased rain and ice mass in the PHASE-1 clouds resulted in an increase in the average precipitation, which, when combined with a greater number of precipitating clouds, increased the average precipitation rate of the entire PCF region.

Increasing SST enhanced the warm phase microphysical processes, with subsequent impacts on the mixed phase processes. Over warmer SSTs, the BL is deeper, warmer, and moister, all of which invigorated the updrafts of PCF cumulus clouds. More frequent deeper congestus clouds were found, as was a greater average ice mass through riming and rain accretion. Combined with the increased rain mass, a greater average surface precipitation mass was found. This increased surface precipitation mass was partially offsets by the enhanced evaporation below cloud base due to a warmer, deeper BL, but the greater frequency of precipitation clouds constrained this offset resulting in greater precipitation rates over the warmer SSTs. Increasing the cloud nucleating aerosol concentration also enhanced the number of deeper congestus type clouds, but to a lesser extent than that of the SST experiments. The aerosol-induced suppression of the warm rain processes reduced the average surface

precipitation mass even as ice mass was increased. However, the distribution of clouds between cumulus and congestus type at times offset the decreased average precipitation rate per cloud.

The ability of these environmental factors to alter the vertical structure of the vertical velocity and the surface precipitation is important when considering the overall modification of the PCF regional water vapor field. While invigorating the updraft will increase the vertical water vapor mass flux, if the mass of water lost to precipitation is greater, then vertical flux of water vapor to the free troposphere will be lessened. While the B10 and B11 schematic emphasized the vertical mass flux by shallow clouds, they did not consider the other important factors impacting the fluxing of water vapor within the PCF region such as cloud entrainment and surface precipitation or the impacts of environmental factors on these processes. Here we have characterized the PCF clouds beyond the ability of the B10 and B11 studies by using a high resolution CRM. In the following section will be able to analyze the net effects of the PCF cloud field on the modification of the PCF regional moisture field.

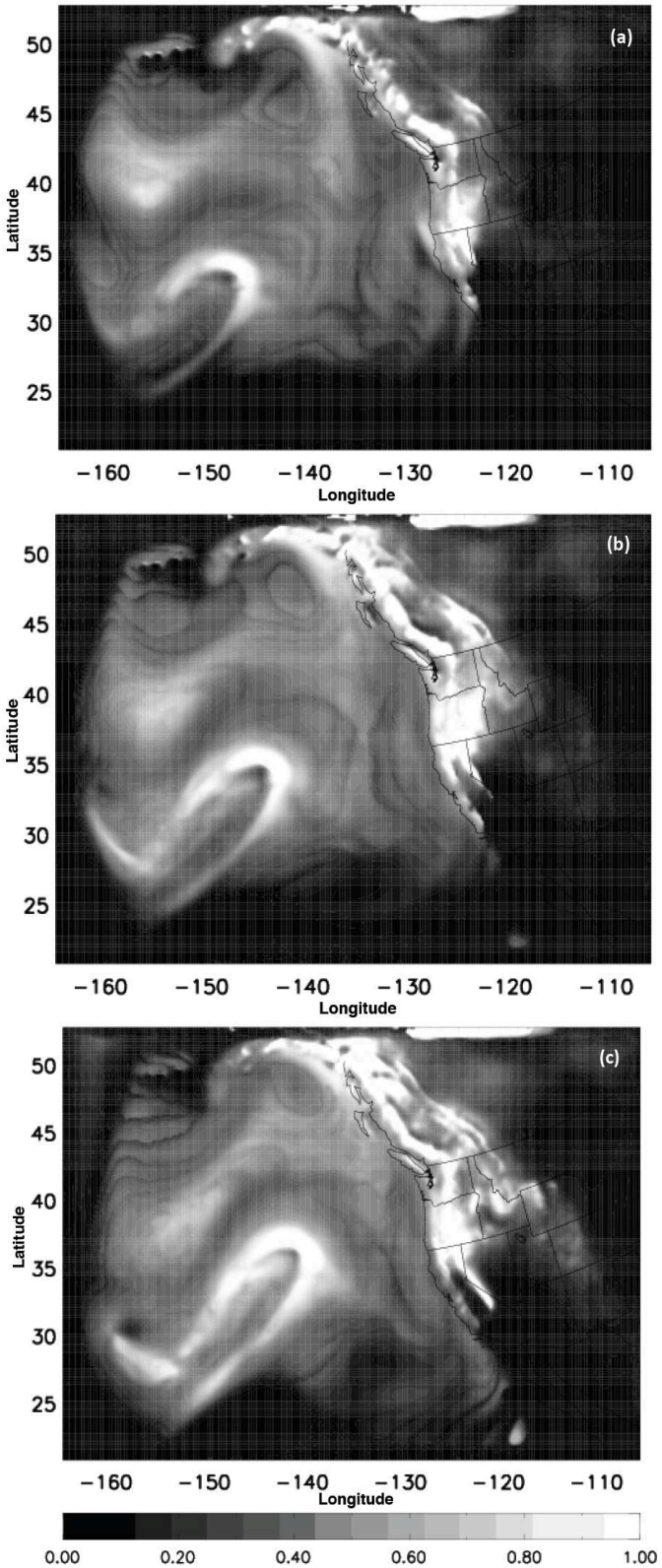

Figure 3.1: Grid 1 cloud fraction from the CL simulation at (a) 36 (12UTC 13 Jan), (b) 42 (18UTC 13 Jan), and (c) 48 (00UTC 14 Jan) simulation hours.

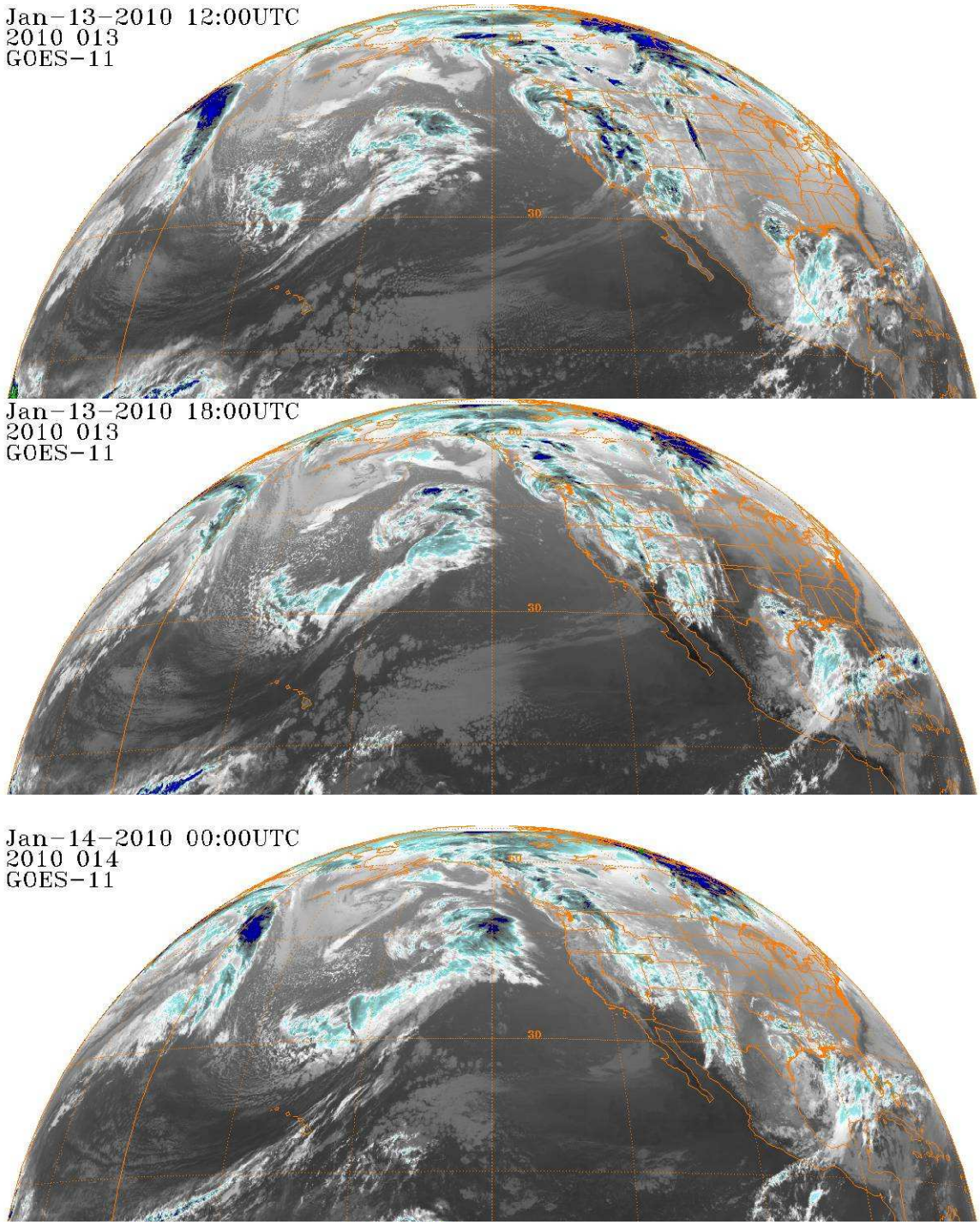

Figure 3.2: Infrared satellite images from GOES-11 from 12 and 18UTC on 13 Jan 2010 and from 00Z on 14 Jan 2010 over the Eastern Pacific Ocean. (http://www.ncdc.noaa.gov/gibbs/availability/2010-01-13)

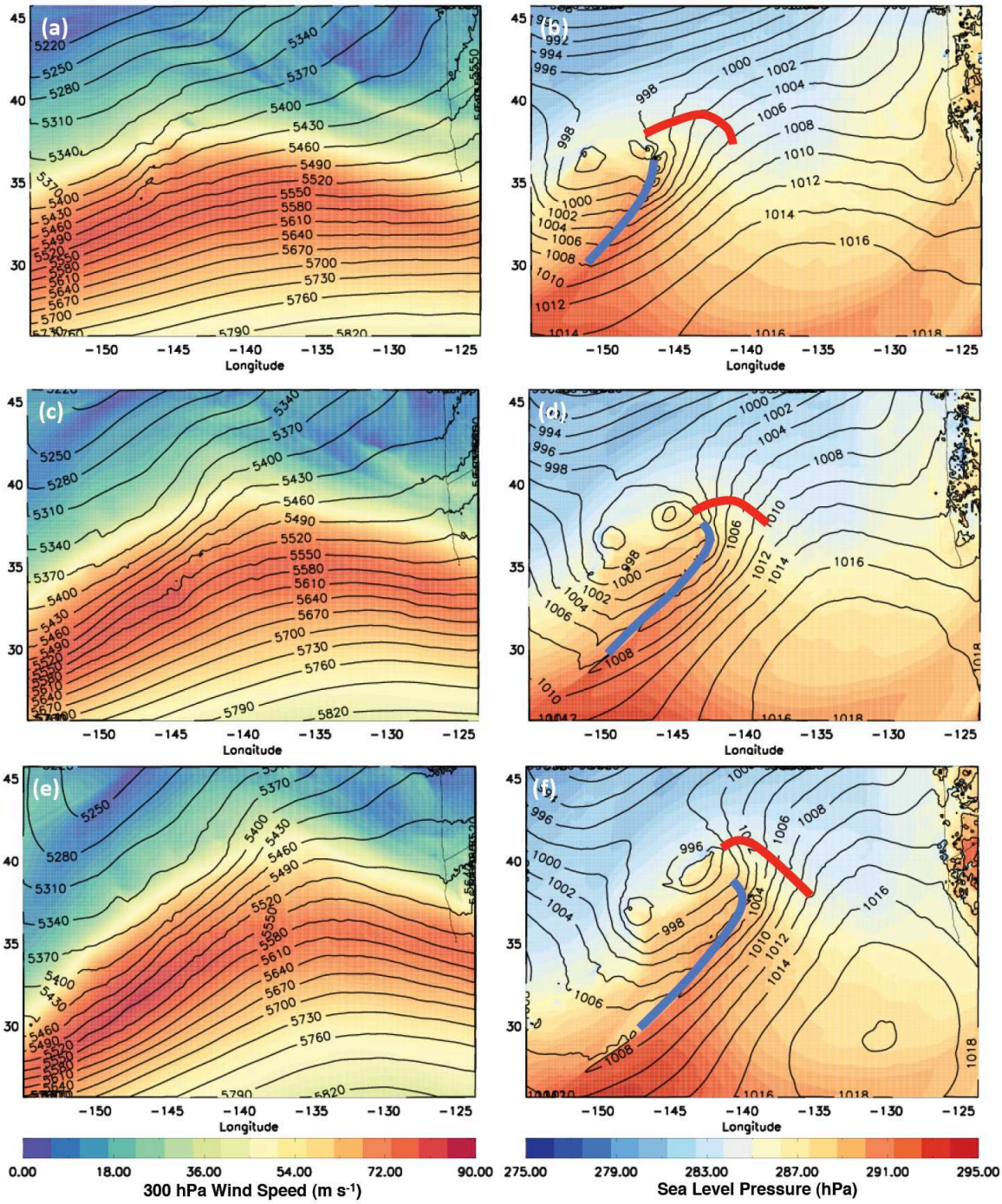

Figure 3.3: Plots of (a,c,e) the 300-hPa wind speed (shaded; m s^{-1}) and 500-hPa geopotential height (contoured; m), and (b,d,f) surface potential temperature (lowest model level; 40 m above the sea surface) (shaded; K) and sea level pressure (contoured; hPa) from Grid 2 for the CL simulation at 36, 42, and 48 simulation hours, respectively. Estimates of the location of the warm front (thick red line) and primary cold front (thick blue line) locations are drawn on panels (b, d, f).

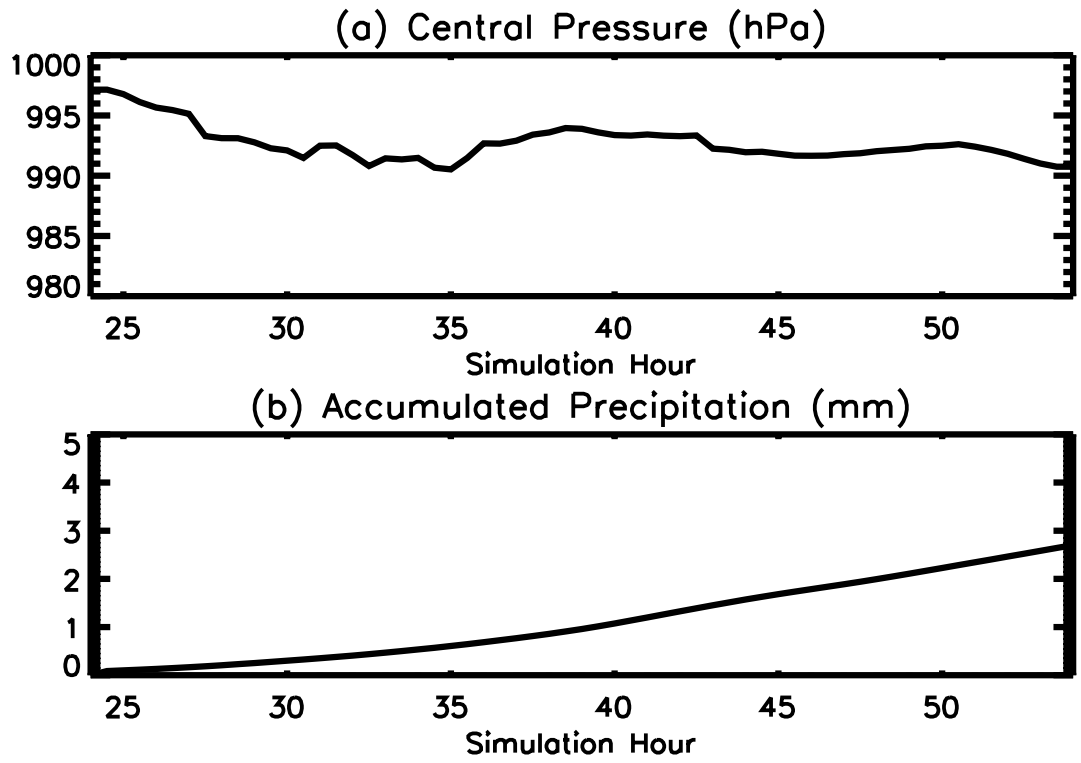

Figure 3.4: (a) Low pressure center of the ETC (hPa) and (b) grid domain wide accumulated ETC precipitation (mm) on Grid 2 for the CL simulation. The time series begins after the first 24 simulation hours (00 UTC 13 January 2010) in order to account for the ETC spin up.

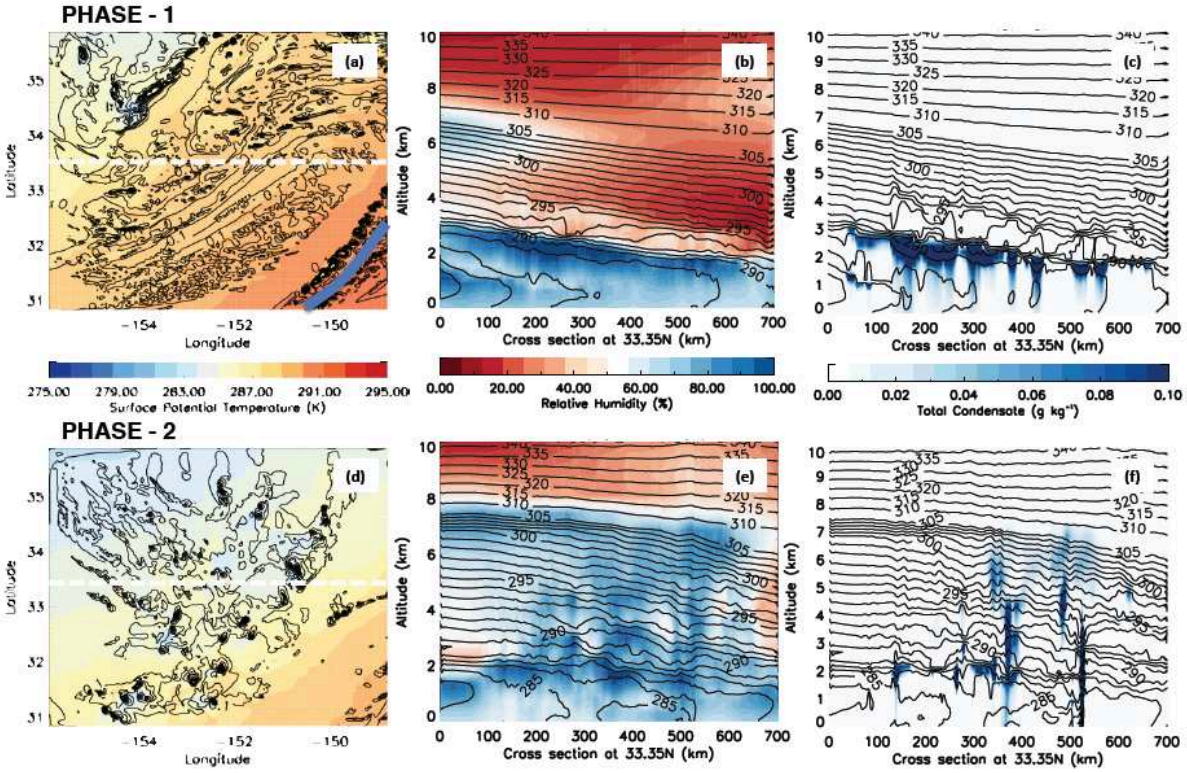

Figure 3.5: Characteristics of the PCF region for two time periods (14UTC 13 Jan 2010 (a-c) and 00UTC 14 Jan 2010 (d-f)) during PHASE-1 and PHASE-2, respectively, for the CL simulation: (a,d) Plan view of Grid 3 surface potential temperature (lowest model level, 40 m above the sea surface) (shaded; K) and vertically integrated condensate (0.1 mm contours). (b,e) East-west cross section at 33.35^{o}N of Grid 3 (dashed white line on panels (a) and (d)) of average (+/- 50 km in the north-south direction) relative humidity (shaded; %) and potential temperature (contour; K); and (c,f) total condensate (shaded; g kg^{-1}) and potential temperature (contour; K). Potential temperature contours are every 1 K in the lower troposphere and 5 K (> 305 K) in the upper troposphere. The approximate location of the cold front is identified on panel (a) (thick blue line).

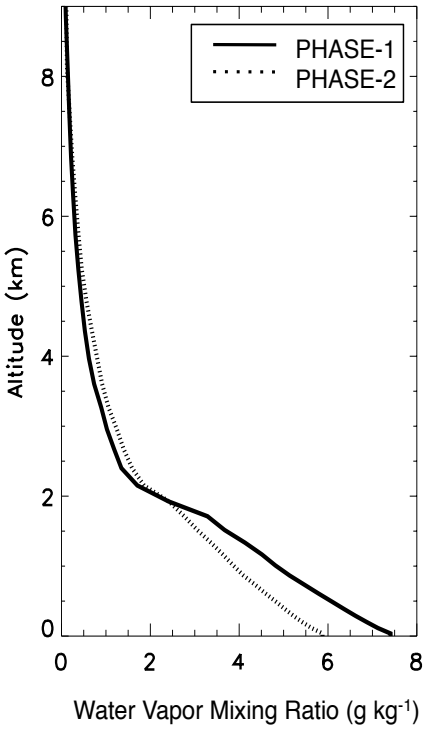

Figure 3.6: Vertical profiles of the average PCF environmental water vapor mixing ratio (g kg^{-1}) for PHASE-1 and PHASE-2 within Grid 3 of the CL simulation shown in figure 3.5. These profiles are averaged over the cloud-free regions.

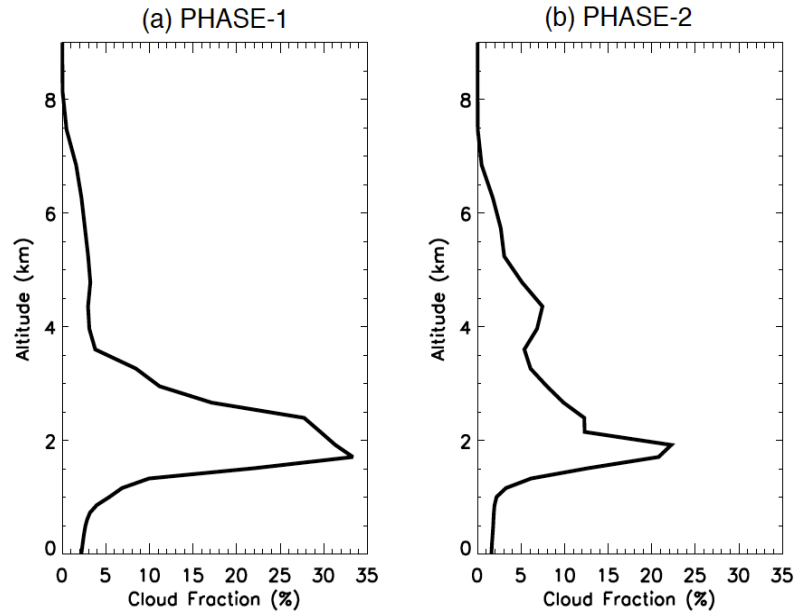

Figure 3.7: Profiles of PCF cloud fraction (%) within Grid 3 for the CL simulation for (a) PHASE-1 and (b) PHASE-2. Grid points are assumed to be cloudy where the total condensate is greater than 0.1 g kg^{-1}.

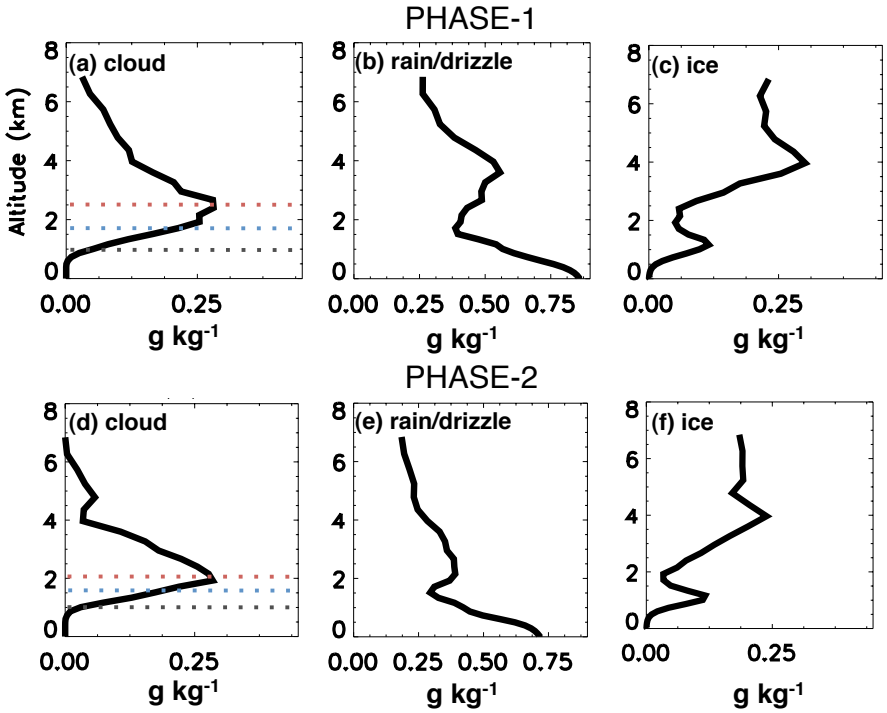

Figure 3.8: Vertical profiles of the PCF spatially- and temporally-averaged mixing ratio (g kg^{-1}) of (a,d) cloud, (b,e) rain+drizzle, and (c,f) total ice for PHASE-1 (a-c) and PHASE-2 (d-f) within Grid 3 of the CL simulation. These averages are taken over points where total condensate is greater than 0.1 g kg^{-1}. The dashed lines on panels (a) and (d) represents the approximate altitude of cloud base (black), the freezing level (blue) and the BL inversion (red) of each phase.

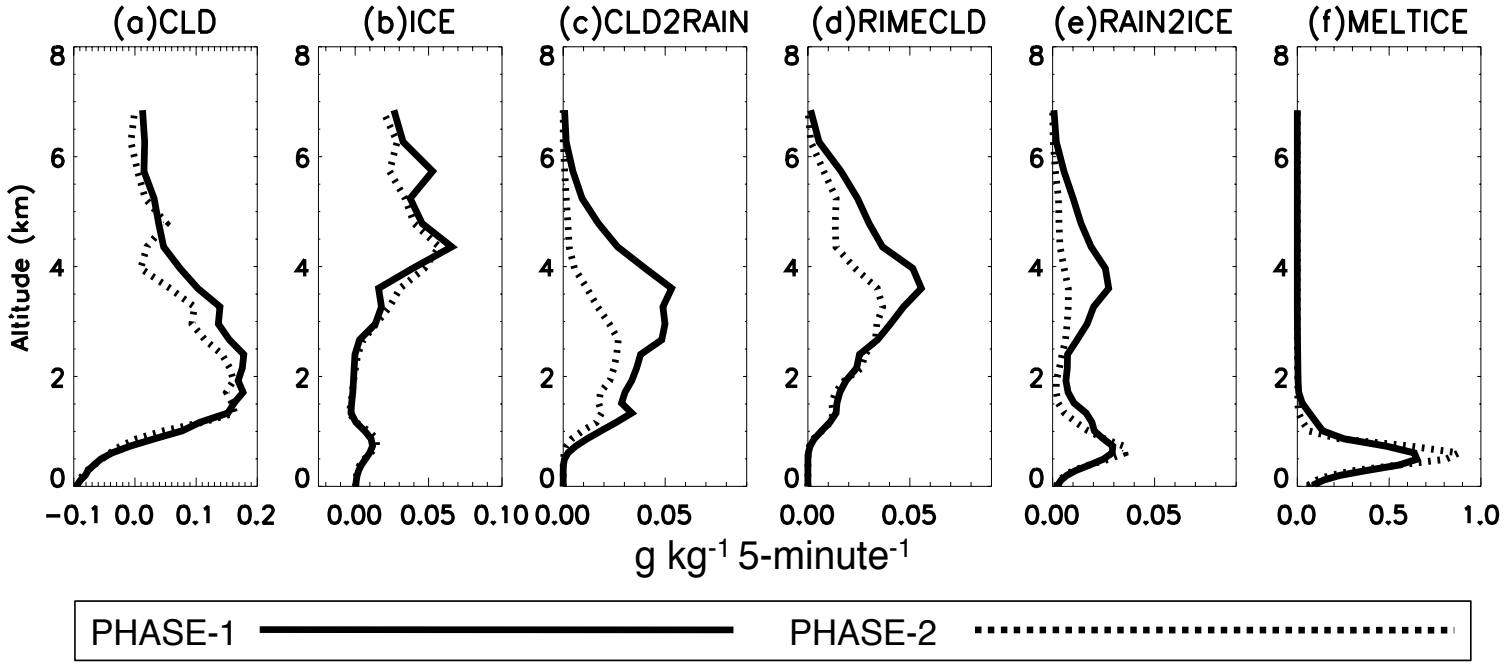

Figure 3.9: Vertical profiles of the PCF spatially- and temporally-averaged rate (g kg^{-1} 5-minute^{-1}) of (a) nucleation of cloud droplets and evaporation/condensation onto liquid hydrometeors (CLD) and (b) nucleation of ice and sublimation/deposition onto ice hydrometeors (ICE), (c) collision-coalescence of cloud droplets onto raindrops (CLD2RAIN), (d) riming of cloud water by ice (RIMECLD), (e) accretion of rain onto ice (RAIN2ICE), and (f) melting of ice (MELTICE) for PHASE-1 and PHASE-2 within Grid 3 of the CL simulation. These averages are taken over points where total condensate is greater than 0.1 g kg^{-1}. Note that the x-axis scales are different per panel.

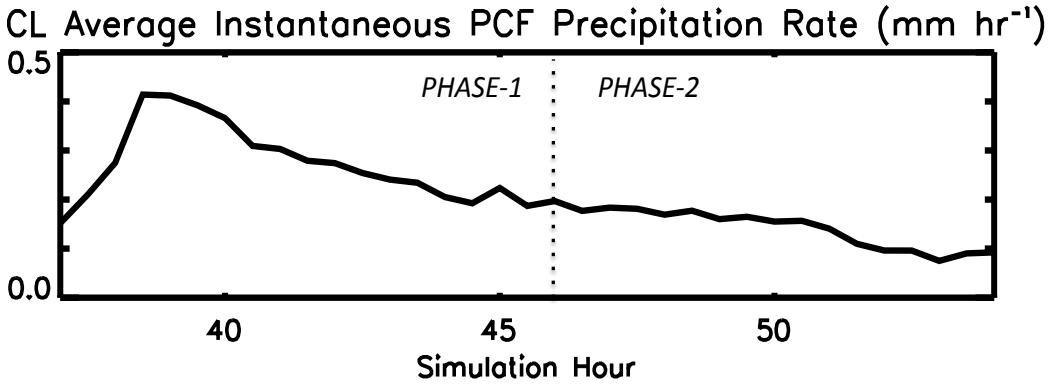

Figure 3.10: Average instantaneous precipitation rate (mm hr^{-1}) of the PCF region on Grid 3 from the CL simulation. Average includes non-precipitating grid points. A dashed lined demarcates PHASE-1 (38 – 46 simulation hours) and PHASE-2 (46 – 54 simulation hours).

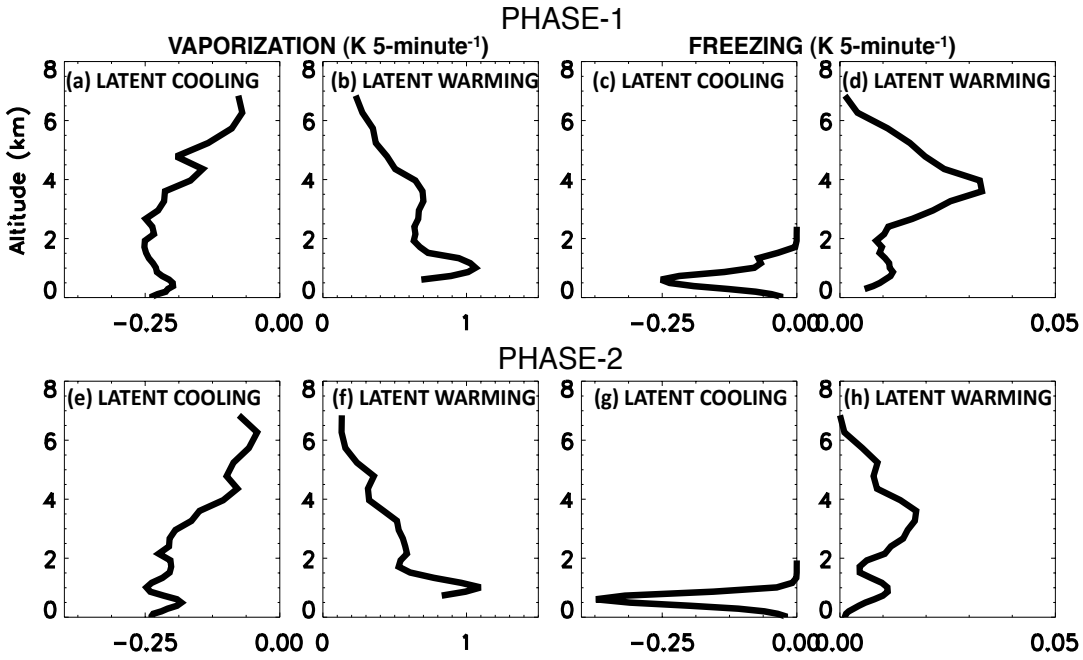

Figure 3.11: Vertical profiles of the PCF spatially- and temporally-averaged rate (K 5-minute^{-1}) of (a,e) latent cooling and (b,f) latent warming due to vaporization and (c,g) latent cooling and (d,h) latent warming due to freezing for PHASE-1 (a-d) and PHASE-2 (e-h) on Grid 3 of the CL simulation. These averages are taken at points where total condensate is greater than 0.1 g kg^{-1}.

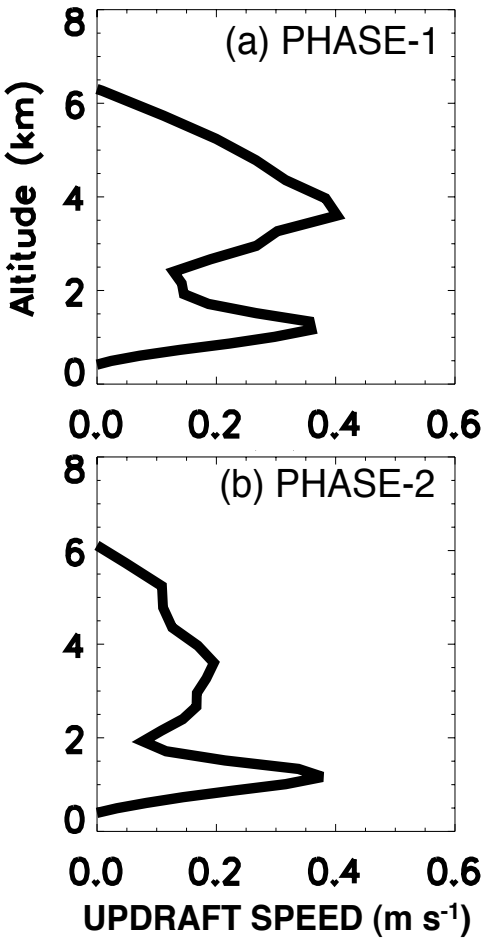

Figure 3.12: Vertical profiles of the PCF spatially- and temporally-averaged updraft speed (m s^{-1}) for (a) PHASE-1 and (b) PHASE-2 within Grid 3 in the CL simulation. These averages are taken at points where total condensate is greater than 0.1 g kg^{-1}.

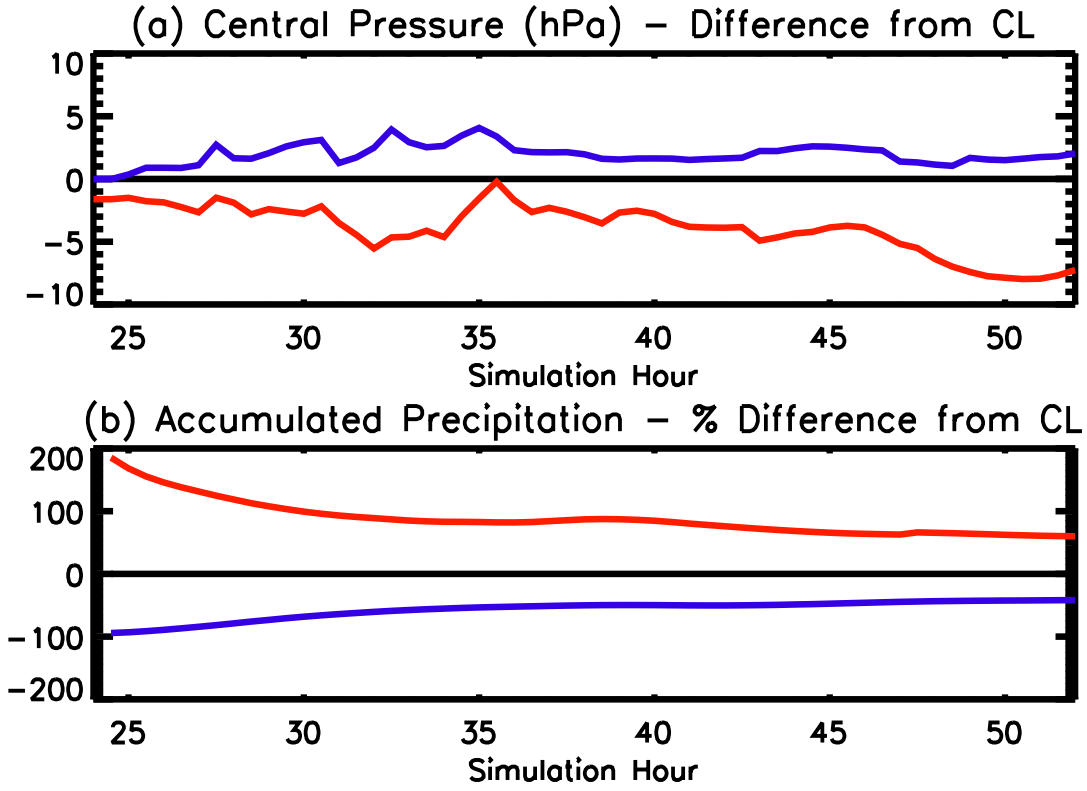

Figure 3.13: (a) Low pressure center of the ETC (hPa) and (b) grid domain wide accumulated ETC precipitation on Grid 2 for the -2KCL and +2KCL simulations, expressed as a difference from the CL simulation.

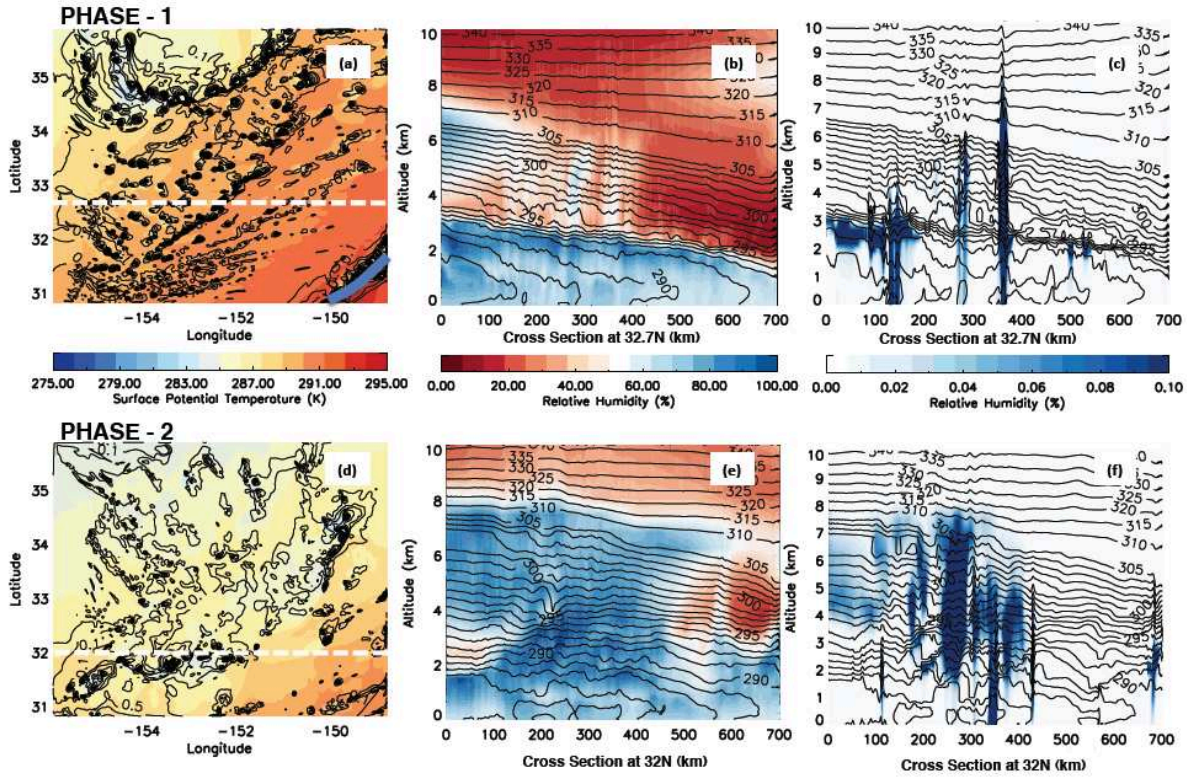

Figure 3.14: Same as figure 3.5 except for the +2KCL simulation.

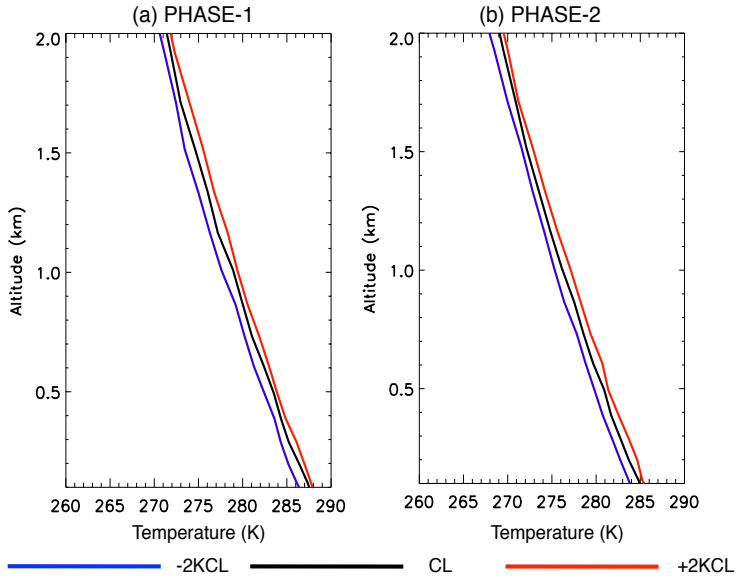

Figure 3.15: Spatially- and temporally-averaged ambient BL temperature profiles from Grid 3 over the PCF region for (a) PHASE-1 and (b) PHASE-2 for the -2KCL, CL, and +2KCL simulations.

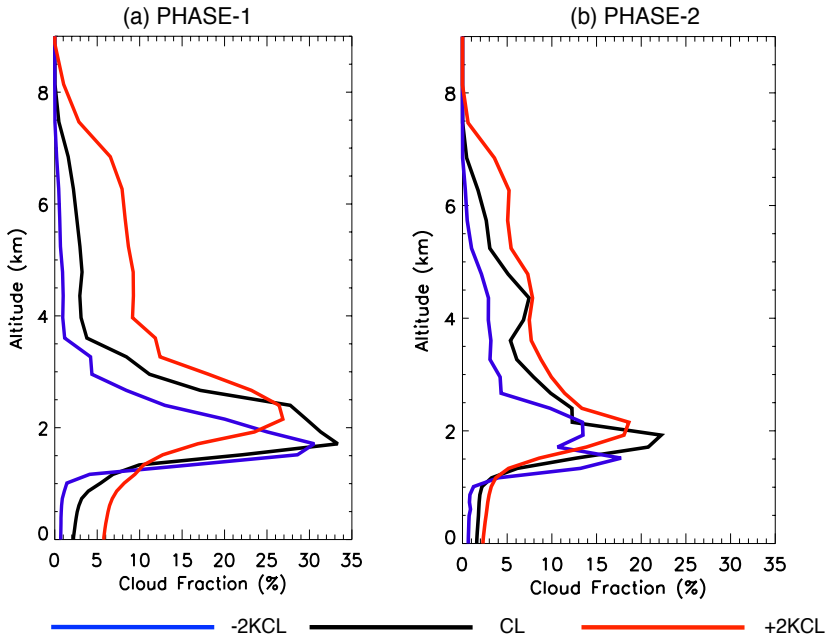

Figure 3.16: As for figure 3.7 but for the SST sensitivity experiments.

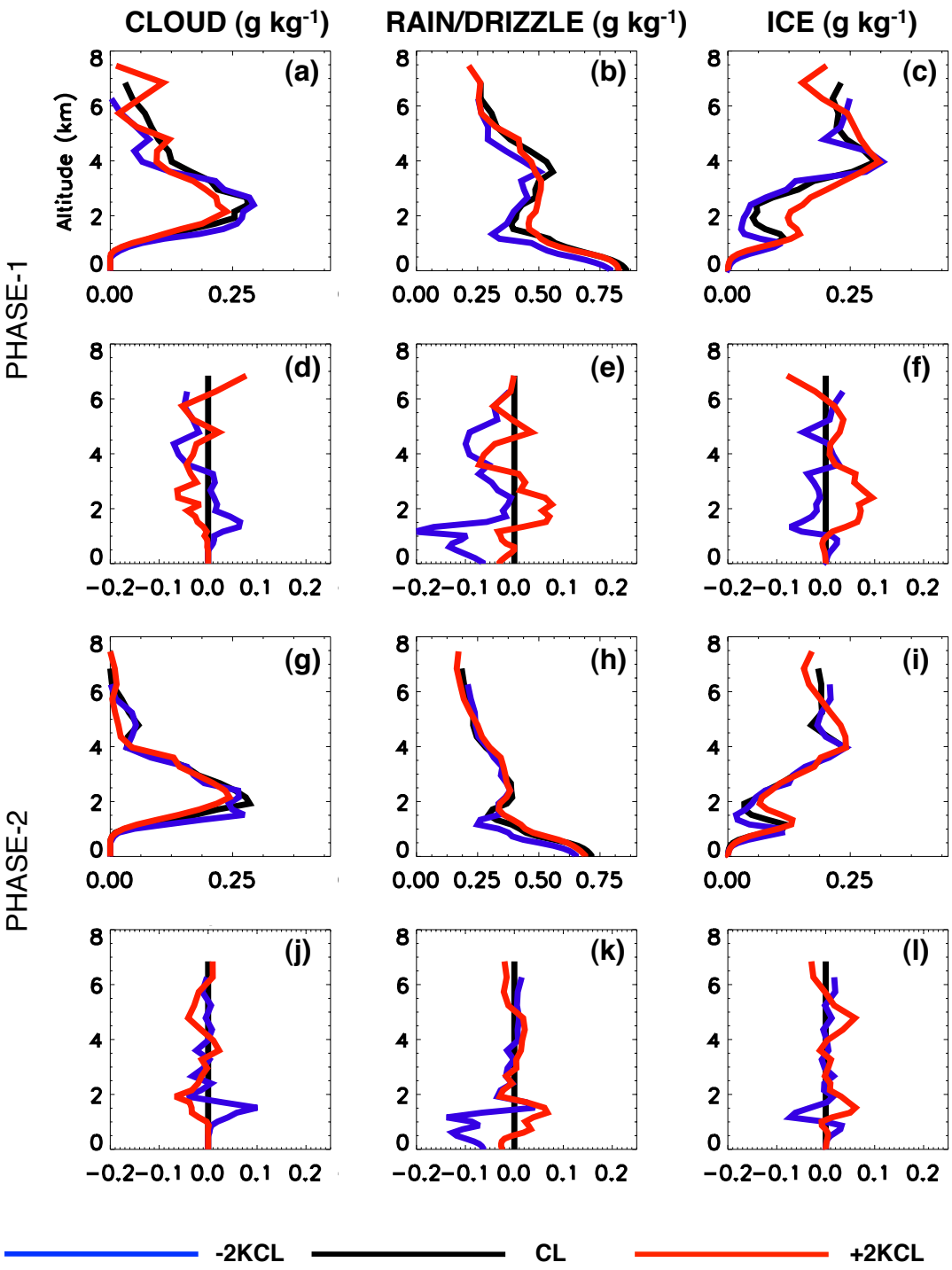

Figure 3.17: Vertical profiles of the PCF spatially- and temporally-averaged mixing ratio (g kg^{-1}) of (a,g) cloud, (b,h) rain+drizzle, and (c,i) total ice, for PHASE-1 (a-f) and PHASE-2 (g-l) of the CL, +2KCL, and -2KCL simulations. These averages are taken at points where total condensate is greater than 0.1 g kg^{-1}. Differences from the CL simulation are presented in panels (d)-(f) and (j)-(l) for each phase, respectively.

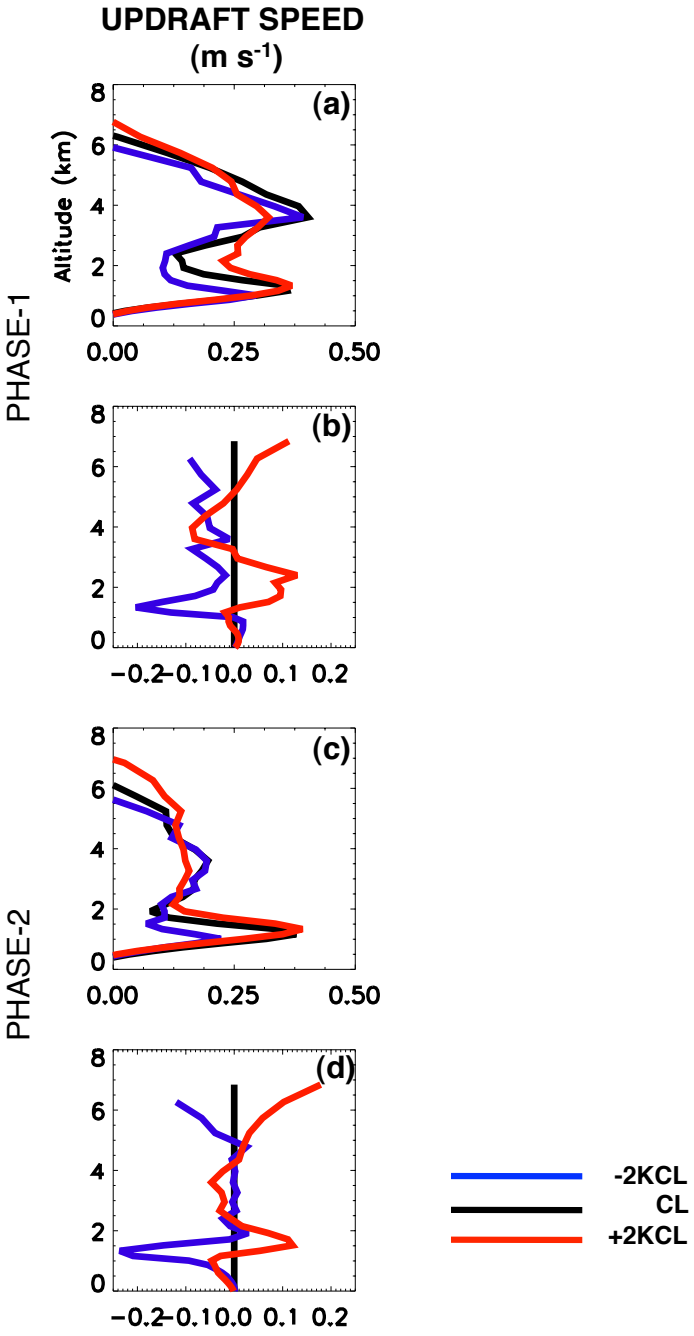

Figure 3.18: Vertical profiles of the PCF spatially and temporally averaged updraft speed (m s^{-1}) for PHASE-1 (a-b) and PHASE-2 (c-d) within Grid 3 in the CL, +2KCL, and -2KCL simulations. These averages are taken at points where total condensate is greater than 0.1 g kg^{-1}. Differences from the CL simulation are in panels (b) and (d) for the respective phases.

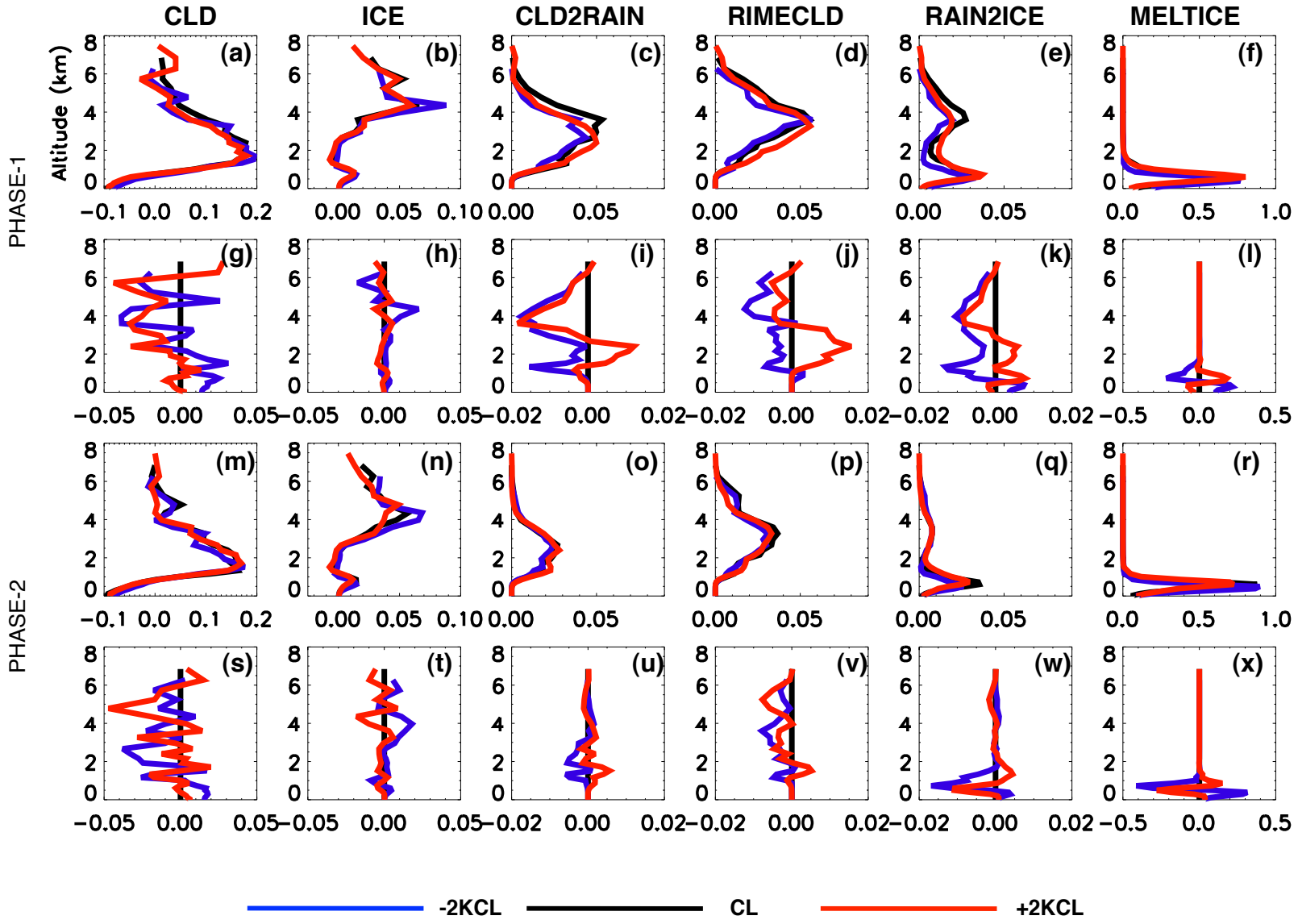
CLD
ICE
CLD2RAIN
RIMECLD
RAIN2ICE
MELTICE
PHASE-1
PHASE-2
Altitude (km)
(a)
(b)
(c)
(d)
(e)
(f)
(g)
(h)
(i)
(j)
(k)
(l)
(m)
(n)
(o)
(p)
(q)
(r)
(s)
(t)
(u)
(v)
(w)
(x)
-2KCL
CL
+2KCL

Figure 3.19: Vertical profiles of the PCF spatially- and temporally-averaged net rate (g kg^{-1} 5-$minute^{-1}$) of (a,m) nucleation of cloud droplets and evaporation/condensation onto liquid hydrometeors (CLD), (b,n) sublimation/condensation onto ice hydrometeors (ICE), (c,o) collision-coalescence onto raindrops (CLD2RAIN), (d,j) riming of cloud water (RIMECLD), (e,q) accretion of rain onto ice (RAIN2ICE), and (f,r) melting of ice (MELTICE) within Grid 3 for PHASE-1 (a-l) and PHASE-2 (m-x) of the CL, +2KCL, and -2KCL simulations. These averages are taken at points where total condensate is greater than 0.1 g kg^{-1}. Differences from the CL simulation are in panels (g)-(l) and (s)-(x) for each respective phase.

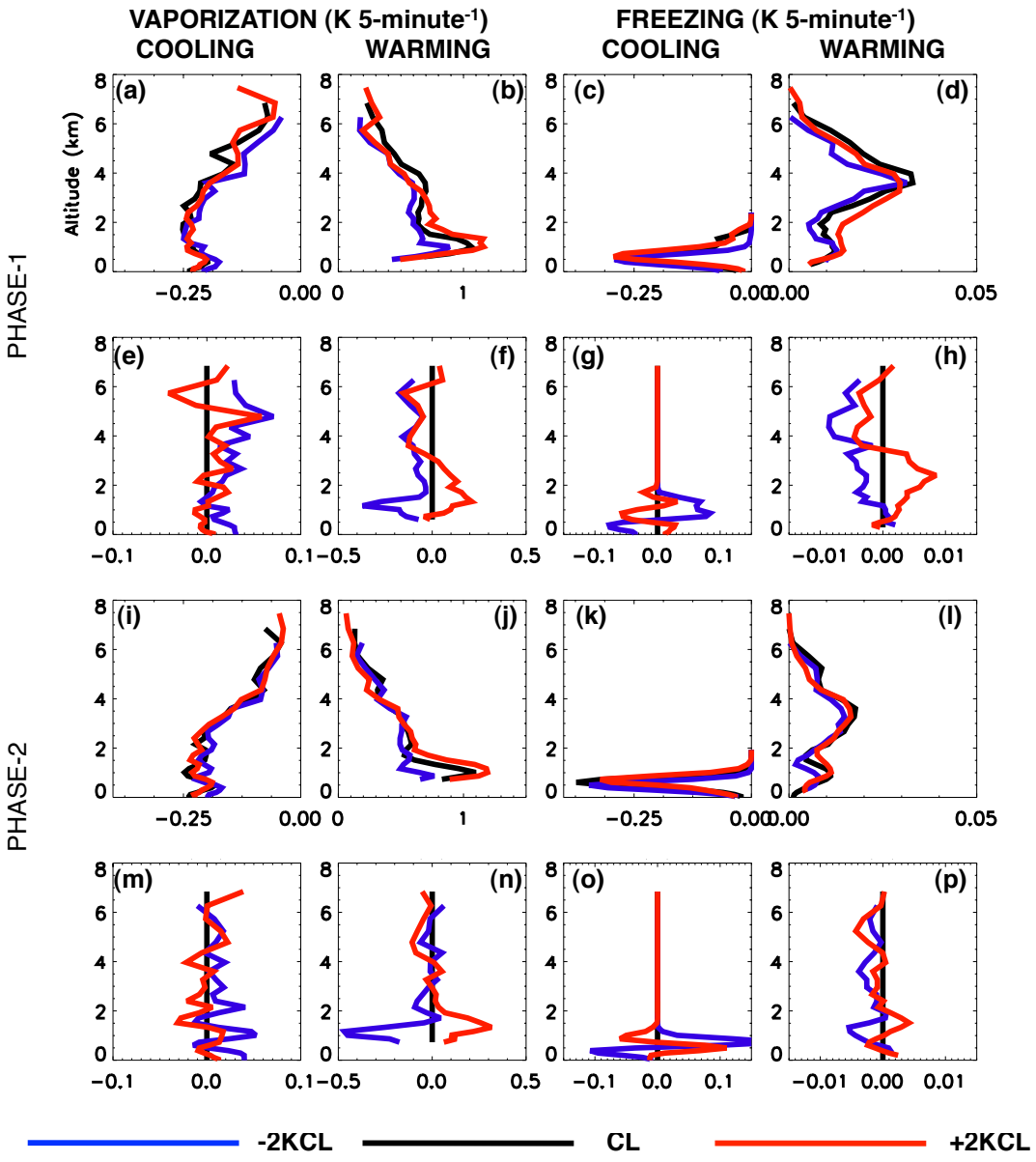

Figure 3.20: Vertical profiles of the PCF spatially- and temporally-averaged rate (K 5-minute^{-1}) of (a,i) latent cooling and (b,j) latent heating due to vaporization and (c,k) latent cooling and (d,l) latent heating due to freezing for PHASE-1 (a-h) and PHASE-2 (i-p) within Grid 3 of the CL, +2KCL, and -2KCL simulations. These averages are taken at points where total condensate is greater than 0.1 g kg^{-1}. Differences from the CL simulations are in panels (e)-(h) and (m)-(p) for the respective phases.

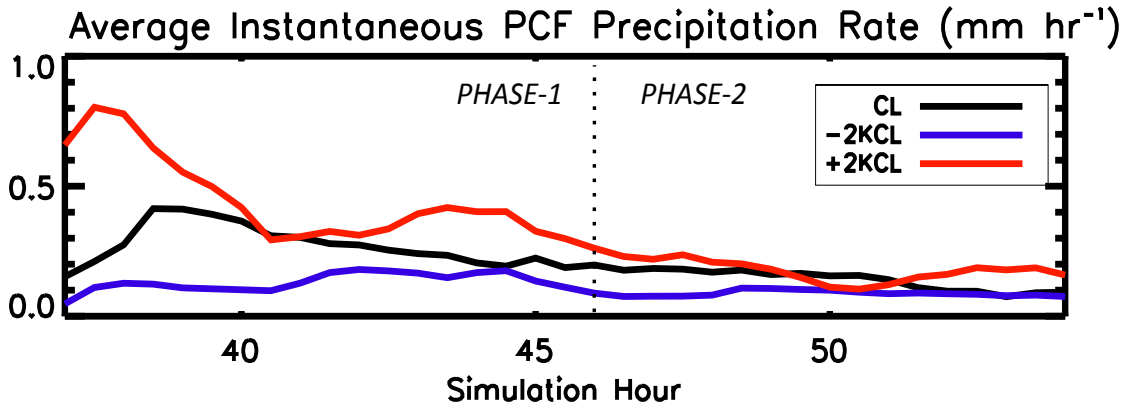

Figure 3.21: As for figure 3.10 but for the SST sensitivity experiments.

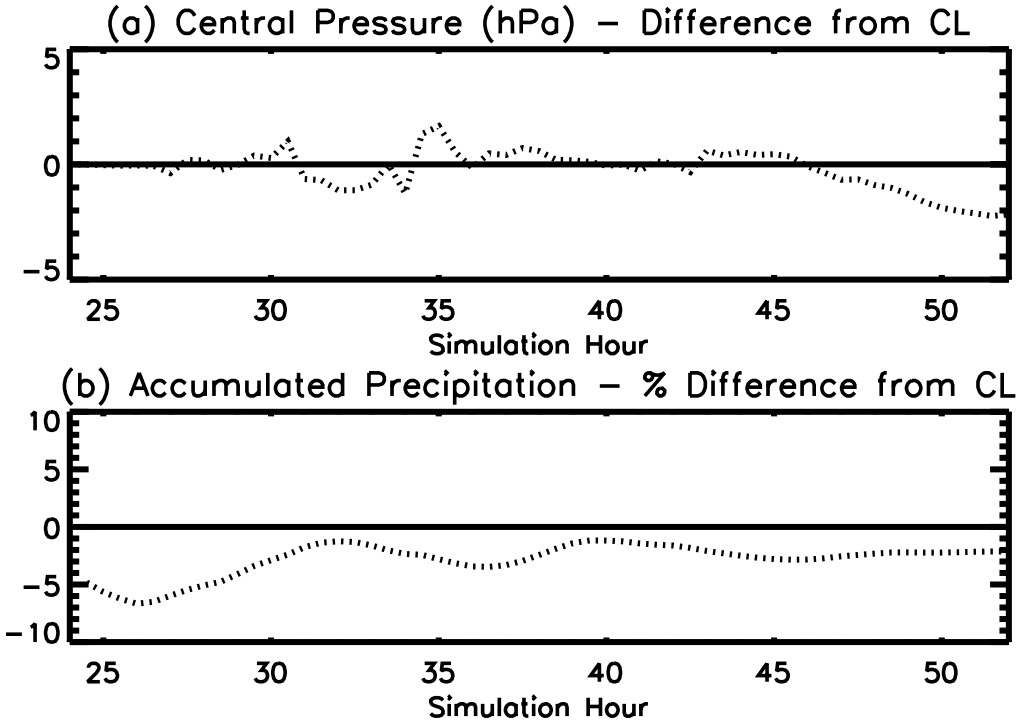

Figure 3.22: As for figure 3.13 but for the aerosol sensitivity experiment.

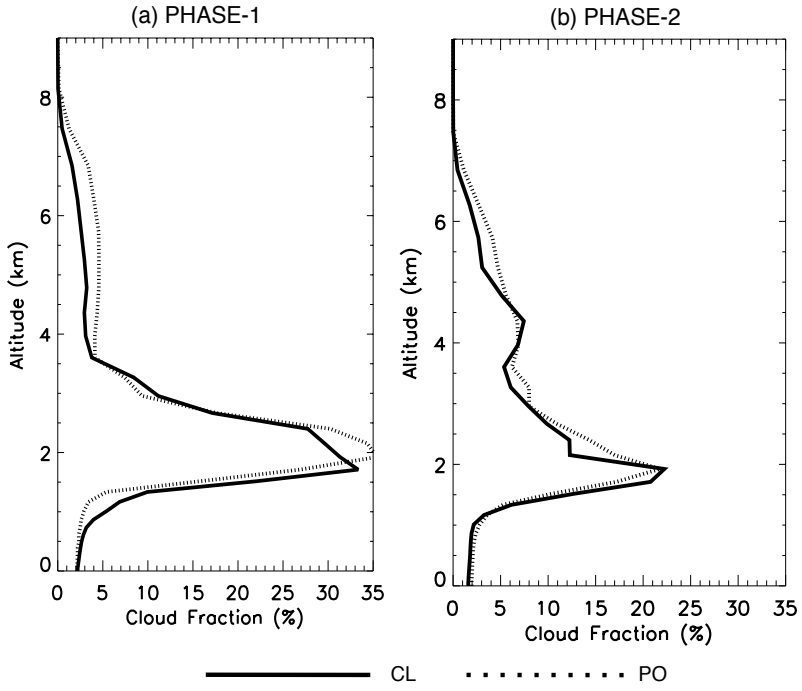

Figure 3.23: As for figure 3.16 but for the aerosol sensitivity experiment.

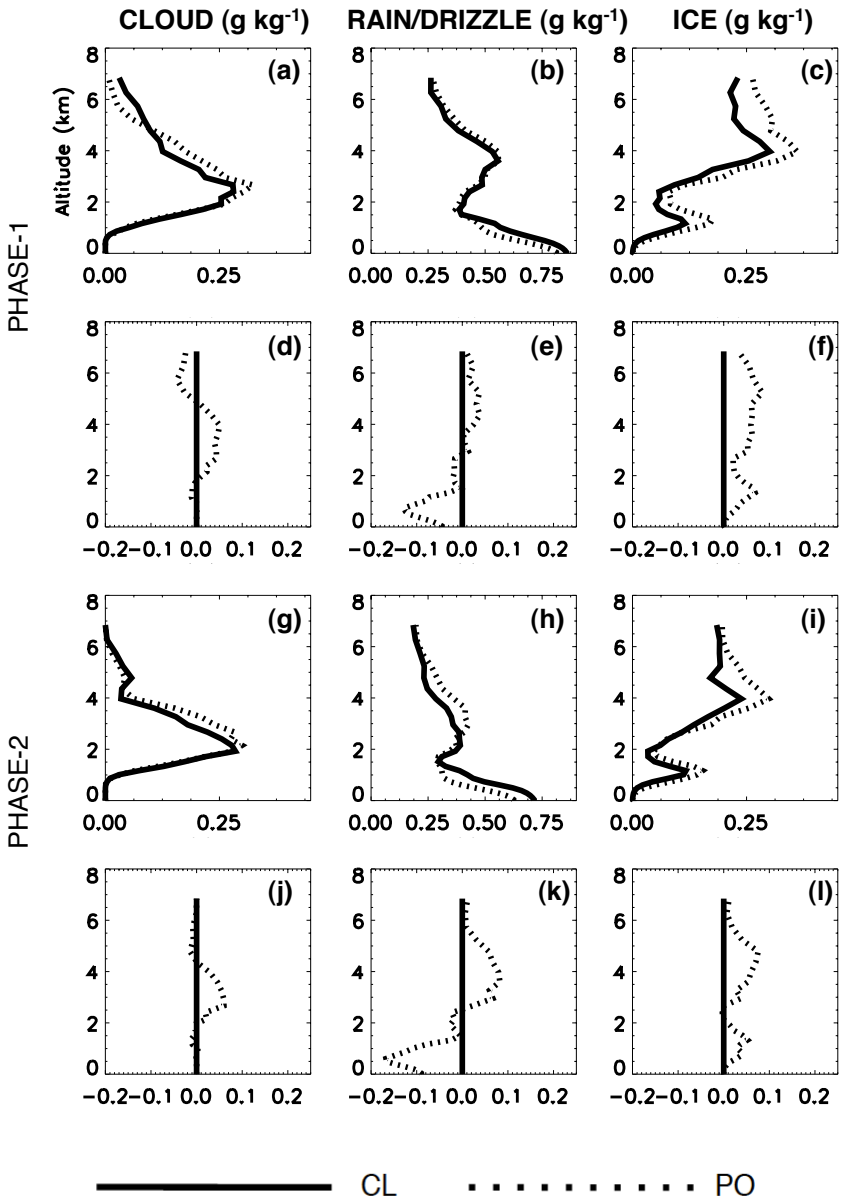

Figure 3.24: As for figure 3.17 but for the aerosol sensitivity experiment.

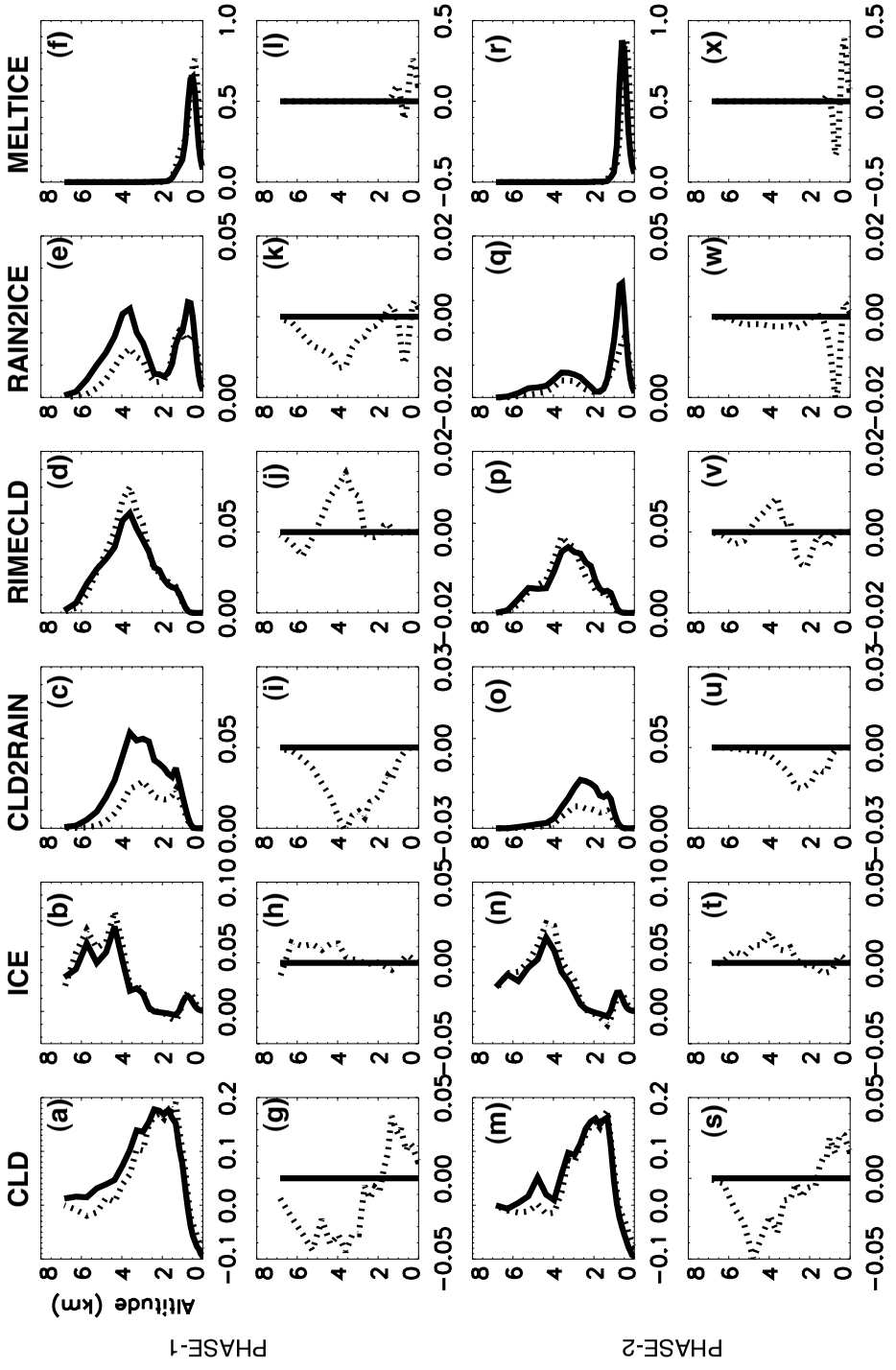

Figure 3.25: As for figure 3.19 but for the aerosol sensitivity experiment.

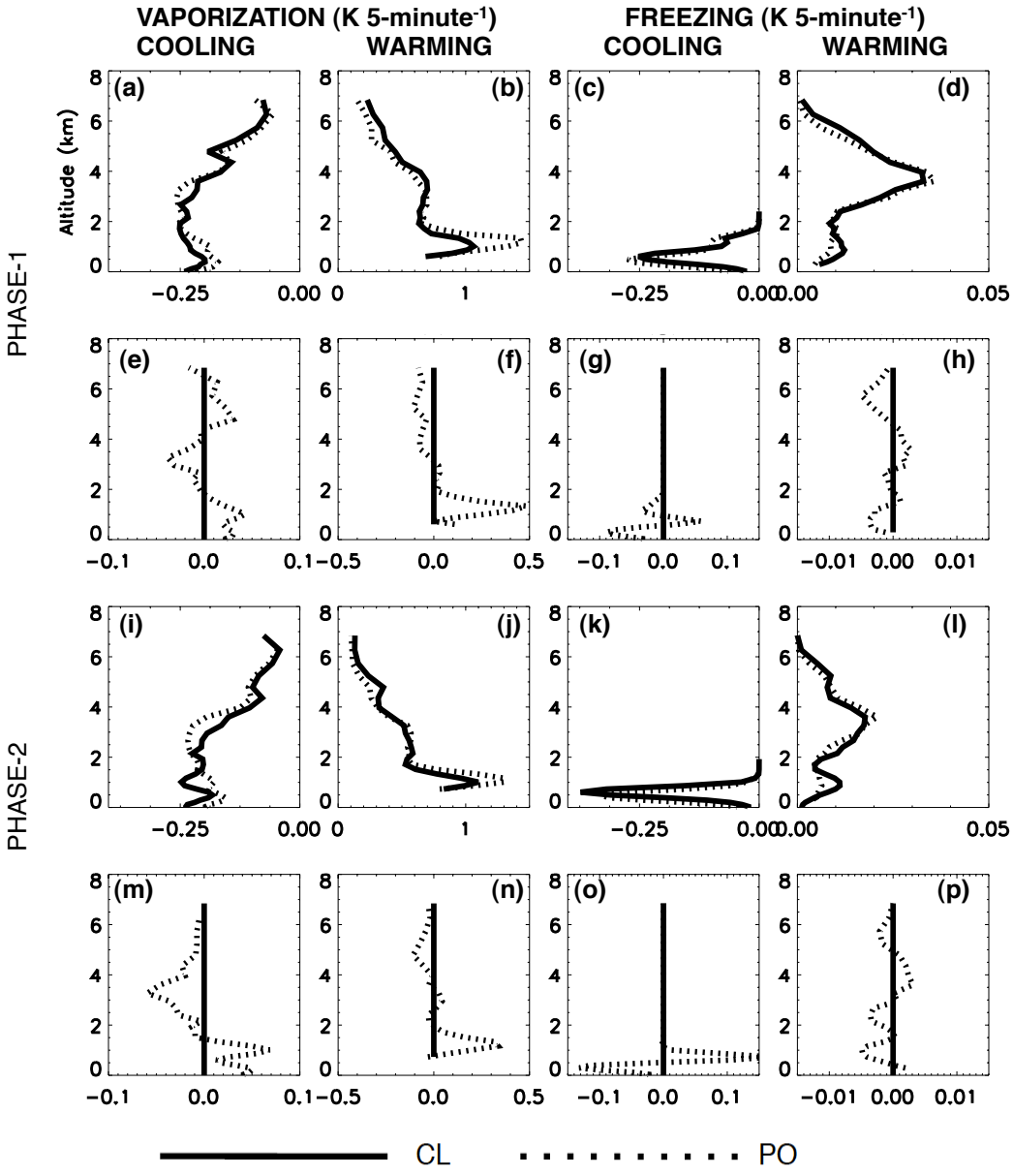

Figure 3.26: As for figure 3.20 but for the aerosol sensitivity experiment.

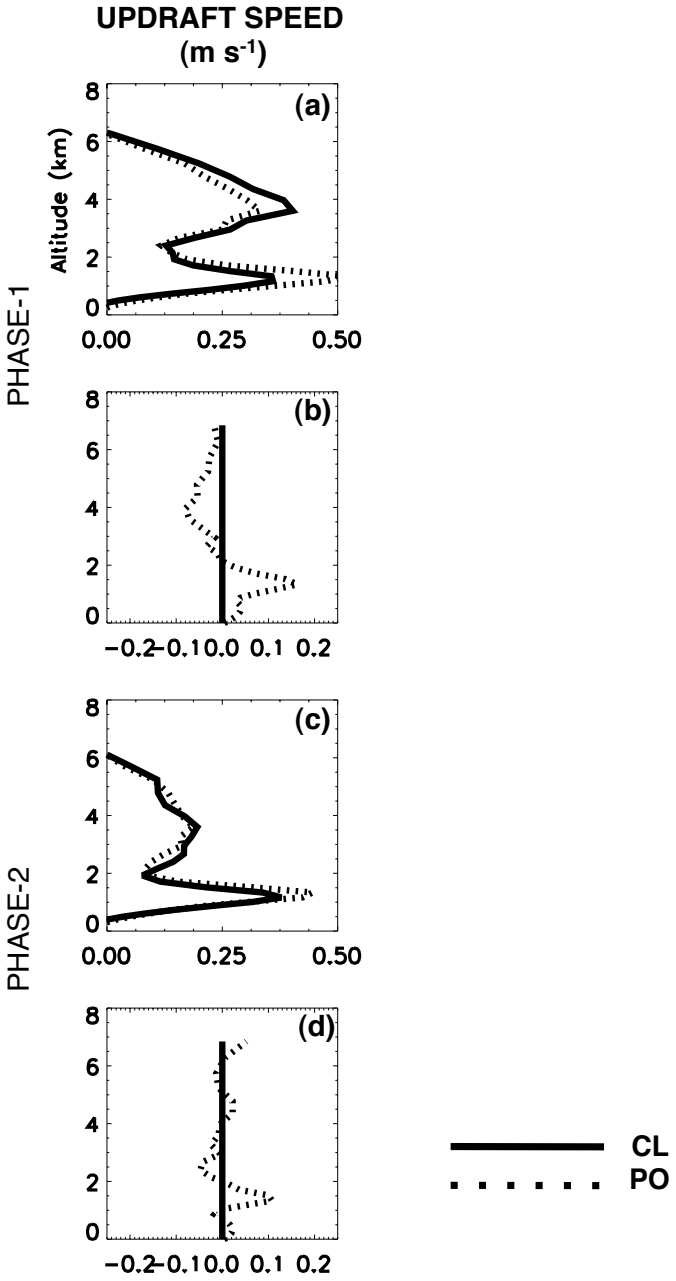

Figure 3.27: As for figure 3.18 but for the aerosol sensitivity experiment.

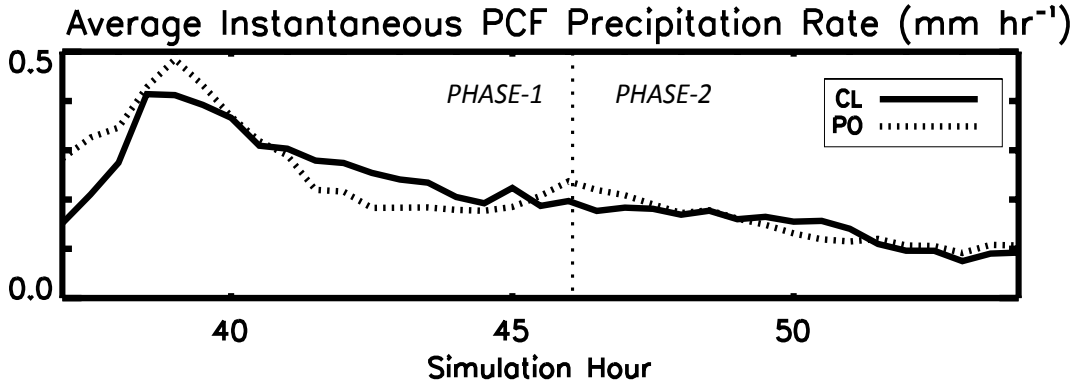

Figure 3.28: As for figure 3.21 but for the aerosol sensitivity experiment.

4. WATER VAPOR MASS FLUX AND WATER VAPOR BUDGET OF THE POST-COLD FRONTAL REGION

4.1 INTRODUCTION

Examination of the PCF cumulus clouds' microphysical and dynamical structure in the previous chapter highlighted the importance of the variations in the environmental characteristics of PHASE-1 and PHASE-2, as well as variations in SST and aerosol loading, to the latent heating structure, strength of the updrafts, and the surface precipitation of these clouds. The strength of the BL inversion as well as the BL moisture content in PHASE-1 promoted the development of shallow PCF cumulus clouds interspersed with only a few strong congestus clouds, while the BL drying and free troposphere instability present during PHASE-2 reduced the overall cloud fraction, in particular the shallow cumulus clouds but enhanced the congestus cloud frequency. Increasing the SST not only increased the average updraft speed of PCF clouds in the lower troposphere resulting in a greater number of congestus clouds, but also increased the average surface precipitation mass. Increasing the concentration of available cloud-nucleating aerosol resulted in both an invigoration of the updraft and a reduction in the average surface precipitation mass.

The goal of this chapter is to examine the role of PCF clouds in the water vapor budget in the PCF region of ETCs. This is a function of each individual cloud's vertical water vapor mass flux, as well as the cumulative number of clouds in the region. Figure 4.1 is a schematic, modified after B10 and B11, showing the ways in which PCF cumulus clouds can potentially impact the PCF regional water vapor field, including those processes transporting water vapor to and from the BL. Using relatively coarse global model simulations of an idealized ETC, B10 and

B11 identified the importance of the cumulative PCF cloud ventilation of moisture from the ETC BL in comparison to that associated with the WCB. They also identified that surface evaporation in the PCF region is an important source of the water vapor for the WCB, being advected from the PCF region to the WCB origin within the BL. However, the B10 and B11 schematic omitted several potentially important cloud-scale features of PCF clouds that could contribute to the net vertical water vapor mass flux within the PCF region. Our ability to examine the individual cloud structure and the integrated impacts of the PCF cloud field using a CRM allows us to better understand the relative contributions of various cloud-scale processes to the net vertical and horizontal water vapor mass flux.

Numerous processes impact the water vapor budget within the PCF region (figure 4.1). As discussed in B10 and B11, cumulus cloud development leads to an upward in-cloud flux of water vapor and condensate mass from the sea surface towards the top of the BL. If the cumulus cloud is able to penetrate through the inversion capping the BL, this flux of water vapor and condensate mass can extend into the free troposphere from where it may be advected over large distances by the mid- and upper-tropospheric winds. Advection of moisture occurs into and out of the PCF region, and may serve as a water source for other regions of the ETC as suggested by B10. Turbulence can also vertically flux water vapor mass within the BL and to the free troposphere across the BL inversion. However, B10 found the net turbulent contribution of the BL to the free troposphere transport to be small. We will be able to explore several of the additional processes shown in figure 4.1 with our CRM simulations. These include: (1) the evaporation and detrainment of cloud condensate which can return water vapor to the troposphere through evaporation at different vertical locations; (2) downdrafts near cloud edges and below cloud base which may flux water vapor into the BL from the free troposphere; (3)

large-scale ambient environmental subsidence which can also contribute to BL water vapor contents; and (4) precipitation that falls toward the surface, from where it may evaporate and/or possibly reach the surface.

Figures 4.2 and 4.3 show examples of several of the surface processes demonstrated in figure 4.1. These plan views are of the PCF region on Grid 3, six hours after the grid was included in the CL simulation. Figure 4.2 shows (a) the surface latent heat flux ($\rho_a C_p U_* r_*$) (shaded; W m^{-2}), (b) the surface sensible heat flux ($\rho_a C_p U_* \theta_*$) (shaded; W m^{-2}), and (c) the surface instantaneous precipitation (shaded; mm hr^{-1}), overlaid with vertically integrated total condensate (mm) contoured at 0.5 mm intervals. Surface fluxes are a function of the air density (ρ_a; kg m^{-3}), surface wind speed (U_*; m s^{-1}), and the temperature (θ_*; K) and water vapor content (r_*; kg_{water} kg_{air}^{-1}) differences between the lowest atmospheric level and the sea surface (indicated by the "*"). C_p is the specific heat of water vapor at constant pressure. Similarly, figure 4.3 shows the vertical water vapor mass flux ($q_v w \rho_a$) (shaded; kg m^{-2} s^{-1}) at 1 km ASL. Vertical water vapor mass flux is the product of the water vapor mixing ratio (q_v; kg_{water} kg_{air}^{-1}), vertical velocity (w; m s^{-1}), and air density. The 1 km ASL altitude was chosen because, as will be shown later, the largest PCF vertical water vapor fluxes occur near this level in the PCF BL. Both the latent and sensible heat fluxes in the CL simulation are positive throughout the grid domain at this time (figure 4.2a,b) and are greatest near areas of strong winds and/or large temperature or water vapor differences between the air and surface, such as in the cold pools or behind the cold front (figure 4.2c). Upward water vapor mass flux at 1 km ASL occurs near the updraft cores of convection and also within the ambient rising motion, such as associated with cold pools induced by convection (figure 4.3). Couplets of upward and downward water vapor mass flux near clouds are evident in figure 4.3, as is larger-scale subsiding motion. For example, a cloud-free region of

subsidence associated with the DCB to the west of the cold front is evident, followed further to the west by numerous couplets of upward/downward flux associated with PHASE-1 PCF clouds. As discussed in Chapter 3, PCF clouds in PHASE-1 were found to be primarily BL capped cumulus clouds, with a few deeper congestus type clouds. The ability of these few strong congestus clouds to reach above the BL inversion impacted their subsequent cloud microphysical development. Mesoscale organization assists in lofting these clouds above the BL. Throughout the domain there are long, thin filaments of upward water vapor mass flux that are associated with cold pools and other regions of convergence, while the patches of light blue coloring show large-scale subsiding air outside of clouds (figure 4.3). These regions of convergence support the enhanced development of some of the cumulus beyond the BL inversion. Such mesoscale processes are missing from the convective parameterizations of GCMs such as used in B10 and B11.

With our high resolution CRM simulations of a PCF region, we will be able to examine the cumulative impacts of each of the local cloud scale processes in detail, as well as those processes impacted by the larger-scale ETC processes (i.e. advection, surface evaporation) in order to assess what role PCF clouds play in the PCF regional water vapor budget. In order to examine the impact of the net cloud field, we will look at the bulk PCF processes. By this we mean we will look at the Grid 3 domain-wide changes in water vapor, cloud condensate, surface evaporation, surface precipitation, and water vapor advection to obtain a water vapor budget for Grid 3, which covers a significant portion of the PCF region. First we will examine these processes for the CL simulation followed by those for the SST and aerosol sensitivity simulations (+/-2KCL and PO). All of the following budgetary analysis will be performed for Grid 3 unless stated otherwise.

4.2 VERTICAL DISTRIBUTION OF WATER VAPOR MASS IN THE PCF REGION

A. THE CL SIMULATION

Figure 4.4 shows a time series of the atmospheric integrated water vapor mass (IWV) for the CL simulation. The simulated water vapor mixing ratio is vertically and horizontally integrated over the grid domain in order to obtain the total grid domain IWV (kg) using the following equation:

$$IWV = \iint q_v \rho_a dz dA \tag{4.1}$$

where dz (m) is the depth of each model level and dA (m^2) is the horizontal area of the Grid 3 domain, and the other terms are as defined previously. The IWV is first shown as over the entire depth of the atmosphere (figure 4.4.a), and is then examined over three layers: (b) surface to 1 km (sub-cloud layer), (c) 1 km to 2.4 km (cloud layer), and (d) 2.4 km to the top of the atmosphere (TOA) (free troposphere layer). Panels (b-d) are shown as a percentage of the IWV (panel a) in each layer. These layers were chosen as cloud base in these simulations is found near 1 km ASL and the BL inversion is near 2-2.5 km ASL depending on the environmental conditions. The dashed line at 46 hours differentiates PHASE-1 from PHASE-2. Figure 4.5 shows the temporally-averaged IWV for both PHASE-1 and PHASE-2 for the CL and each of the sensitivity tests (PO, -2KCL, +2KCL). As the SST in the PCF domain does not vary with time, variations in the surface fluxes will only be impacted by the ambient atmospheric thermodynamic conditions and the magnitude of the near-surface wind field.

The total IWV is found to decrease ~20% from the beginning of PHASE-1 to the end of PHASE-2 (figure 4.4a). In keeping with the results shown in Chapter 3, a moist sub-cloud BL overlaid by a relatively dry free troposphere characterizes PHASE-1, while in PHASE-2, weak free tropospheric moistening throughout the depth of the free troposphere occurs while the sub-

cloud BL and cloud layer become drier (figure 4.5). Thus, the decrease in IWV with time is due to the fact that the upper tropospheric moistening is insufficient to compensate for the BL drying. Therefore, in the progression from PHASE-1 to PHASE-2, the absolute magnitude of the total IWV decreases, the BL and cloud layer IWV decreases, and the free troposphere IWV increases (figure 4.5). A corresponding trend is evident in the percentage contributions of these layers to the total IWV (figure 4.4). The cloud layer (1-2.4 km) percentage varies little with time (figure 4.4c), even though the actual magnitude of IWV in the cloud layer decreases. Therefore, at the end of PHASE-2, there is less water vapor in the BL, less water vapor in the cloud layer, and more water vapor in the free troposphere compared to that at the start of PHASE-1.

B. SENSITIVITY SIMULATIONS

Figures 4.6 and 4.7 are similar to figure 4.4, but now include comparisons between the vertical IWV distribution for the CL simulation and the SST (+/-2KCL) and aerosol (PO) sensitivity simulations, respectively. The first thing to note is that in all of the sensitivity simulations, the total IWV decreases throughout the entire depth of the atmosphere between PHASE-1 and PHASE-2 as it did in the CL simulation (figures 4.5, 4.6a, 4.7a).

Increasing SSTs are associated with a greater magnitude of IWV throughout the depth of the atmosphere (figure 4.5, 4.6a), which is in keeping with the Clausius-Clapeyron equation. This increase is on the order of 14-17% between the -2KCL and +2KCL simulations (figure 4.6a) in both phases, and is due to increases in the actual magnitude of IWV in the sub-cloud and free troposphere layers (figure 4.5). The IWV in the cloud layer (figure 4.5) is found to decrease with increasing SST, the reasons for which will be discussed below. The partitioning of IWV in the atmosphere (i.e. the percentage) is also dependent on the SST. With increasing SST, the percentage contribution of the IWV in the sub-cloud layer (0-1km) (figure 4.6b) decreases while

the trends reverse in the free troposphere, in that an increase in the percentage contribution is evident (figure 4.6d). Although the percentage contribution of the IWV to the total IWV in the sub-cloud layer is less over warmer SSTs, there is more actual IWV mass in the sub-cloud layer in both phases and similarly in the free troposphere layer (figure 4.5). Therefore, with increasing SSTs, the actual magnitude of the IWV in the sub-cloud layer and free troposphere (cloud layer) is greater (smaller), however, the percentage contribution to the total IWV varies, with a decrease in the sub-cloud layer, an increase in the free troposphere and a mixed response in the cloud layer with increasing SST. Therefore, warmer SSTs result in greater moisture contents in the atmosphere, with proportionally larger amounts in the free troposphere.

The reduced percentage of IWV in the sub-cloud layer and increasing percentage in the free troposphere with increasing SST suggests that a vertical redistribution of IWV is occurring, either through changes in advection, large-scale lift, or local cloud processes that are fluxing moisture upwards from the sea surface source to the free troposphere. The average IWV in the cloud layer is less with increasing SSTs (figure 4.5). This suggests that the local cloud processes are at least in part responsible for the vertical redistribution of moisture from the sea surface source to the free troposphere through the cloud layer. For example, over warmer SSTs, more congestus clouds were present (figure 3.16). These clouds will assist in fluxing water vapor to the free troposphere. Subsequent sections of this chapter will investigate this cloud scale vertical redistribution compared with other sources such as ETC large-scale advection.

Unlike the simulations with varying SST, changing the aerosol loading has little impact on IWV (figure 4.7a, 4.5). The greatest differences are in the cloud layer (1-2.4 km ASL) where the percent differences in the contributions to the total IWV are similar to those for the SST simulations (figure 4.7c). Chapter 3 showed PCF cumulus cloud updraft and condensate

formation to be sensitive to cloud nucleating aerosol and as such can redistribute sub-cloud BL moisture towards the top of the BL in the cloud layer. However, unlike SST, aerosols have a limited impact on the redistribution of water vapor from the surface to the free troposphere.

4.3 VERTICAL WATER VAPOR MASS FLUX

A. THE CL SIMULATION

The magnitude of vertical water vapor mass flux at any point in space and time will depend on both the vertical velocity and the available water vapor mass. Water vapor mass can be fluxed vertically by rising or sinking motion within both cloudy and cloud-free air. Here we will compare the cumulative upward and downward water vapor mass flux occurring at each altitude of the PCF region.

Figure 4.8 shows vertical profiles of the temporally-averaged upward ($w > 0$ m s^{-1}), downward ($w < 0$ m s^{-1}), and net (all upward and downward motion) water vapor mass flux horizontally integrated over Grid 3 for both phases. The WVMF was first calculated at each model level and then horizontally integrated across all of Grid 3 at each model level:

$$WVMF = \int w q_v \rho_a dA \tag{4.2}$$

where w (m s^{-1}) is the vertical velocity and the other terms have been defined previously. Horizontally integrating represents the cumulative WVMF of the PCF region for the upward and downward motions. Each WVMF was then averaged temporally over the 8 hours of each phase.

In both phases, both the upward and downward vertical WVMF is largest within the BL, and maximizes near 0.5-1 km ASL before it decreases with height (figure 4.8). This occurs as a result of the water vapor content being significantly larger in the BL than higher up. Equivalent vertical velocities at lower altitudes will therefore vertically flux more water vapor within the BL than at higher altitudes. The average PCF upward WVMF in figure 4.8(a,d) resembles the

average vertical velocity profiles of the in-cloud updrafts (figure 3.12) shown in Chapter 3. Here, the peak upward WVMF is slightly below the average updraft peak near 2 km of the large number of PCF cumulus clouds due to being constrained to a slightly lower altitude by the BL water vapor content. Upward WVMF decreases above the BL in part due to the limited number of updrafts at this level (see cloud fraction in figure 3.7), and in part due to the reduced water vapor mass in this region. Hence for upward WVMF, this cumulative flux is primarily determined by the magnitude and number of cloudy updrafts, although any rising motion in the clear air columns is also included in these cumulative totals. Downward WVMF is a function of the local cloud circulations and downdrafts, which are inherently linked to the cloud dynamics and microphysics, and larger scale ETC subsidence and radiation. As with the upward WVMF, the peak downward WVMF is in the BL where water vapor is more readily available for fluxing (figure 4.8b,e). Evaporation of precipitation within downdrafts will also contribute to this signal.

The net average WVMF is positive throughout the vertical profile in both phases (figure 4.8c,f), although is close to neutral in the free troposphere in PHASE-2. Therefore, more water vapor is lifted from the surface to the free troposphere through the action of these PCF clouds than is transported downward into the BL. There is a hint of the double-peak structure in the net WVMF profiles in PHASE-1 in keeping with that observed in Chapter 3. The average peak upward WVMF is less in PHASE-2 than in PHASE-1. This is due to the fact that the BL cloud fraction is much less in PHASE-2 (figure 3.7), and also that the moisture content of the BL is less in this phase. In the deeper PCF clouds of PHASE-2, the decrease in average cloud updraft (figure 3.12) will also be responsible for the decreased WVMF in the deeper clouds (figure 4.8f), although this is partially compensated by the increasing water vapor content of the free troposphere in PHASE-2. The decrease in average downward WVMF is due to the reduced

number of downdrafts in association with the development of fewer BL clouds. This results in the peak average net vertical WVMF being on the order of 2-3 times greater in PHASE-1 than in PHASE-2. Overall, both the PCF cumulus and congestus clouds of PHASE-1 have a greater net upward WVMF than in PHASE-2.

B. SENSITIVITY SIMULATIONS

Here we will examine the differences in the average upward and downward WVMF due to varying the SST and the concentration of available cloud nucleating aerosol. These environmental factors were shown to alter the average PCF cloud updraft speed, cloud fraction, and for SST experiments, the vertical water vapor mass profile. Each of these variables will impact the magnitude of the WVMF. Figures 4.9 and 4.10 are similar to 4.8 but now examine the upward, downward, and net WVMF for the +/-2KCL (figure 4.9) and the PO (figure 4.10) simulations.

With increasing SSTs, the average upward, downward, and net WVMF is greater at all altitudes and in both phases (figure 4.9). The increase in average upward WVMF will be due to in part to the increases in the atmospheric IWV (figure 4.6), the increased cloud fraction over warmer SSTs (figure 3.16), and the stronger updrafts that extend, on average, to greater depths of the free troposphere (figure 3.18). These factors all combine to produce a greater upward flux of water vapor over warmer SSTs throughout the BL and the free troposphere. These increases are on the order of 200-400% between the lowest and warmest SST sensitivity experiments (figure 4.9c,f,i,l). The differences between the SST sensitivity experiments are less in PHASE-2 than in PHASE-1.

Increasing the available CCN increases the average updraft speed due to changes in latent heating associated with cloud water formation through suppression of the warm rain process

(section 3.4). As the ambient water vapor is initially unchanged between these simulations given that SST is held constant, the primary differences in the cumulative WVMF will be due to aerosol-induced differences in the water vapor profile due to microphysical processes (figures 3.25, 3.26), vertical velocity (figure 3.27), and the cloud fraction (figure 3.23). The upward and downward WVMF are increasing in association with the stronger, more frequent polluted PCF clouds (figure 4.10), although this increase is very small compared with those seen in association with changes to SST. Differences are non-existent in the free troposphere, especially above 4 km ASL, as the increasing number of PCF congestus clouds in the PO simulation is not sufficient to increase the cumulative WVMF. The greatest differences between the CL and PO simulations in both PHASE-1 and PHASE-2 are in the cloud layer (1-2.4 km ASL) (figure 4.10c,f,i,l), similar to the trends in IWV found in figure 4.7c. Furthermore, the differences are larger in PHASE-2. In this phase, the impacts of the drier BL on the aerosol-altered drop size distributions become more apparent. This is discussed in more detail in the next section.

4.4 DETRAINMENT AND EVAPORATION OF CONDENSATE

A. THE CL SIMULATION

PCF cumulus clouds impact the vertical redistribution of water vapor through their formation of cloud droplets through condensation, and their vertical transport and subsequent evaporation of those droplets and other hydrometeors (figure 4.1). If these clouds extend above the BL, they can assist in the transport of water vapor from the BL to the free troposphere through detrainment and evaporation. Evaporation of precipitation below cloud base could counterbalance this process and return water vapor mass to the BL. The balance between condensation and evaporation is important for the formation of surface precipitation, which is a

sink of water vapor from the PCF region. The evaporation-condensation processes within the PCF region will now be examined.

Figure 4.11 shows vertical profiles of the temporally-averaged horizontally integrated rate of condensate mass formation/loss per vertical meter (kg m^{-1} s^{-1}) that is due to all hydrometeor evaporation and sublimation ($r_c < 0$), nucleation and condensation ($r_c > 0$), and the net of these respective processes:

$$COND = \int r_C \rho_a dA \tag{4.3}$$

where r_c (kg_{cond} kg_{air}^{-1} s^{-1}) is the rate of each respective condensate mass formation/loss and the other terms have been defined previously. r_c is outputted from the model at 5-minute intervals and converted to rates in terms of seconds. COND was temporally-averaged over the 8 hours of each phase to create the vertical profiles shown in figure 4.11. Nucleation and vapor depositional growth of cloud droplets and ice are shown as a positive process ($r_c > 0$; COND > 0) while evaporation of cloud droplets and sublimation of ice are shown as a negative process ($r_c < 0$; COND < 0).

These vertical profiles represent the exchange between water vapor mass and cloud condensate, the net of which will give us some sense of the redistribution of water vapor in the vertical due to cloud microphysical processes. Condensation and evaporation maximize between 1-2 km ASL in association with the presence of the PCF cumulus clouds while mixed phase processes are more important at higher altitudes in PCF congestus clouds (figure 4.11a,b,d,e). Here, we find that the cumulative nucleation and condensation rates in the PCF grid domain are greater than the cumulative evaporation and sublimation counterparts in both PHASE-1 and PHASE-2 (figure 4.11c,f), except below cloud base where precipitation evaporation is most important. This highlights a net loss of water vapor from the atmosphere to condensate formation,

with a relatively small return to the BL through precipitation evaporation. The average net COND profiles in both PHASE-1 and PHASE-2 are similar in magnitude and structure (figure 4.11c,f), but the greatest differences exist near the lower free troposphere above the BL due to the greater number of PCF cumulus clouds and strong PCF congestus clouds in PHASE-1.

B. SENSITIVITY SIMULATIONS

Figures 4.12 and 4.13 are similar to Figure 4.11, but now include average profiles from the +/-2KCL (figure 4.12) and the PO simulation (figure 4.13) and their difference from the CL average profile for both phases. Warmer SSTs result, on average, in less cumulative cloud water condensing and evaporating in the PCF cumulus clouds, but greater cumulative rates (including ice) in the deeper PCF congestus clouds (figure 4.12). These trends remain in the net (figure 4.12c,f,i,l) and match those in Chapter 3, where increasing SSTs promoted more vigorous, deeper convection and the associated conversion of cloud water to ice and rain water, thereby reducing cloud water nucleation and vapor depositional growth throughout the depth of the cumulus clouds. Fewer cumulus clouds and greater numbers of stronger PCF congestus clouds were found with increasing SST, resulting in the increasing trends evident above 3 km ASL in figure 4.12 (b,e,h,k). Cumulative rates of evaporation/sublimation (figure 4.12a,d,g,j) are also a function of the number of clouds and decrease with decreasing SSTs. Additionally, we see enhanced precipitation evaporation below cloud base with increasing SSTs (figure 4.12a,d,g,j) from the increase in the number of precipitating clouds and the increase in average precipitation mass.

In the more polluted PCF clouds, the trends in the cumulative nucleation/condensation versus evaporation/sublimation are much weaker than those with SST (figure 4.13). In Chapter 3, we found that aerosol-induced suppression of the warm rain process resulted in a greater cloud

droplet cumulative surface area and the production of more cloud condensate. This signal is seen in the cumulative here (figure 4.13b,e,h,k). However, a corresponding increase in the cumulative evaporation/sublimation is also found with increased aerosol loading, resulting in the net differences (figure 4.13c,f,i,l) to be relatively small.

4.5 WATER VAPOR BUDGET OF GRID 3

Figure 4.1 suggests the main pathways for water vapor exchange and transport in the PCF region. As discussed in the previous sections of this chapter, this includes local cloud processes including vertical WVMF and the transformations between water vapor and cloud condensate. Here we will complete the water vapor budget of the PCF region by examining the other relevant processes.

A. WATER VAPOR BUDGET EQUATION

The PCF regional water vapor budget is calculated with respect to Grid 3. The water vapor budget will be calculated using the following equation:

$$\frac{\partial IWV}{\partial t} = F_{HZ} + F_{SFC} - \frac{\partial C}{\partial t} - \frac{\partial P}{\partial t} \tag{4.4}$$

where $\frac{\partial IWV}{\partial t}$ is the change with time in the grid domain water vapor storage, F_{HZ} is the horizontal flux convergence of the vertically integrated water vapor and condensate mass, F_{SFC} is the flux of water vapor into the grid domain from surface evaporation, and $\frac{\partial C}{\partial t}$ and $\frac{\partial P}{\partial t}$ are the rates of the production/loss of condensate (C) or the production of surface precipitation (P) within the grid domain.

IWV was calculated according to equation (4.1), divided by the grid area, then differenced over the 5-minute model output to calculate the water vapor storage term, $\frac{\partial IWV}{\partial t}$ (kg

m^{-2} s^{-1}). $\frac{\partial IWV}{\partial t}$, $F_{SFC,}$, $\frac{\partial C}{\partial t}$, and $\frac{\partial P}{\partial t}$ were all calculated directly from the model simulation output (the latter three terms described below) while F_{HZ} (kg m^{-2} s^{-1}) was calculated as a residual of the other four terms using equation (4.4).

The flux of water vapor into the grid domain from the surface, F_{SFC} (kg m^{-2} s^{-1}), was calculated by horizontally integrating the latent heat flux (*LHF*; W m^{-2}) output from the model then dividing by the grid domain area (A; m^2) and the latent heat of vaporization (l_v; 2.5 x 10^6 J kg^{-1}) in the following expression:

$$F_{SFC} = \frac{1}{l_v A} \int LHF dA \tag{4.5}$$

Flux into the grid domain from the surface was deemed to be positive.

The rate of the production of condensate, $\frac{\partial C}{\partial t}$ (kg m^{-2} s^{-1}), was calculated by vertically and horizontally integrating the mass of condensate in the grid domain using the total condensate mixing ratio at a single time step and dividing by the grid domain area:

$$C = \frac{1}{A} \iint q_c \rho_a dz dA \tag{4.6}$$

Then, the change in C over the 5-minute model output was calculated and converted to per second. A positive $\frac{\partial C}{\partial t}$ indicates that more condensate was present in the grid domain after 5-minutes while a negative $\frac{\partial C}{\partial t}$ indicates less condensate was present in the grid domain after 5-minutes.

The model output includes the grid domain accumulated precipitation (P; mm), which when divided by the grid area and differenced over the 5-minute model output produces the final

term on the right hand side of equation (4.4) ($\frac{\partial P}{\partial t}$) in mm s^{-1}, which is equivalent to kg m^{-2} s^{-1}. $\frac{\partial P}{\partial t}$ can only be zero or greater than zero.

Figure 4.14 shows a schematic of the balance between each term in the water vapor budget equation (4.4) in the PCF grid domain (i.e. Grid 3). $\frac{\partial IWV}{\partial t}$ and $\frac{\partial C}{\partial t}$ represent the change in the water vapor storage (IWV + C) within the grid domain as water vapor is fluxed in and out of the grid domain due to F_{HZ}, F_{SFC}, and precipitation. Figure 4.15 examines the time series (kg m^{-2} s^{-1}) of (a) $\frac{\partial IWV}{\partial t}$, (b) $\frac{\partial C}{\partial t}$, (c) $\frac{\partial P}{\partial t}$, (d) F_{SFC}, and (e) F_{HZ}, over PHASE-1 and PHASE-2. Assuming the rates in figure 4.15 are constant over the 5-minute model output, we can estimate the total water vapor mass (kg) contributed by each term in equation (4.4) for PHASE-1 and PHASE-2 for Grid 3. This is presented in figure 4.16, and allows for a comparison of the bulk PCF processes in figures 4.14 and 4.15 and their variations with phase, SST, and aerosol. In figure 4.16, the signs associated with each term in equation (4.4) are included. This allows for the sources of IWV to be shown as positive estimates and sinks as negative estimates. For example, if the amount of condensate in the domain were decreasing with time (i.e. $\frac{\partial C}{\partial t} < 0$), the estimate would be shown as a positive (i.e. a source) value in figure 4.16 as the condensate term is represented as $-\frac{\partial C}{\partial t}$ in equation (4.4).

B. CL SIMULATION

In the CL simulation, the local time rate of change in the IWV ($\frac{\partial IWV}{\partial t}$), or the water vapor storage, is negative (figure 4.15a) for most of the time period, which reflects the decrease

in IWV per phase found in figure 4.4a. This loss occurs at a greater rate in PHASE-1 than PHASE-2.

The smallest contributor to the water vapor budget in the PCF region is the change in total condensate. The condensate term is primarily negative in PHASE-1 (figure 4.15b), indicating that less total condensate is forming with time in the PCF grid domain. In PHASE-2, this term is close to zero, which indicates very little change in condensate formation. These are consistent with the decreasing cloud fractions with time as found in Chapter 3, such as from PHASE-1 to PHASE-2. As this term is negative in PHASE-1 (and close to zero in PHASE-2) it implies that the reduced condensate formation is a source of water vapor (i.e. $-\frac{\partial C}{\partial t} > 0$). However, as stated above, this term is very small compared with the other terms, and in essence is negligible.

The net rate of change in surface precipitation mass ($\frac{\partial P}{\partial t}$), a sink to water vapor, is an order of magnitude larger than the condensate term (figure 4.15c). The precipitation term is larger in PHASE-1 than PHASE-2. In Section 3.2C, it was demonstrated that the average surface precipitation mass of an individual PCF cloud is less in PHASE-2 than in PHASE-1 for the CL simulation. These reduced precipitation rates combined with the fewer BL clouds forming during PHASE-2 resulted in the reduced grid domain average precipitation rate during PHASE-2 (figure 3.10). Overall, the precipitation term is an important control on the IWV in the PCF region due to its sheer magnitude.

F_{SFC} and F_{HZ} are comparable sources/sinks of water vapor mass in the PCF region in terms of their magnitudes. In the CL simulation, a slightly decreasing source of water vapor from sea surface evaporation occurs with time (figure 4.15d), while the water vapor flux convergence

is primarily negative throughout both phases of the CL simulation (figure 4.15e). A negative water vapor flux convergence indicates that more water vapor is being advected out of the domain than is being converged into it. The primary control of the grid domain F_{HZ} is the zonal advection, as the flow in the PCF region is primarily from the west.

As F_{HZ} was calculated as a residual from the other four terms in equation 4.4, caution has to be taken in interpreting this term. Errors exist inherently due to using a computer model and it's representation of physical processes, and calculating F_{HZ} from the other terms may cumulatively compound these errors in this term. This cumulative error may be contributing to the rapid variations with time in this term and hence consideration of the broader trend is needed.

Overall in the CL simulation (figure 4.16), the dominant control of the water vapor budget in the PCF region is the precipitation term, which tends to be at least twice the size of any of the other contributing terms. Water vapor in the PCF region is thus depleted primarily by precipitation. Flux divergence and condensate formation are also both found to decrease the water vapor content of the atmosphere, with the flux divergence being the larger contributor. These negative contributions are offset by surface evaporation contributions that are similar in magnitude to the loss due to advection of water vapor from the grid domain. The greatest changes between PHASE-1 and PHASE-2 are associated with the precipitation term, which is reduced in PHASE-2. As the other terms remain relatively constant, the loss in water vapor storage in PHASE-2 is reduced.

C. SENSITIVITY SIMULATIONS

All of the sensitivity simulations demonstrate greater differences in the water vapor budget terms during PHASE-1 than in PHASE-2. In fact, most of the terms are relatively constant in PHASE-2.

The water vapor loss due to precipitation is greater in magnitude for the higher SST cases, that is a greater proportion of water vapor is lost from the atmosphere through precipitation in the warmer SST case than in any of the other sensitivity tests. This is in keeping with the results shown in Chapter 3, which showed that the number of precipitating clouds increases with increasing SST, and that their precipitation rates increase as well (figure 3.21).

F_{SFC} is also greater with increasing SSTs following the Clausius-Clapeyron equation (figure 4.15d). However, this source of water vapor remains less than half of the sink due to precipitation. The differences are less pronounced in PHASE-2, which is at a further distance from the cold front. These reduced differences in F_{SFC} with SST in PHASE-2 are due in part to the reduced near surface winds and in part to the increases in the atmospheric air temperature with the weakening of the cold front passage.

Over the warmest SSTs, the moisture flux convergence, F_{HZ}, is primarily positive in PHASE-1 before becoming negative in PHASE-2 (figure 4.15e). Therefore in the highest SST case, water vapor converges into the PCF region, whereas in the CL and low SST cases water vapor is still lost from the PCF region through the grid domain boundaries.

The integrated impacts of these terms in each phase are shown in figure 4.16. It is clear from this figure that the changes are greatest in PHASE-1 in association with the activity of the PCF region. Also, it is clear from this figure that the storage of water vapor in the atmosphere decreases in both phases. Thus, there is an overall drying throughout the atmosphere, and that this is greatest in PHASE-1. Furthermore, the dominance of the precipitation term is clearly evident from this figure. The gains of atmospheric water vapor through surface fluxes are somewhat similar to the loss through water vapor flux divergence, and the condensate contributions are minor. Thus, the variations in water vapor storage in the PCF region are

primarily dominated by the precipitation rates, which increase with increasing SST. It is interesting to note that a weak vapor flux convergence occurs in the highest SST case. It is hypothesized that this occurs in association with the fact that the precipitation loss is so large in this case, that more water vapor is being transported into the region from the west than is being lost from the downwind boundary. This is more prevalent in PHASE-1, wherein during PHASE-2 the lesser surface precipitation-surface evaporation imbalance results in divergence of water vapor from the PCF region, although at lesser rates than that of the lower SSTs.

While increasing the concentration of cloud nucleating aerosols was found to increase the amount of cloud condensate (figure 3.24), the aerosol-induced change to the surface precipitation (figure 4.15c) through suppression of the warm rain process remains the primary term in the water vapor budget. The reduced loss through precipitation in the polluted case results in slightly more water vapor being stored in the atmosphere in the polluted case during PHASE-1. Overall, the aerosol-induced differences in the terms in equation (4.4) are small.

4.6 DISCUSSION

In this study, we have simulated a wintertime ETC at high temporal and spatial resolutions that allowed us to examine the water vapor budget of the PCF region. A suite of simulations that varied SST or available cloud nucleating aerosol allowed further investigation into the PCF cloud processing of water vapor combined with considerations of the sea surface source of water vapor and moisture advection. Recent studies (B10; B11) have highlighted the importance of PCF clouds in lofting water vapor to the free troposphere from the BL and the subsequent impacts that this has on moisture supply to the WCB. The previous chapter analyzed the cloud microphysical and dynamical structure of PCF clouds, which aided the analysis of this chapter on the cumulative PCF regional processing of water vapor overall.

Figure 4.1 highlighted the main pathways that PCF cumulus clouds impact the local and regional water vapor budgets, which are inherently tied to the external forcings such as moisture advection into the PCF region controlled by the ETC dynamics and sea surface evaporation. Vertical upward flux of water vapor mass and condensate mass occurs in these PCF clouds, and is largest within the BL where the greatest concentration of water vapor overlaps with the largest updrafts in PCF clouds. However, the return of water vapor into the boundary layer by local cloud circulations and large-scale subsiding motion is found to offset this lofting, at least in part. Never the less, the PCF region does produce a net upward lofting of water vapor. Detrainment and evaporation of lofted condensate is found to be a relatively small factor in the overall water vapor budget but does serve as to return water vapor from the atmosphere.

The availability of moisture to be transported eastward and poleward from the PCF region by the greater ETC circulation is reliant on the cloud-precipitation processes combined with the interaction with large-scale advection and the surface evaporation source. PCF clouds move water vapor from the BL to the free troposphere within the PCF region, but also remove water vapor from the system through precipitation. The loss of water vapor from the atmosphere due to precipitation processes in the PCF region is found to be by far the dominant term in the water vapor budget equation. It is this PCF cloud process that robs the atmosphere of its water vapor in this region. The loss of water vapor is offset by evaporation from the sea surface, but it is insufficient to offset the loss due to precipitation. It should be noted here that should interactive SSTs been utilized that the surface water vapor flux would have been reduced due to a cooling of the SST following precipitation. Furthermore, the loss of water vapor through the precipitation process reduces the amount of water vapor that is transported out of the PCF domain. This is particularly evident in the highest SST case where the precipitation loss is so

high that, in spite of enhanced surface fluxes, the water vapor flux convergence is slightly positive, that is less water vapor leaves the PCF region than is advected into it. Finally, the impacts of aerosol on the PCF water vapor budget were much smaller than those for SST, and occurred primarily through their impacts on precipitation and condensate loading.

Previous work (B10; B11) that compared the importance of lofting of water vapor by PCF clouds to the WCB were unable to consider the complexity of clouds that were not resolved in their larger scale models. For example, the resultant downward flux of water vapor due to local induced cloud circulations and the complex precipitation processes. Here, the dominant role of the precipitation process as a water vapor sink, and the impact of environmental conditions on this precipitation process have proved critical. Unless GCMs are able to represent such processes, the water vapor sources and sinks in the PCF region will not be properly represented, and hence the subsequent amounts of water vapor transported in the mid- and upper-troposphere will not be properly simulated. This has significant impacts for the poleward transport of water vapor by ETC systems, as well as the latitudinal variation in their precipitation production. In the next chapter will examine how the moisture that is lofted in the PCF region can be transported within the overall ETC motions, including cold frontal ventilation and lofting into the upper level westerlies. The importance of ETC intensity and strength will be shown to be important, especially if linked to increased SST as shown here.

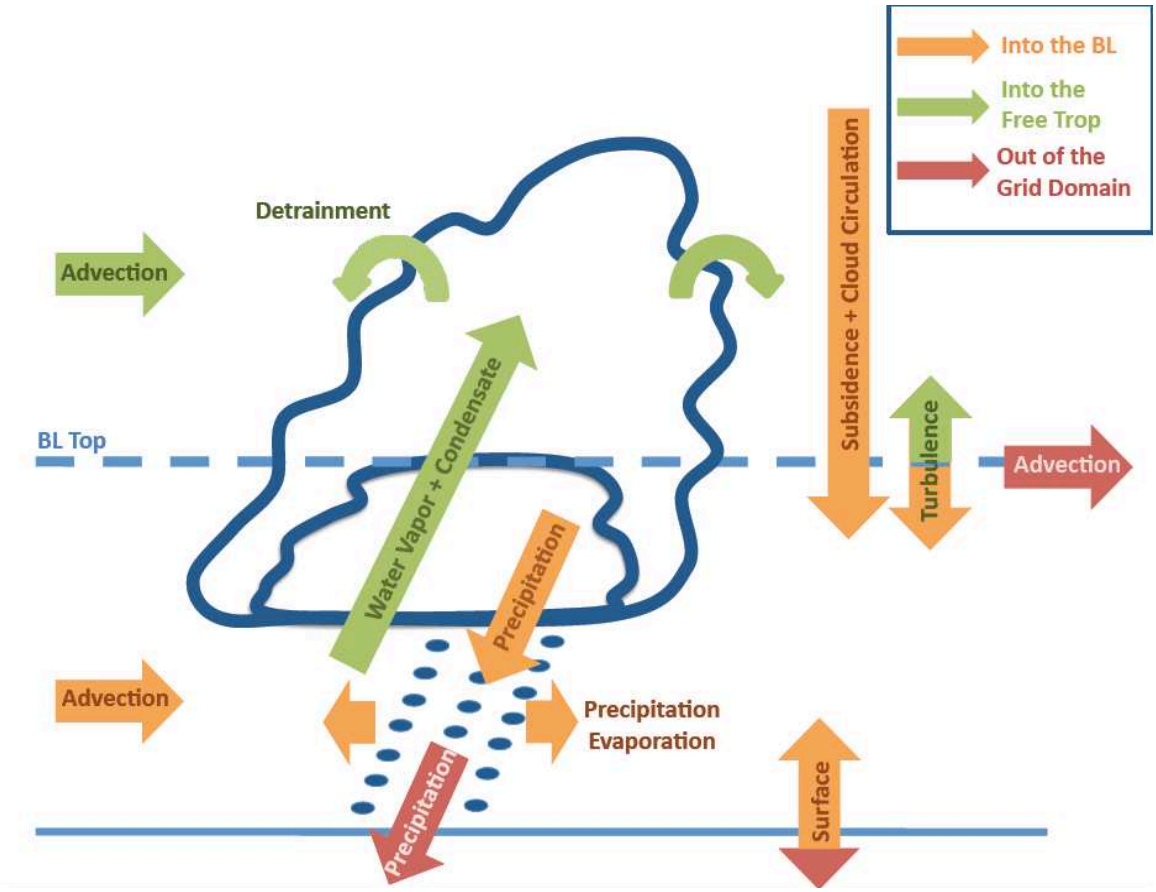

Figure 4.1: Schematic of the processes in the post-cold frontal (PCF) region that flux water vapor mass in/out of the boundary layer (BL). Colored arrows represent these processes including water vapor fluxes into the boundary layer (orange), out of the BL to the free troposphere (green), and to the surface or out of the region (red). PCF clouds that extend either to the BL inversion or into the free troposphere are drawn as examples.

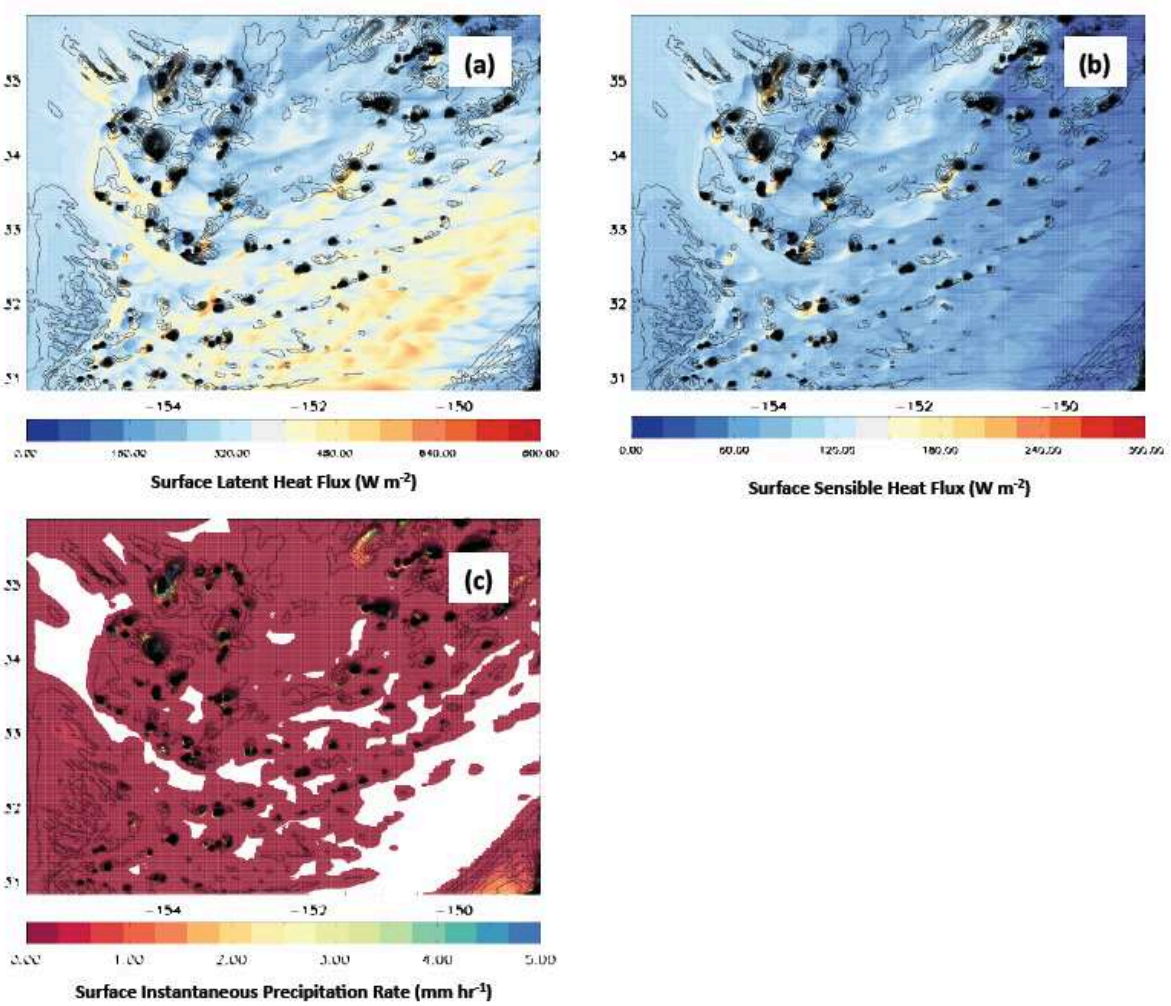

Figure 4.2: Plan view (Grid 3) of (a) surface latent heat flux (shaded; W m^{-2}), (b) surface sensible heat flux (shaded; W m^{-2}), and (c) surface instantaneous precipitation rate (shaded; mm hr^{-1}) overlaid with vertical integrated condensate (0.5 mm; contoured) at 18Z 13 January 2010 of the CL simulation.

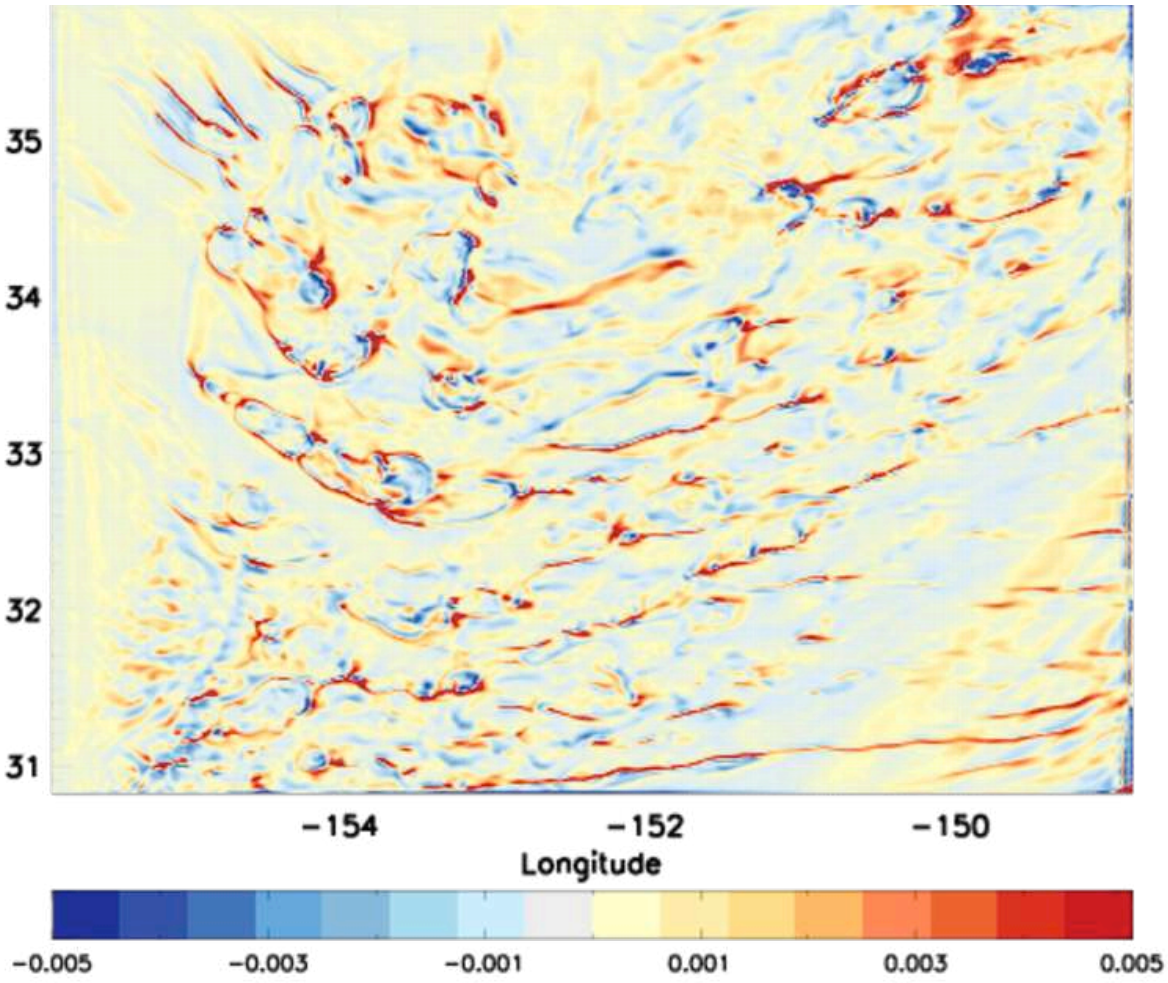

Figure 4.3: Plan view (Grid 3) of the vertical water vapor mass flux (kg m^{-2} s^{-1}) at 1 km ASL at 18Z 13 January 2010 of the CL simulation.

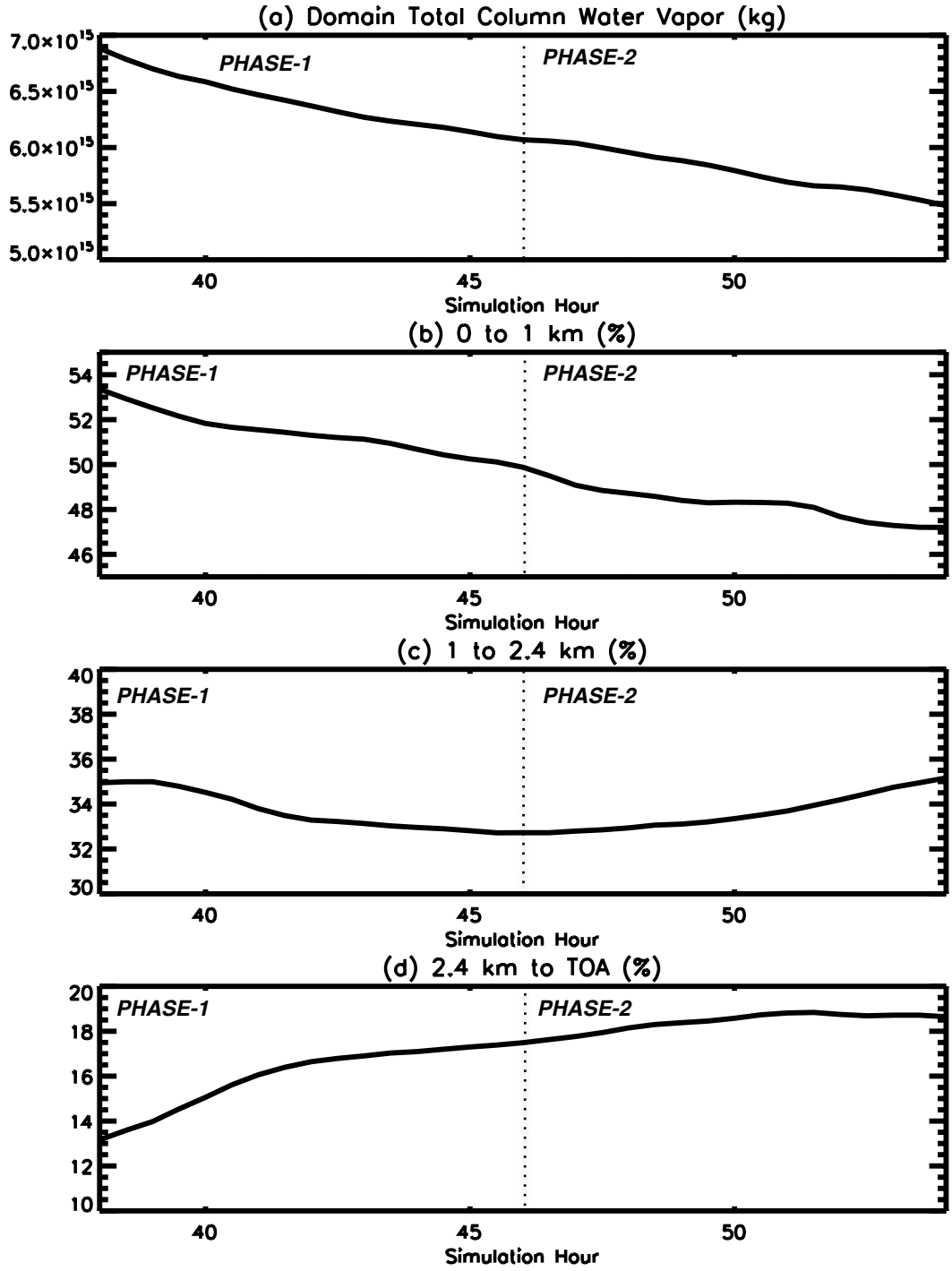

Figure 4.4: Time series of the integrated water vapor mass (IWV) (kg) for Grid 3 for the CL simulation for (a) entire atmosphere, and (b) from 0 to 1 km, (c) from 1 to 2.4 km, and (d) from 2.4 km to the top of atmosphere (TOA). Figures (b) through (d) are represented as percentages of the total IWV shown in (a). The vertical dashed line at 46 simulation hours discriminates between PHASE-1 and PHASE-2.

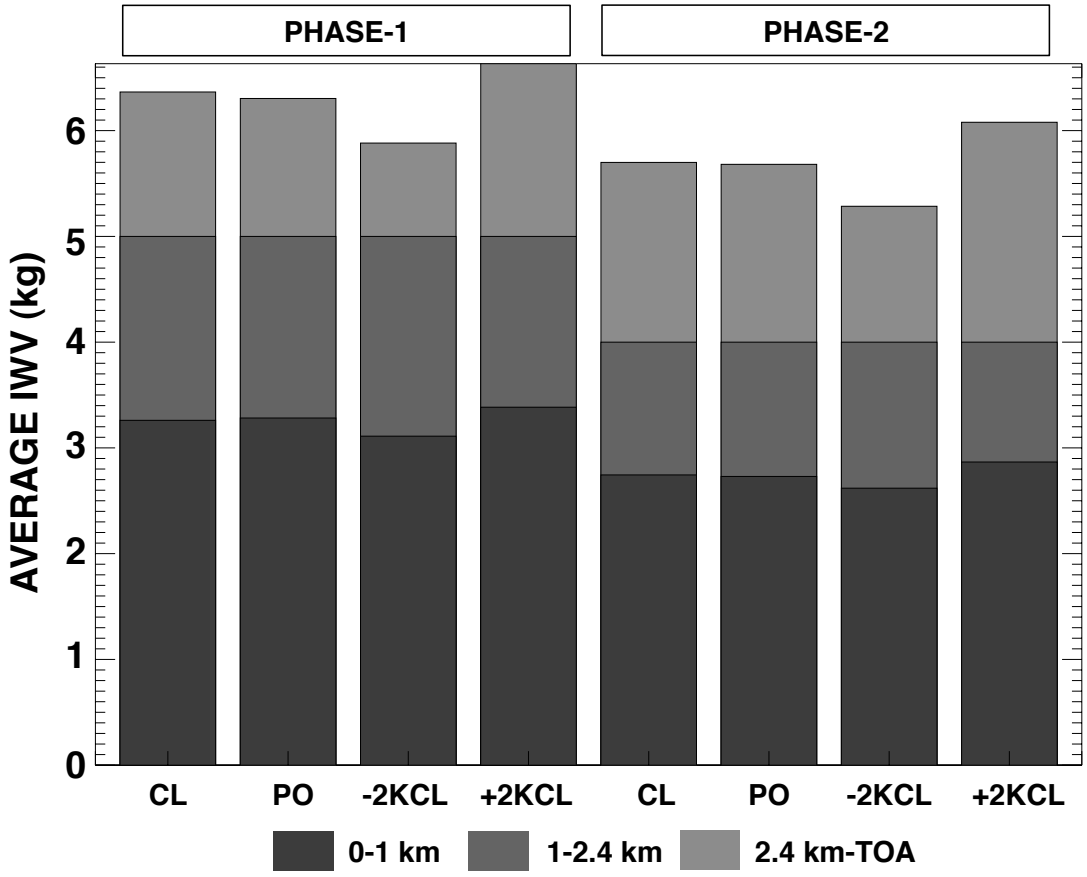

Figure 4.5: Average IWV (kg) in PHASE-1 and PHASE-2 for the CL, PO, -2KCL, and +2KCL simulations. The IWV is partitioned into three layers: 0-1 km, 1-2.4 km, and 2.4 km – TOA.

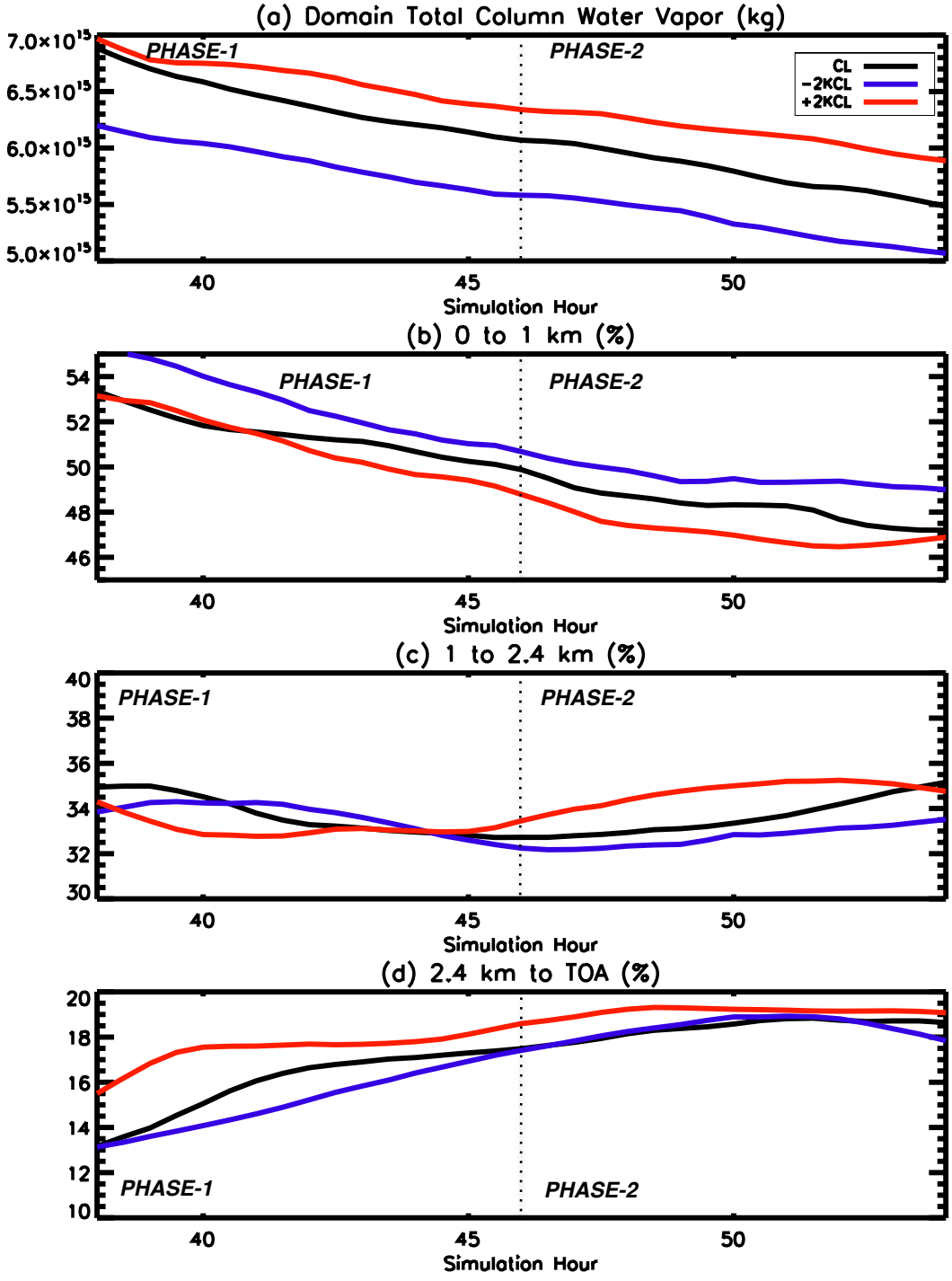

Figure 4.6: As for figure 4.4, but now for the SST sensitivity experiments.

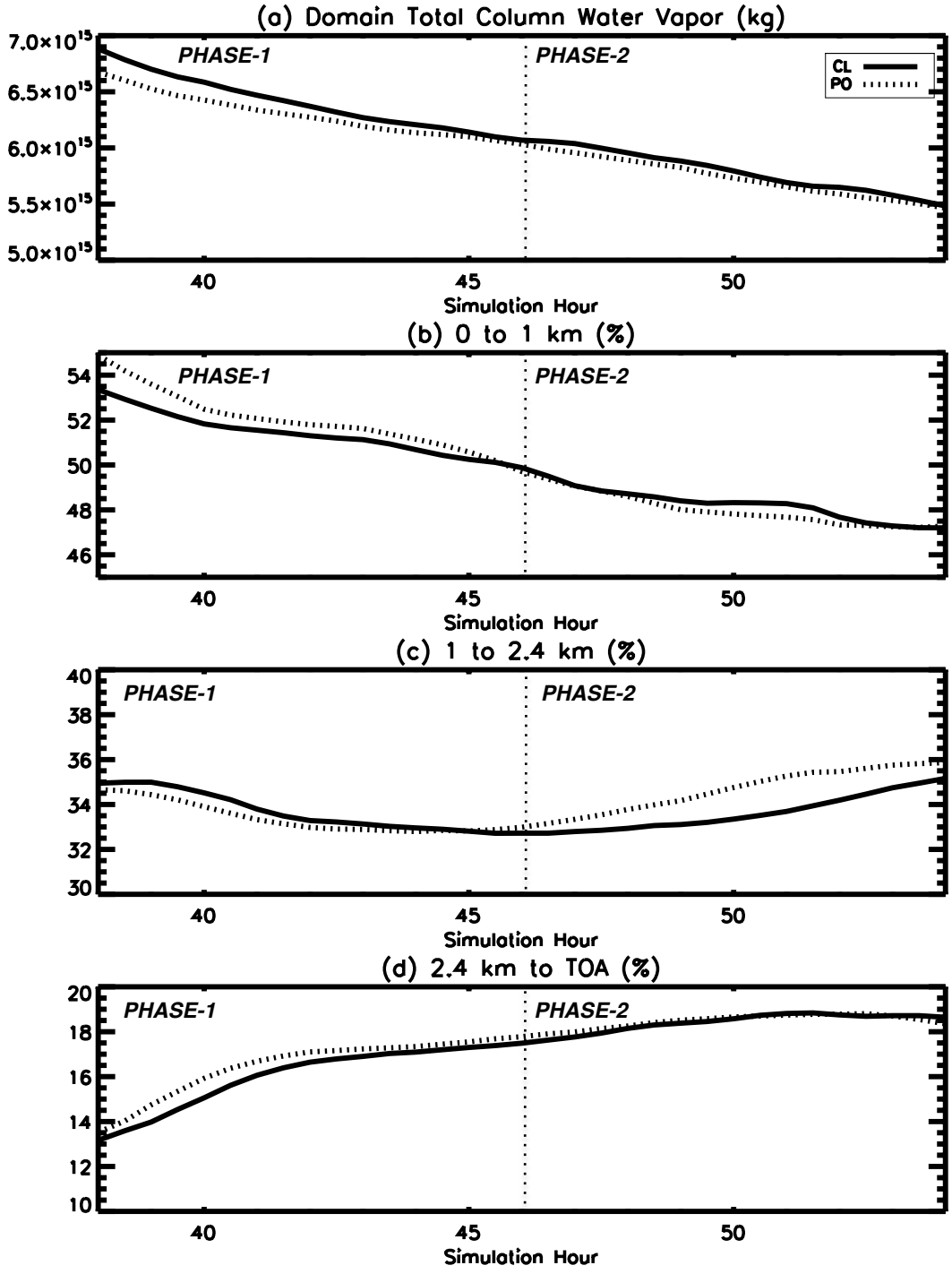

Figure 4.7: As for figure 4.4, but now for the aerosol sensitivity experiment.

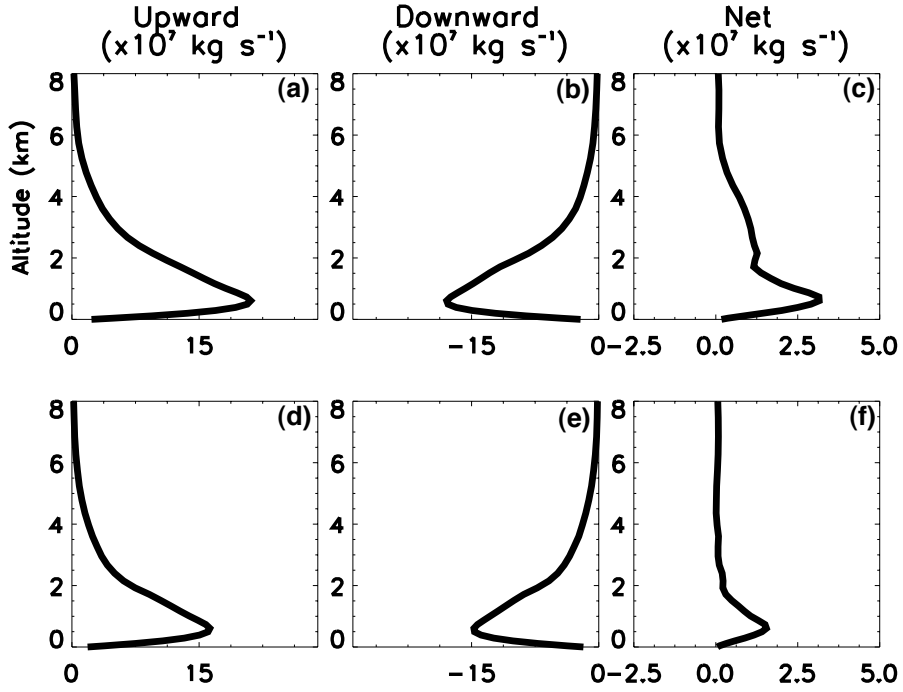

Figure 4.8: Vertical profiles of the temporally-averaged, horizontally integrated vertical water vapor mass flux (x10^7 kg s^{-1}) for all motions (in and outside of cloud) (a,d) upward (w > 0 m s^{-1}), (b,e) downward (w < 0 m s^{-1}), and (c,f) net, for PHASE-1 (a-c) and (d-f) PHASE-2. Note that the scale in panels (c) and (f) covers a smaller range than in the other panels.

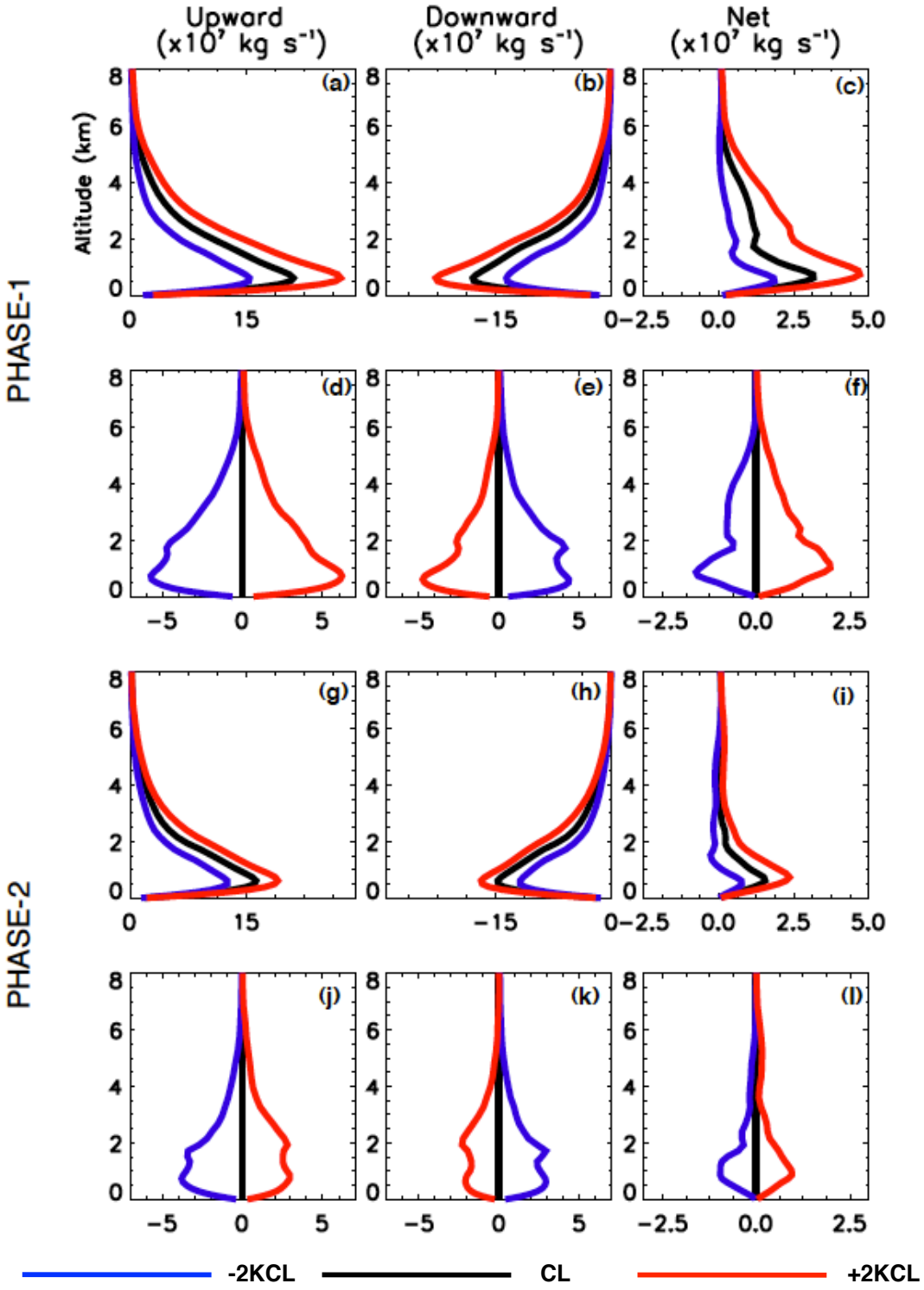

Figure 4.9: As for figure 4.8, but for the SST sensitivity experiments, including the differences from the average CL profile (d-f, j-l) for PHASE-1 (a-f) and PHASE-2 (g-l).

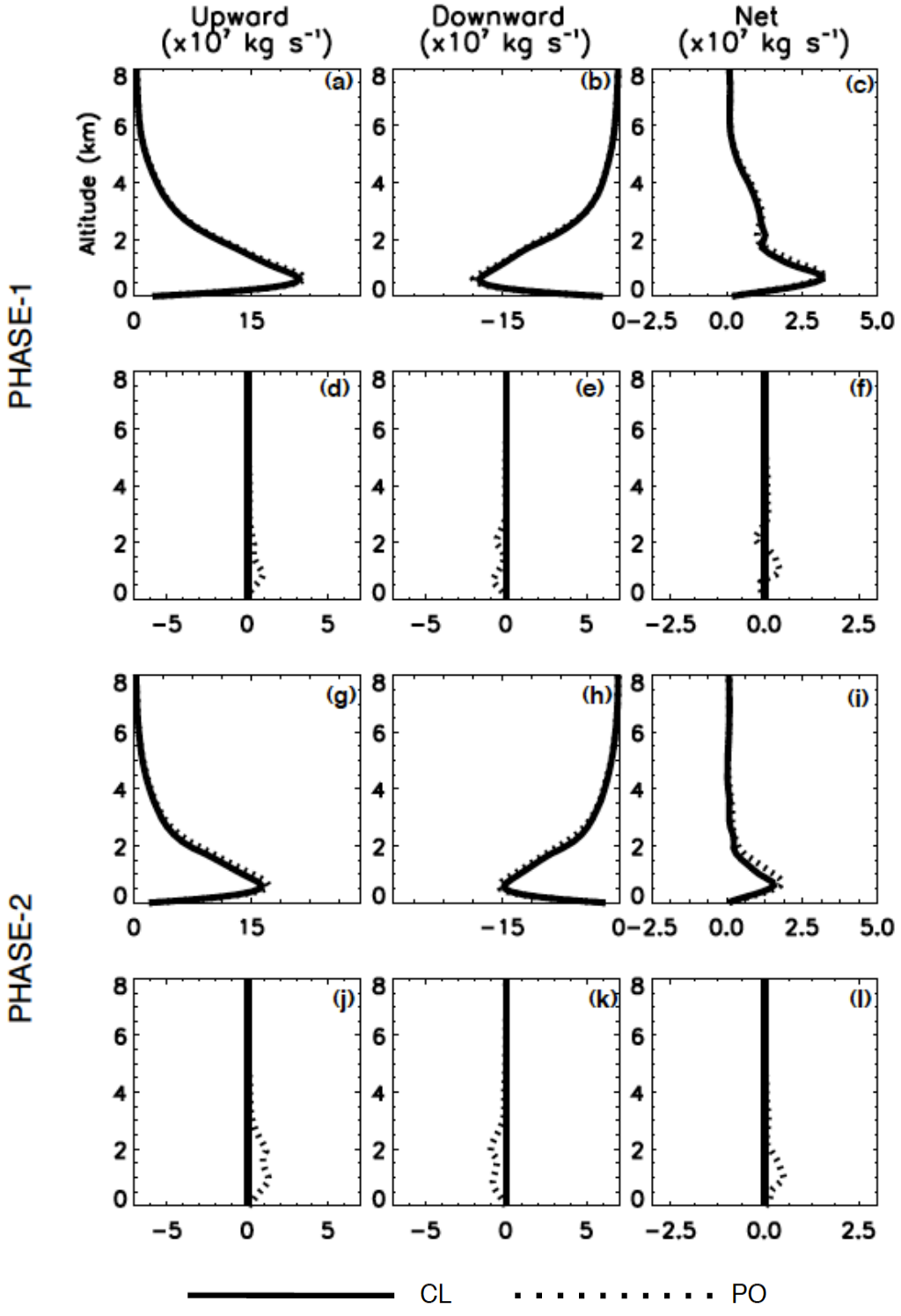

Figure 4.10: As for figure 4.9, but for the aerosol sensitivity experiment.

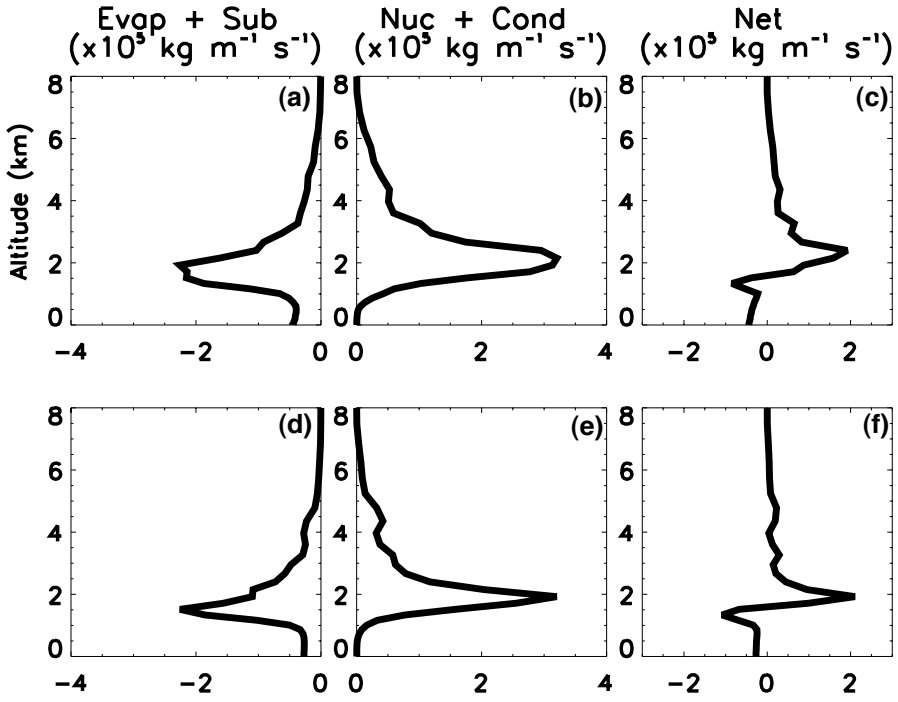

Figure 4.11: Vertical profiles of CL simulation (Grid 3) temporally averaged total rate of mass exchange (x10^5 kg m^{-1} s^{-1}) by (a,d) evaporation/sublimation of condensate, (b,e) condensation/nucleation of condensate, and (c,f) the net of these processes, for PHASE-1 (a-c) and PHASE-2 (d-f).

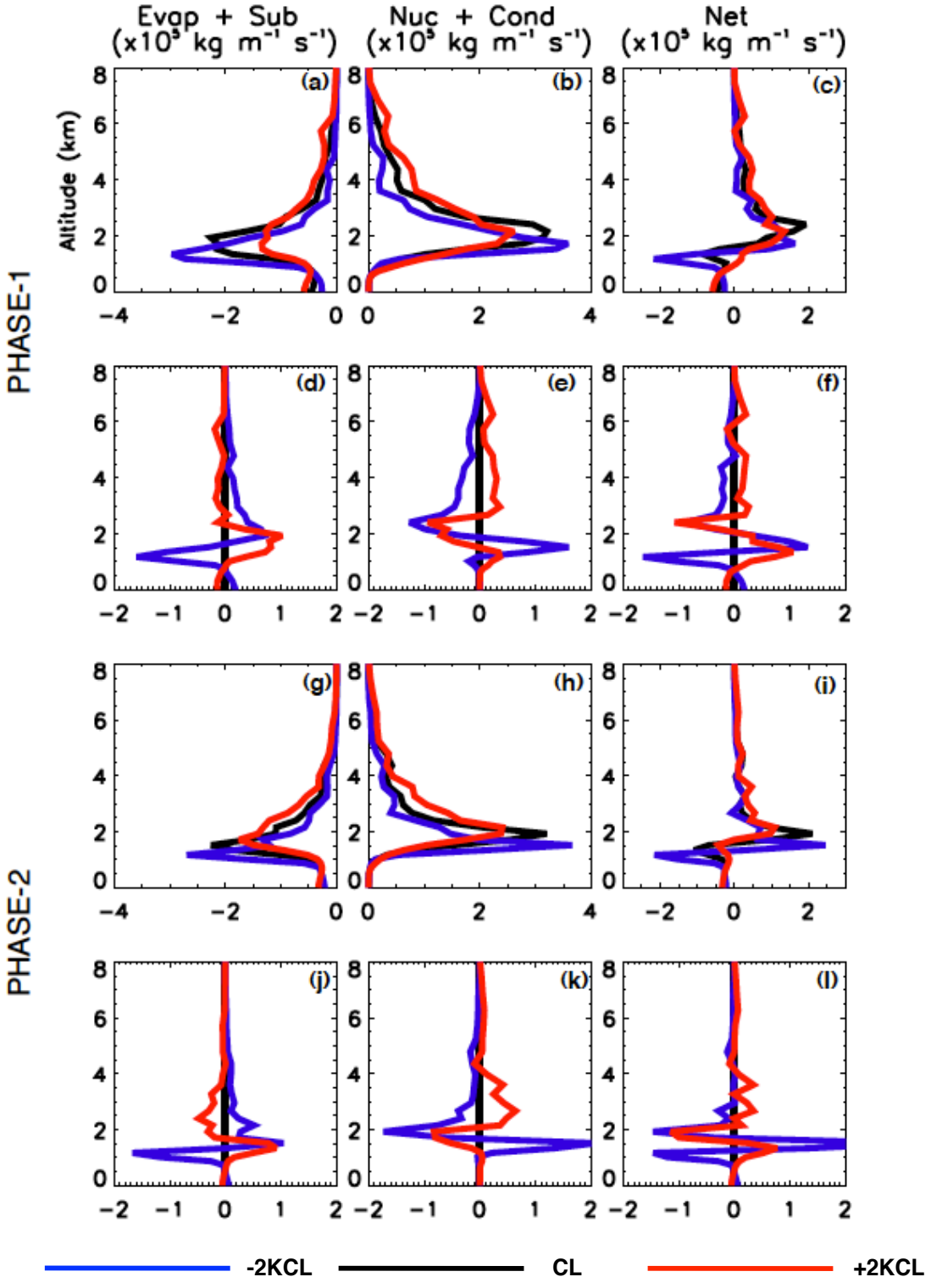

Figure 4.12: As for figure 4.11, but for the SST sensitivity experiments, including the difference from the average CL profile (d-f, j-l) for PHASE-1 (a-f) and PHASE-2 (g-l).

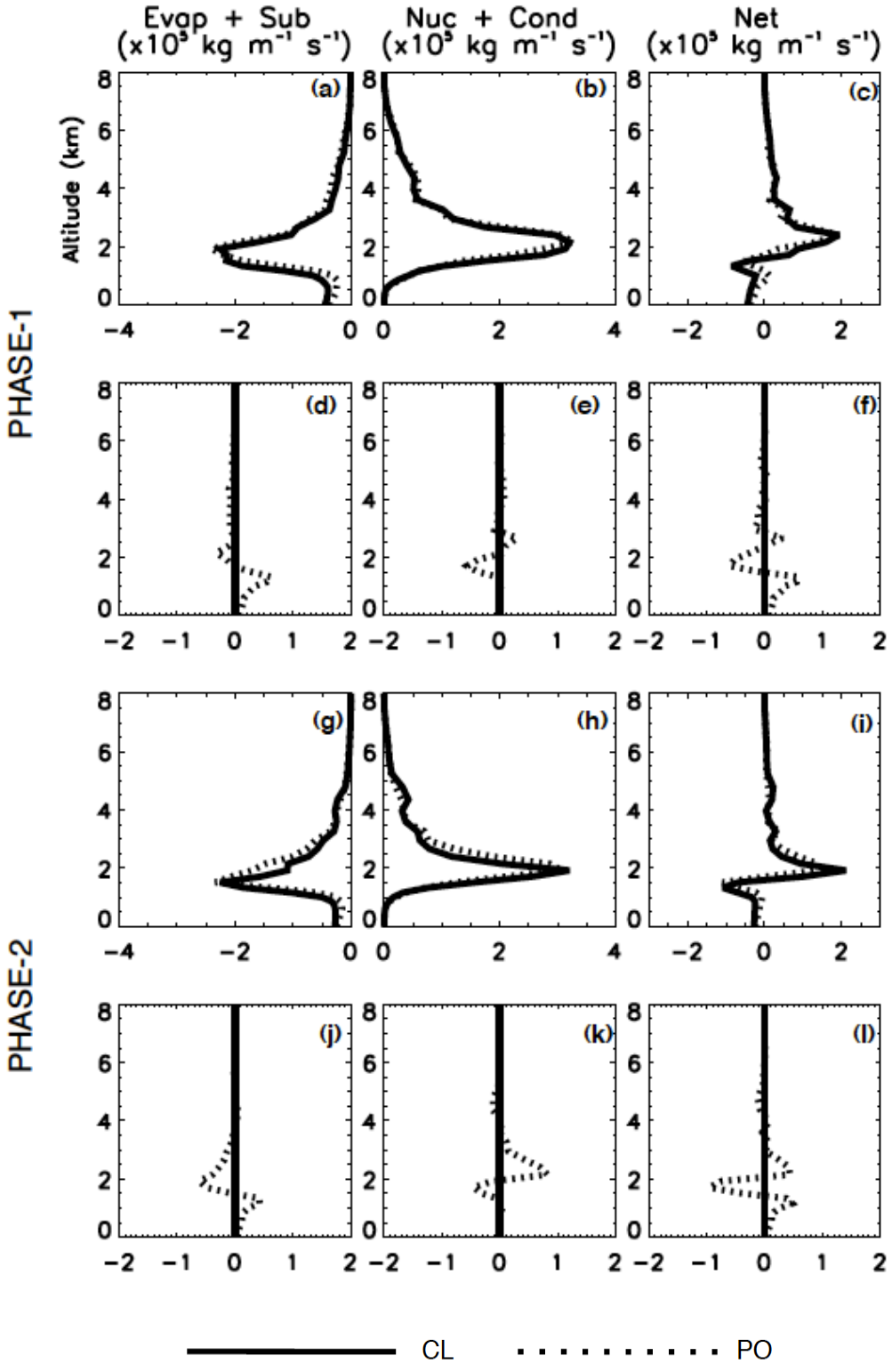

Figure 4.13: As for figure 4.12 but for the aerosol sensitivity experiment.

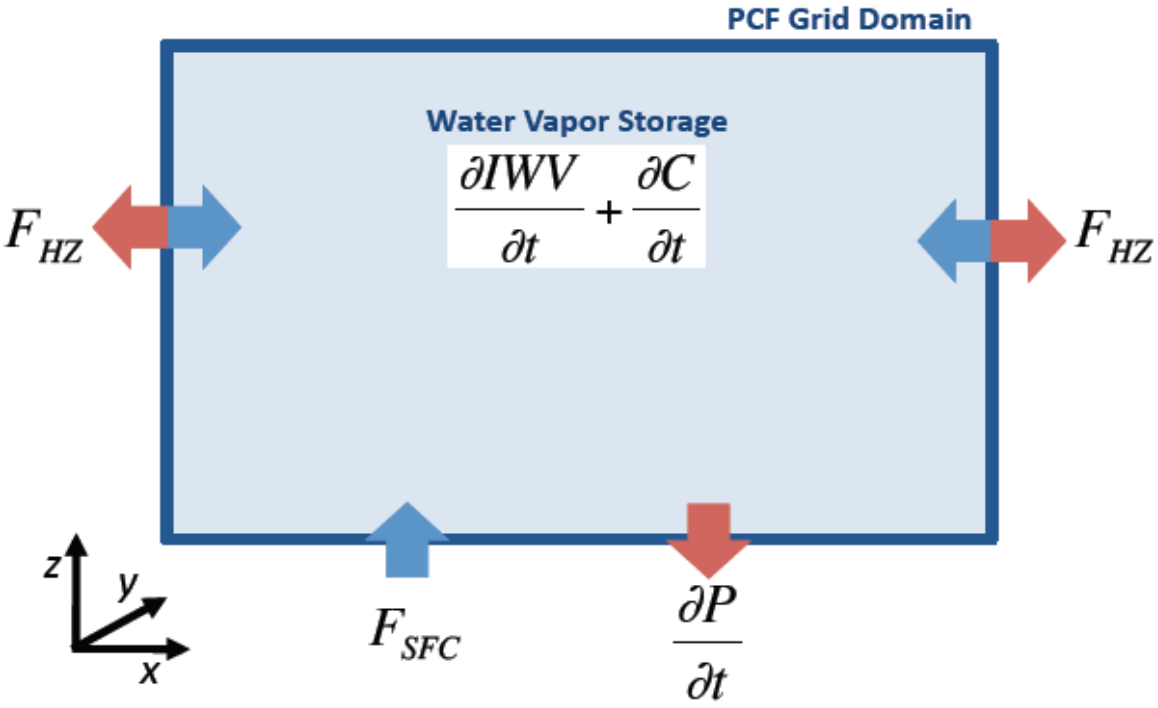

Figure 4.14: Schematic of terms in equation (4.4) in the PCF grid domain (i.e. Grid 3).

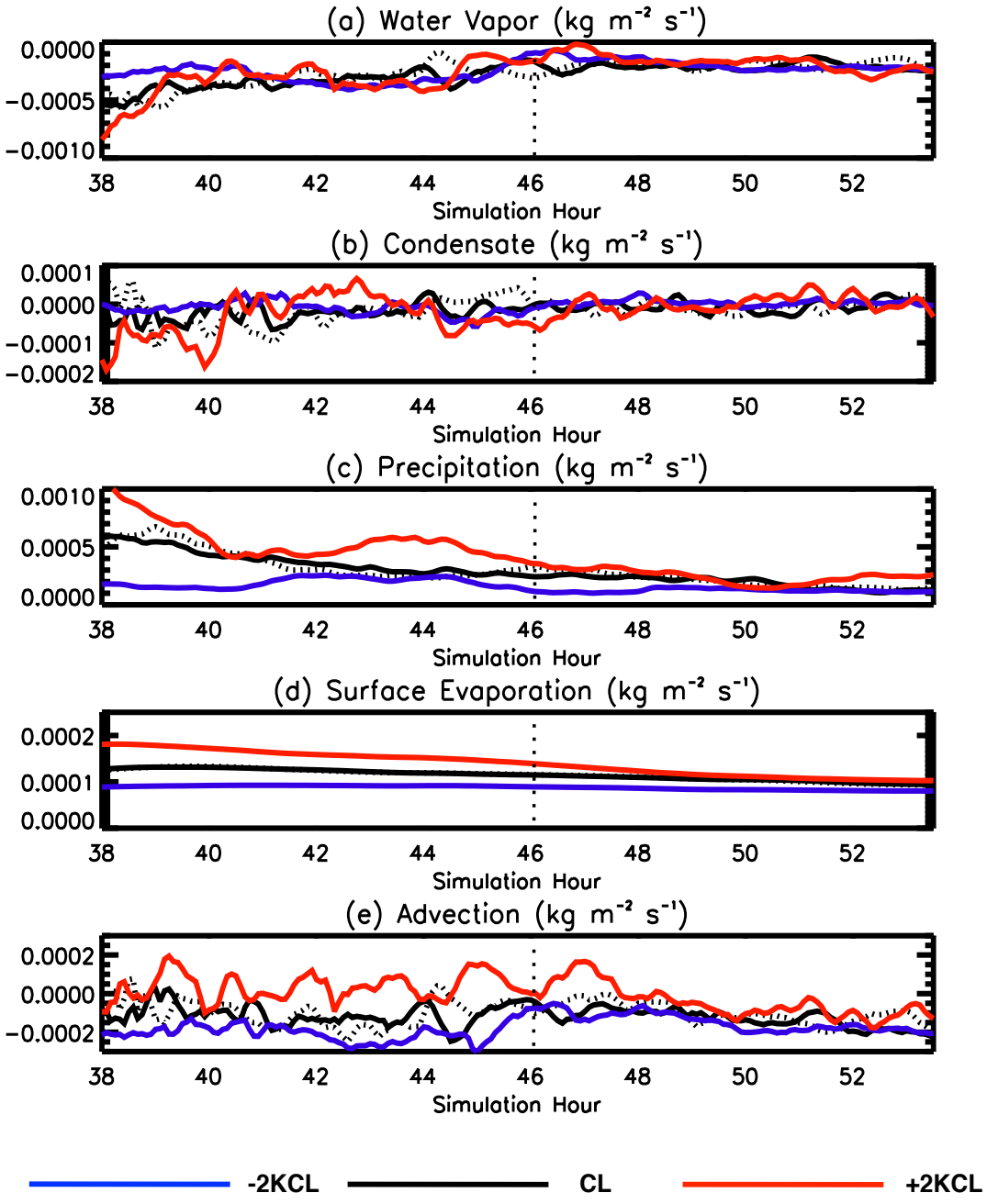

Figure 4.15: Time series of the water mass flux rate per unit area (kg m^{-2} s^{-1}) of the terms in equation (4.4): (a) $\frac{\partial IWV}{\partial t}$, (b) $\frac{\partial C}{\partial t}$, (c) $\frac{\partial P}{\partial t}$, (d) F_{SFC}, and (e) F_{HZ}. The dashed line at 46 hours indicates PHASE-1 and PHASE-2.

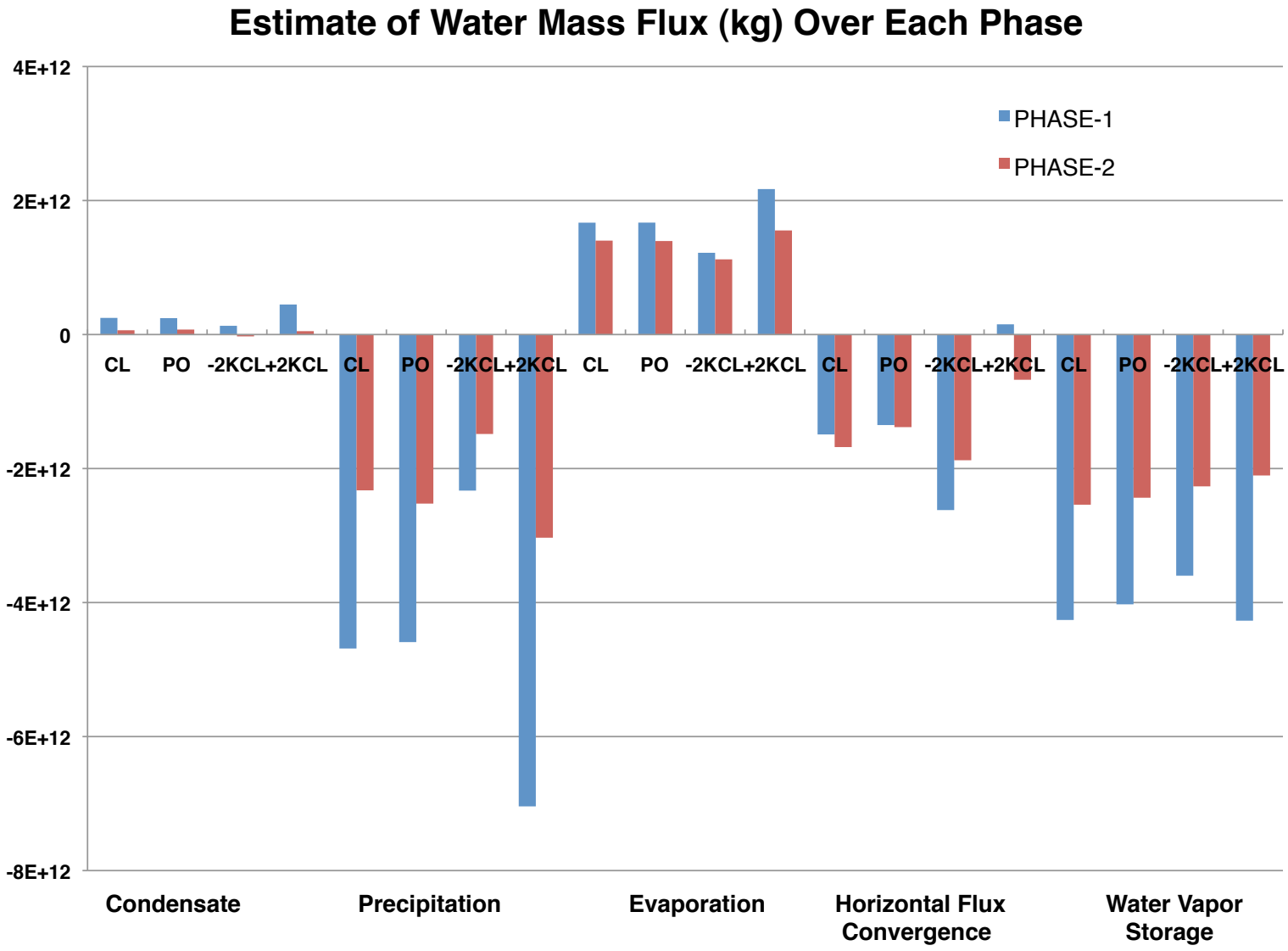
Estimate of Water Mass Flux (kg) Over Each Phase
4E+12
2E+12
0
-2E+12
-4E+12
-6E+12
-8E+12
PHASE-1
PHASE-2
CL
PO
-2KCL+2KCL
Condensate
Precipitation
Evaporation
Horizontal Flux Convergence
Water Vapor Storage

Figure 4.16: Cumulative flux of water mass (kg) in PHASE-1 (blue) and PHASE-2 (red) for the terms in equation 4.4 for each simulation (CL, PO, -2KCL, +2KCL). Positive processes indicate a source and negative processes indicate a sink of water vapor mass.

5. TRANSPORT OF PASSIVE TRACERS BY AN EXTRATROPICAL CYCLONE

5.1 INTRODUCTION

As discussed in B10 and B11 and in the previous chapters (figure 4.1), the transport of water vapor between the cold frontal, PCF, and warm sector regions of an ETC is due to the balance between the advective and surface source of water vapor and the local convective-evaporative-precipitation cloud processes. The balance between these processes in maritime clouds of the PCF region was analyzed in Chapter 4. In this chapter, the transport pathways of lofted moisture will be examined. This will be facilitated through the use of surface based passive tracers released in different regions of the ETC. Examining these pathways will allow us to answer several questions about ETC transport including: (1) how are passive tracers that are ventilated by the PCF region transported throughout ETCs? (2) how does the mesoscale and/or synoptic scale lofting of passive tracers compare between different ETC sectors? (3) what is the relative role of these mechanisms in the long-range transport of ETC? and (4) how does increased ETC intensity (as may occur with increased SST) impact this transport?

Answering these questions will allow us to compare the importance of different lofting mechanisms within ETCs and to assess the relative importance of the PCF region compared with other features such as the WCB, and as well as the role of other processes such as advection and convergence. While not an exact analogy, this tracer transport can be interpreted as the possible routes of water vapor or aerosol species through ETCs once they are lofted from the surface, and is similar in approach to that taken in the study of B11.

As described in section 2.2B, five passive tracers (P1, P2, W3, W4, TR5) were released in different sectors of a mature ETC in a high-resolution, large domain single grid simulation.

These tracers were initialized at the start of the simulation and were not updated in time. An additional passive tracer (SFC-TRACER) was released across the entire model domain and continuously replenished from the lowest model level. All of the passive tracers are massless and are advected and dispersed throughout the domain without interacting with cloud microphysical processes.

Transport pathways of all six passive tracers will first be examined for the single grid CL simulation. Following this, a comparison between the SFC-TRACER transport pathways for the CL and +2KCL simulation will be shown in order to examine the impacts of ETC intensity through increased SST.

5.2 EXTRATROPICAL CYCLONE LOFTING OF SURFACE TRACERS BY SECTOR

This section will examine the transport of the five passive tracers (P1, P2, W3, W4, TR5) initiated in separate sectors of our simulated ETC (figure 2.7). Figures 5.1-5.2 and figures 5.4-5.6 show plan views of sea level pressure (black contours) and the vertically integrated number of passive tracers in an atmospheric column, shown as a percentage of the initial number of tracers in the grid domain (shading). The percentage of each tracer was calculated by vertically integrating the number of each tracer at each time and then dividing this integrated value by the total number of tracer initially released. Thus, figures 5.1-5.2 and figures 5.4-5.6 represent the temporal redistribution of tracers as a percentage of the initial total number of tracers. The number of tracers is conserved until such time as they are advected through the lateral boundaries, which in the case of these simulations occurs at the northern and eastern boundaries. Also, as the initial total number concentration was the same for all of the different tracers released, the percentage contributions are directly comparable between the tracers. The percentages are represented using a logarithmic scale, and we have utilized a jump to larger

values partway on the legend due a large percentage of the tracers remaining in a concentrated area. Please note the shading contour scale difference between figures 5.1 and 5.4 compared to figures 5.2, 5.5, and 5.6. Figure 5.3 is similar to these figures, except shows the difference between the P1 and P2 tracer percentages found in figures 5.1 and 5.2 in order to compare the different transport pathways of the PCF tracers.

In order to examine the lofting of the passive tracers further, east-west cross sections of tracer concentration (shading; $x10^7$ m^{-3}) and potential temperature (black contours; K) from 1, 2 and 4 simulation hours after the release of the tracers are shown in figure 5.7. Again, a logarithmic scale is used. The location of each cross section is marked on panels (a) of figures 5.1-5.2 and figures 5.4-5.6 and is at the same latitude for each cross section. In addition, Table 5.1 shows the percentage of the initial number concentrations of P1, P2, W3, W4, and TR5 tracers in several atmospheric layers (0-2km, 2-6km, 6-9km, and 9km to TOA) as a function of hours after release. Each respective tracer number was summed vertically and horizontally over the corresponding layer in the grid domain. These layers were chosen in order to divide the atmosphere into the BL and mid-troposphere, with an additional summation for the highest altitudes. The total percentage in all layers may not total 100% due to the advection of tracers out of the grid domain.

A. POST-COLD FRONTAL REGION

The P1 and P2 tracers were initiated in the PCF region, with P1 behind the primary cold front and P2 behind the secondary cold front that is beginning to form at this time (figure 2.7). The local convection, mixing, and large-scale lifting will determine the altitude to which the tracers are transported. This, in turn, will impact the horizontal transport as the synoptic scale winds increase with height. The sinking motion of the DCB also impacts the PCF region.

Both the P1 and P2 tracers are initially transported to the east and northeast (panels a-b in figures 5.1, 5.2). Near 10-12 hours after initialization, both tracers reach the eastern and northern lateral edges of the grid domain (panels e-f in figures 5.1, 5.2). In spite of starting at the same latitude, the P1 tracer reaches further north faster than the P2 tracer, while the P2 tracer extends further south than the P1 tracer (figure 5.3). This southern extension difference is ~5 degrees latitude after 12 hours (figures 5.1f, 5.2f). Both tracers reach the cyclonic and anticyclonic turning of the WCB in the mid-to-upper troposphere.

Differences exist in the primary mechanisms lofting the P1 and P2 tracers into the large-scale flow. The P1 and P2 tracers are initially ventilated off the surface by BL turbulence, and some reach the free troposphere due to PCF clouds (figure 5.7a,d). Additionally, some of both the P1 and P2 tracers are immediately transported eastward in both the BL and the free troposphere and subsequently lofted by their respective cold fronts to the mid-troposphere. For example, the primary cold front is near 148^{o} W at 1 hour after the tracers were released. The P1 tracers are located to the west of this front (figure 5.7a). The secondary cold front, which contains even colder air, can be found nearer 152^{o} W, and the P2 tracers are located to the west of this front (figure 5.7d). One can get a better sense of the locations of the frontal locations by examining the vertically integrated SFC-TRACER number (figure 5.8). The SFC-TRACER will be examined in section 5.3, but the lofting by the primary cold front and near the ETC center and warm front is evident over the 2 to 12 hours of SFC-TRACER lofting and give a sense of these frontal locations.

Within two hours of release, less than 1% of the P1 and P2 tracers have been lofted above the BL (table 5.1). Instead, a significant portion of the P1 and P2 tracers remain in a small,

concentrated ‘packet’ near the surface (< 2-3 km ASL). These BL ‘packets’ are then transported eastward towards the cold fronts (panels a-b in figures 5.1, 5.2).

While some P1 tracers are lofted into the free troposphere in the PCF region, the majority of P1 tracers remain below the PCF BL inversion in the first 1-2 hours (figure 5.7a,b). This is similar to the capping of cumulus cloud development by the PCF BL inversion nearest the primary cold front in PHASE-1 discussed in Chapter 3. Subsequently, the P1 tracer BL packet is transported to the northeast in association with the strong cyclonic motion near the ETC center (figure 5.1), leaving a relatively small number of tracers in the PCF region to be lofted by the passage of the secondary cold front (figure 5.7c). Due to its initial proximity to the primary cold front and to the southeast of the ETC center, the packet of P1 tracers reaches the primary cold frontal region faster than the P2 tracers and achieves a more northerly location closer to the ETC center (figure 5.1c). The initial location of the P1 tracer allows for the packet of tracers to be swept into the cyclonic flow of the ETC and propagate polewards and then around the ETC center. Hence, as the P1 tracers propagate northeastward, they are entering the warm sector from behind the primary cold front and are lofted by the occluding front. This horizontal transport within the BL towards the primary cold front and the cyclone center results in relatively large numbers of P1 tracers (table 5.1) reaching the free troposphere away from the PCF region, whereas relatively small amounts of vertical lofting out of the BL occurs in the PCF region itself due to the BL inversion.

Unlike the P1 tracers, the P2 tracers in the PCF region are lofted to higher altitudes (2-3 km ASL) above the BL within 1-2 hours (figure 5.7d,e). This is similar to PHASE-2 examined in Chapter 3, where a weaker BL inversion allowed more deeper cumulus and congestus type clouds which would transport tracers out of the BL. Additionally, the P2 tracers are swept south

and eastward in the diffluent flow associated with the secondary cold front that is forming (figure 5.2b,c). Four hours after release, the P2 tracers have propagated sufficiently far eastward to be lofted by the primary cold front circulations (figure 5.7f), but at a more southerly location than the P1 tracers. While some P2 tracers do propagate northeastward and into the upper level westerlies, the P2 packet of tracers is spread in a northwest to southeast crescent shape behind the primary cold front (figures 5.2d-f, 5.3d-f). This more southerly location compared to that of the P1 tracers is due to the P2 tracer packet not being swept north near the cyclonic center, and instead in a more southerly and easterly direction around the surface trough as the ETC center propagates to the northeast. Hence, the P2 tracers are being lofted in the PCF region more than the P1 tracers due to the weaker BL inversion, but the majority of tracers yet propagate in the BL towards the primary cold front.

Within twelve hours of being released, a significant portion of the P1 tracers (> 50%) are above 2 km compared to only ~9% of the P2 tracers (table 5.1). This is due to the large number of P1 tracers that are lofted vertically off the surface closer to the ETC center and the subsequent east-northeast transport (figure 5.1f, 5.3). During the 12 hours following the release of the tracers, the ETC has become occluded as the primary cold front has caught up to the warm front. Thus, as the P1 tracer packet reaches close to the occluded front, the tracers are lofted out of the BL by the front and enter the large-scale flow. This results in a greater concentration of P1 tracers further north than the P2 tracers (figure 5.3) and a greater number of tracers in the free troposphere (table 5.1). Vertical lofting of the P2 tracers in the PCF region and by the secondary and primary cold front in the first 2-8 hours is small (table 5.1). The vertical lofting by the primary cold is primarily responsible for the increasing amounts of P2 tracer above 2 km ASL at

10-12 hours and will likely increase the concentration beyond 12 hours. A few P2 tracers do get lofted near the frontal occlusion, but in smaller quantities than P1 (figure 5.3f).

B. WARM SECTOR

The W3 tracer was initially released in the warm sector, to the east of the primary cold front and to the southeast of the ETC center. A number of W3 tracers are initially transported east-southeastward after being lofted from the surface (figures 5.4a,b, 5.7g-i). However, similar to the P1 tracer, a packet of W3 tracers is transported to the north (figures 5.4c-f, 5.7i). Twelve hours after their release, a significant portion (~70%) of the W3 tracers are still located under 2 km ASL (table 5.1). However, at least some of the W3 tracers follow the WCB trajectory and are lofted from the warm sector BL north over the warm front to the mid-troposphere (figure 5.4f). More than 28% (5%) of the initial tracers reach above 2 (6) km ASL (table 5.1), which is greater than the lofting of both the P1 and P2 tracers in the PCF region before they interact with the primary cold and occluded fronts. Additionally, some W3 tracers cyclonically circulate the ETC center near 2-4 km ASL (figure 5.4f).

C. AHEAD OF THE WARM FRONT

The W4 tracer was released ahead of the warm front, to the northeast of the cyclone center. W4 tracers are primarily transported (figure 5.5) to the southwest around the cyclone center and to the north with the ETC propagation. A few W4 tracers are transported to the east. Similar to the previous tracers, a concentrated packet of W4 tracers is transported along the surface, primarily to the west-southwest (figures 5.5d, 5.7m-o). However, the W4 tracer lacks a strong local or large scale lofting mechanism to ventilate the tracers. While a few tracers reach the upper levels within 12 simulation hours (< 0.05%) (table 5.1), by far the majority remains under 1 km, being trapped by the warm frontal inversion. The few W4 tracers that are lofted to

the free troposphere are lifted by the CCB, including those propagating west-southwestward (i.e. the cyclonic branch of the CCB) and to the east (i.e. the anticyclonic branch of the CCB).

D. NORTHWEST OF THE EXTRATROPICAL CYCLONE CENTER

Lastly, the TR5 tracer was released to the northwest of the ETC center. While the WCB, CCB, and DCB tend to influence the other sectors of the ETC, this region occurs below the elevated branches of the CCB and WCB. Hence, the TR5 tracers are swept cyclonically around the ETC center in the lowest levels in a thin north-south oriented band (figure 5.6f) where they remain primarily below 1-2 km ASL (figure 5.7j-l). Only ~2% of the TR5 tracers are lost to the northern lateral boundary due to the proximity of the initial tracer location. After 12 hours, these tracers begin to enter the PCF region where they may be lofted and transported in a manner similar to the P2 tracers.

5.3 EXTRATROPICAL CYCLONE LOFTING OF SFC-TRACER

The release of passive tracers from different ETC sectors discussed in the previous section allowed for an examination of the dependence of long-range passive tracer transport on the location of its source. Here, we will now examine how a continuously replenished source of passive surface tracers throughout the entire grid domain accumulates in certain regions of the simulated ETC. This continuous source of tracers can be loosely equated to the continuous oceanic source of water vapor provided through surface evaporation. As the water vapor is transported away from the sea surface, either vertically or horizontally, more water vapor can be evaporated from the surface based on the ambient conditions. The continuous replenishment of passive surface tracers (SFC-TRACER) will allow us to see how water vapor can be advected throughout the domain, as well as how it may converge within particular regions. We will compare how the ETC intensity (here from increased SST in the +2KCL simulation) influences

this advection within the ETC. Thus, the focus of the comparison will not be on the dependence of the water vapor source based on environmental conditions and instead based on the processes that loft water vapor away from the surface, and any differences between the ventilation of SFC-TRACER between the +2KCL and CL simulations examined here would likely be intensified if the tracer concentration was altered according to the local surface fluxes.

Figure 5.8 is a horizontal plan view of the vertically integrated number (x 10^{19}) of SFC-TRACERs from the CL simulation in each atmospheric column at each grid point (shaded) overlaid with sea level pressure at two hour intervals following the introduction of the tracer. The integrated number shading utilized in figure 5.8 starts at values greater than zero in order to highlight the regions of primary lofting or convergence. Ventilation of the SFC-TRACER in the ETC of the CL simulation is primarily associated with the warm and cold fronts, and in the PCF region. Higher tracer concentrations are also evident in association with the cyclone's low-pressure center. East-west cross sections of the SFC-TRACER at hour 12 (figure 5.9) show these lofting mechanisms. A cross section in the northern and southern region of the ETC at 12 hours has been provided to examine the lift along each front and the PCF region. Ventilation is first noticeable along the primary cold and warm front (figure 5.8). PCF lofting becomes more noticeable near 6-12 hours (figure 5.8c-f). After 12 hours, the largest accumulation of tracers in the free troposphere is along the primary cold front (figure 5.8f, figure 5.9 South) and the warm front (figure 5.8f, figure 5.9 North) with widespread lofting in the PCF region (west of -145^{o} longitude in figure 5.9 South). We can see the frontal lofting midway through each cross section, while the PCF lofting is found in the western region of the more southern cross section. Lofting by the weaker secondary cold front is included in this PCF lofting.

Table 5.2 shows the vertically and horizontally integrated number (x 10^{22}) of SFC-TRACERs in the grid domain in four atmosphere layers (same layers as in Table 5.1) at several simulation hours after the initial release. As expected, the surface layer has the greatest number of tracers (table 5.2). The integrated values for the both the CL and +2KCL simulation are shown. Tracers slowly accumulate in the mid-troposphere, and after 12 hours, the lower and mid-free troposphere contains a similar magnitude of tracers, but still less than that of the BL.

SFC-TRACER ventilation mechanisms in the +2KCL simulation are similar to the CL simulation but are greater in magnitude. Figures 5.10-5.11 are similar to figures 5.8-5.9, respectively, but now show the +2KCL simulation while figure 5.12 is a difference between figures 5.10 and 5.8 at 12 hours. The simulated ETC forming over warmer SSTs has a lower central pressure and due to the increased ETC intensity and associated surface winds, increased lofting by both the warm and primary cold front, as well as the PCF region is evident (figure 5.10, figure 5.11). By the end of 12 hours, ~40% more tracers are in both the 2-6 km and 6-9 km layers (table 5.2) in the warmer SST case, while only a 1.5% increase is found in the 0-2 km layer, thus demonstrating that the ETC is efficiently lofting more tracers from the lowest levels to the free troposphere.

5.4 DISCUSSION

In this chapter the transport of massless passive tracers throughout an ETC has been examined. Five tracers (P1, P2, W3, W4, TR5) were released from the surface in different sectors of the ETC, while an additional source was continuously replenished from the surface (SFC-TRACER). Different ventilation mechanisms were responsible for the lofting of the tracers released in different ETC sectors.

B10 and B11 discussed that the PCF region both supports the WCB through providing a water vapor source from surface evaporation that converges into the warm sector within the BL, while additionally vertically ventilating moisture out of the BL in the cold sector through PCF clouds. The cloud-resolving simulations conducted here show that surface initiated PCF passive tracers (P1, P2) are lofted by PCF cloud ventilation. The P1 tracers are lofted less by PCF convection than the P2 tracers due to the strong BL inversion, similar to the capped cumulus clouds in PHASE-1 examined in Chapter 3. However, the primary lofting of PCF tracers occurs near larger-scale ETC features as the large concentration of tracers remaining in the BL is transported away from the PCF region. While a few PCF initiated tracers reach the upper level flow within 6 hours of release, the majority of the tracers are not transported aloft until the packet of surface tracers concentrated under 1 km ASL reaches the primary cold front and the occlusion. Thus, the P1 and P2 tracers are lofted in the PCF region, but a large percentage of the P1 tracer is lofted away from the PCF region. This BL transport from the PCF region to other sectors of the ETC is in keeping with the results shown in B10 and B11. Both tracers enter the upper levels and the associated eastward long-range transport, although much smaller amounts of the P2 tracer reach these levels.

As the cold fronts, and ultimately the occluded front, are the primary lofting mechanisms, the location of the initial source in relation to the primary and secondary cold fronts (such as P1 vs. P2) makes a significant difference in the overall transport. We were able to capture the northeastward propagation and lofting of P1 tracers in association with the frontal occlusion, while the P2 tracers accumulated predominantly to the west of the primary cold front after initially being transported southeastward. The accumulation of the P2 tracers behind the primary cold front, including above the BL, resembles more the accumulation of PCF tracers of the study

of B11. The P1 tracers, on the other hand, reflect the transport within the BL from the PCF region to the WCB source region. While the lofting of PCF tracers by PCF convection is present, it is relatively small compared to the larger-scale processes, at least for the tracer setup used here.

In the 12 simulation hours examined here, the P1 tracers were lofted to the free troposphere more than the other sector-released tracers (W3, W4, TR5). The next largest transport occurs through the lofting of the W3 tracer from the warm sector to above the warm front following the WCB trajectory. B10 and B11 discussed the comparative lofting by the WCB and the PCF convection. Here, we find the WCB lofting to be greater than the PCF lofting in contradiction to the studies of B10 and B11. The W4 and TR5 tracers are slow to be ventilated above the BL although the W4 tracer is lifted by the CCB. However, the cyclonic motion of the ETC may introduce the tracers to other regions, such as the PCF region, where they maybe ventilated further.

Use of the SFC-TRACER allowed us to examine the cumulative lofting by the warm front, the cold fronts, and the PCF region. Similar to B11, tracers accumulated slightly west of the cold front in the BL and the lower free troposphere. In the ETC that developed over warmer SSTs, ~40% more tracers were lofted to the free troposphere after 12 hours due to the increased ETC intensity.

While passive tracers cannot fully encompass how water vapor is processed in the atmosphere due to the lack of cloud processing and radiation impacts, passive tracers can show the lofted water vapor transport pathways if ventilation does occur. If ETC intensity increases in our future climate (e.g. Field and Wood 2007), greater amounts of water vapor can be fluxed through the ETC. We did not account for an increased amount of passive tracers due to increasing SSTs. Hence, the results here are likely to be even more enhanced due to the stronger

storm circulation coupled with the greater water vapor contents. Another transport pathway analogy can be made to aerosol particles as BL ventilation can occur through convection. If the aerosols are also non-soluble, not cloud processed (i.e. used to formed cloud condensate), or regenerated, then vertical fluxing of aerosols into the free troposphere and long range transport would occur along these passive tracer transport pathways. And, if the ETC is intensified, increased ventilation of aerosol pollution is likely. This increased lofting would have consequences on both ETC development, radiation through direct effects, and long-range transport.

Table 5.1: Percentage of vertically and horizontally integrated initial number of P1, P1, W3, W4, and TR5 tracers in several atmospheric layers (0 to 2 km, 2 to 6 km, 6 to 9 km, 9 km to TOA) after several simulation hours after initial release (columns in the table). Each set of layers at each simulation hour may not sum up to 100% due to advection of tracers out of the domain.

	Simulation Hour						
Tracer	**0**	**2**	**4**	**6**	**8**	**10**	**12**
P1							
0 to 2 km	100%	98.53%	88.10%	80.10%	69.04%	52.31%	42.60%
2 to 6 km	0%	0.80%	8.85%	13.15%	19.45%	27.00%	29.05%
6 to 9 km	0%	0%	1.24%	4.02%	7.70%	15.40%	21.96%
9 km to TOA	0%	0%	<0.01%	<0.01%	<0.01%	0.04%	0.17%
P2							
0 to 2 km	100%	98.85%	98.62%	97.82%	91.60%	88.43%	86.51%
2 to 6 km	0%	0.40%	0.11%	0.10%	5.39%	7.93%	8.92%
6 to 9 km	0%	<0.01%	<0.01%	<0.01%	<0.01%	0.03%	0.48%
9 km to TOA	0%	0%	0%	<0.01%	<0.01%	<0.01%	<0.01%
W3							
0 to 2 km	100%	99.72%	99.40%	99.88%	94.50%	83.26%	69.57%
2 to 6 km	0%	<0.01%	0.03%	0.32%	3.78%	12.11%	22.56%
6 to 9 km	0%	0%	<0.01%	<0.01%	0.44%	2.59%	5.89%
9 km to TOA	0%	0%	0%	<0.01%	<0.01%	0.02%	0.15%
W4							
0 to 3 km	100%	99.63%	97.51%	96.24%	93.36%	73.93%	58.12%
3 to 6 km	0%	0.22%	2.05%	3.13%	3.91%	1.91%	0.04%
6 to 9 km	0%	0%	0%	0%	0%	<0.01%	<0.01%
9 km to TOA	0%	0%	0%	0%	0%	0%	0%
TR5							
0 to 2 km	100%	99.86%	99.61%	99.20%	97.10%	94.85%	93.60%
2 to 6 km	0%	<0.01%	0.12%	0.42%	2.26%	4.24%	4.97%
6 to 9 km	0%	0%	<0.01%	<0.01%	<0.01%	<0.01%	<0.01%
9 km to TOA	0%	0%	0%	0%	0%	0%	0%

Table 5.2: Vertically and horizontally integrated number of SFC-TRACERs (x10^{22}) in each atmospheric layer (same as in Table 5.1) after several simulation hours following the tracer release. Values for both the climatological SST simulation (CL) and the increased SST simulation (+2KCL) are shown.

	Simulation Hour					
	2	**4**	**6**	**8**	**10**	**12**
Climatological SSTs (CL)						
0 to 2 km	290.60	395.25	465.63	518.21	558.21	587.40
2 to 6 km	3.57	13.36	26.14	39.84	52.76	63.37
6 to 9 km	0.35	2.40	6.14	10.76	16.60	22.58
9 km to TOA	0.00002	0.002	0.01	0.04	0.14	0.31
Increased SST (+2KCL)						
0 to 2 km	300.83	404.97	473.64	526.89	566.85	595.45
2 to 6 km	7.06	22.22	40.18	56.46	72.86	88.27
6 to 9 km	1.12	4.82	10.79	18.26	26.44	33.20
9 km to TOA	0.002	0.02	0.06	0.13	0.37	0.84

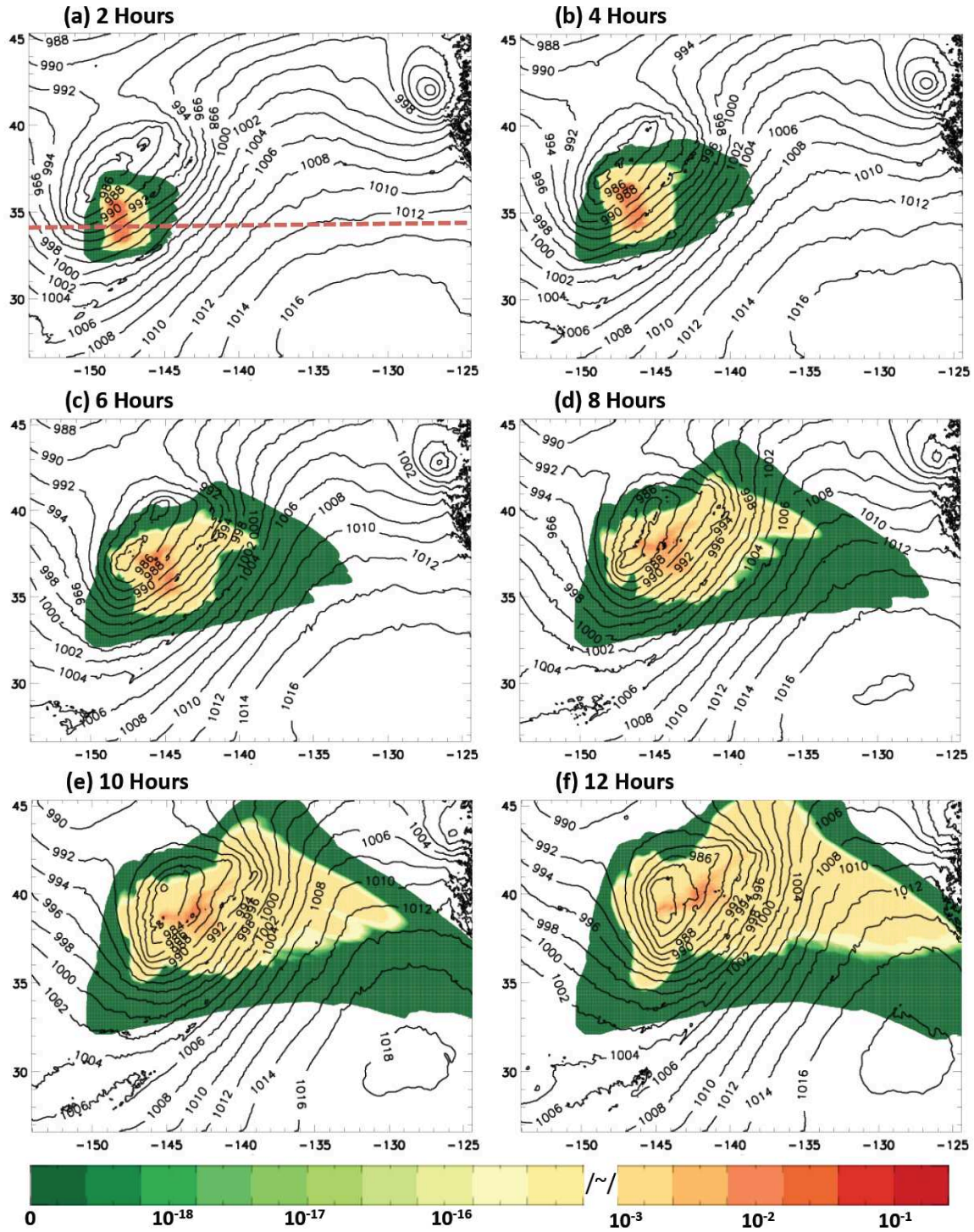

Figure 5.1: Horizontal plan view of vertically integrated number of P1 tracer expressed as a percentage of the initial total tracer number concentration (shaded) at (a) 2, (b) 4, (c) 6, (d) 8, (e) 10, and (f) 12 hours after the introduction of the tracer. Sea level pressure is contoured in black (hPa). The dashed line on panel (a) is the locations of cross-sections examined in figure 5.7.

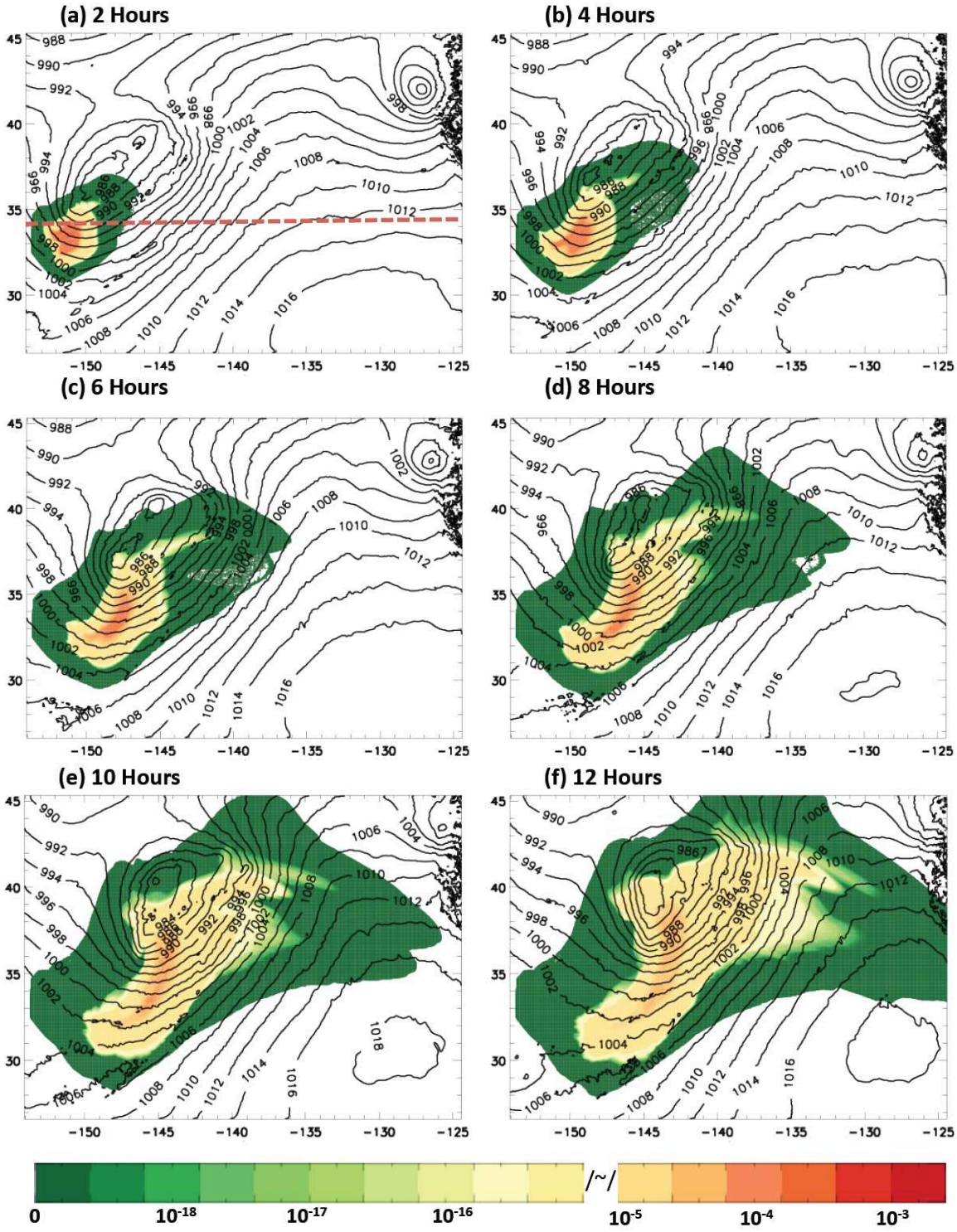

Figure 5.2: As for figure 5.1, but for the P2 tracer. A different contour scale from figure 5.1 has been used.

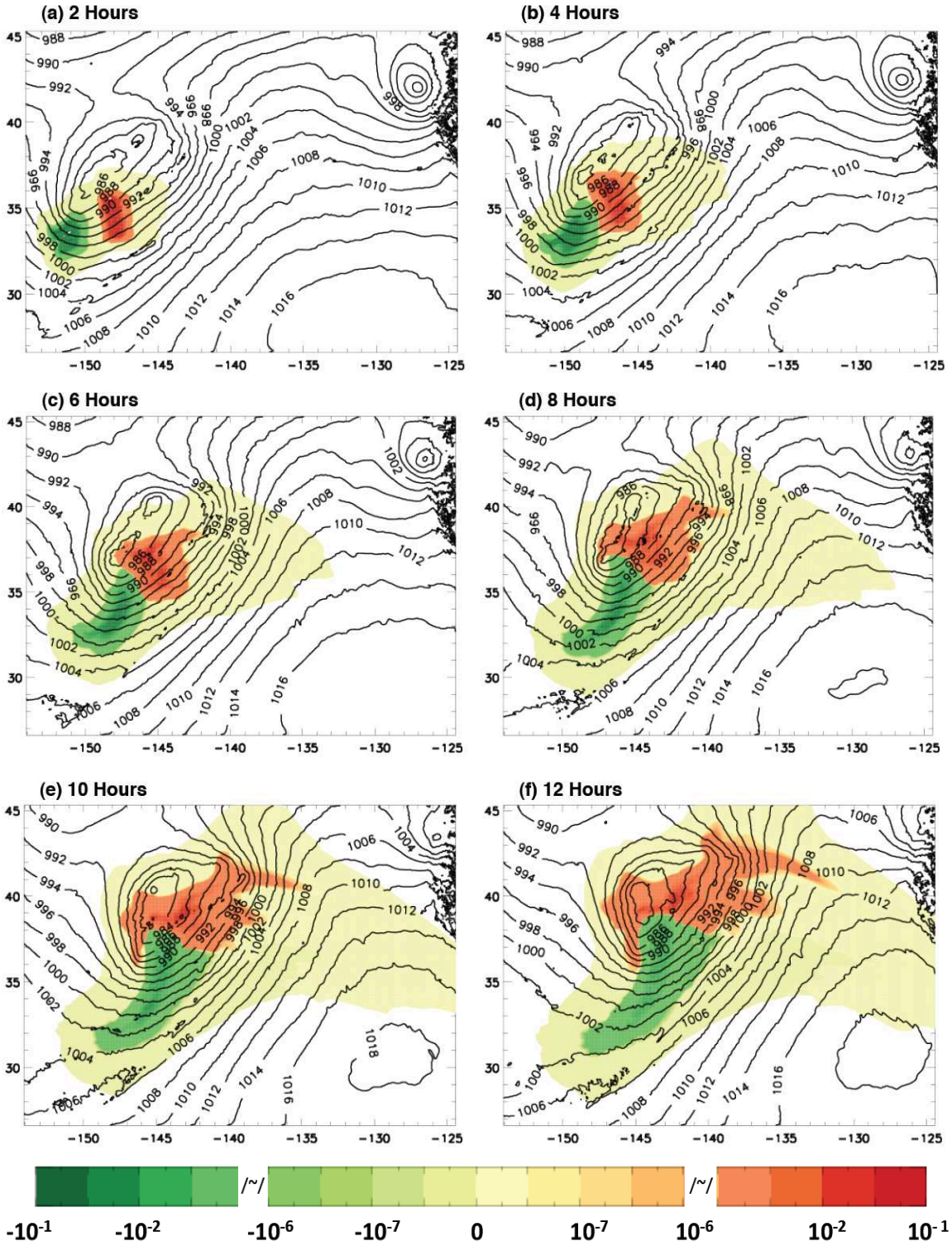

Figure 5.3: Horizontal plan view of difference in P1 and P2 tracer percentages from figures 5.1 and 5.2 (shaded) at (a) 2, (b) 4, (c) 6, (d) 8, (e) 10, and (f) 12 hours after the introduction of the tracer. Sea level pressure is contoured in black (hPa).

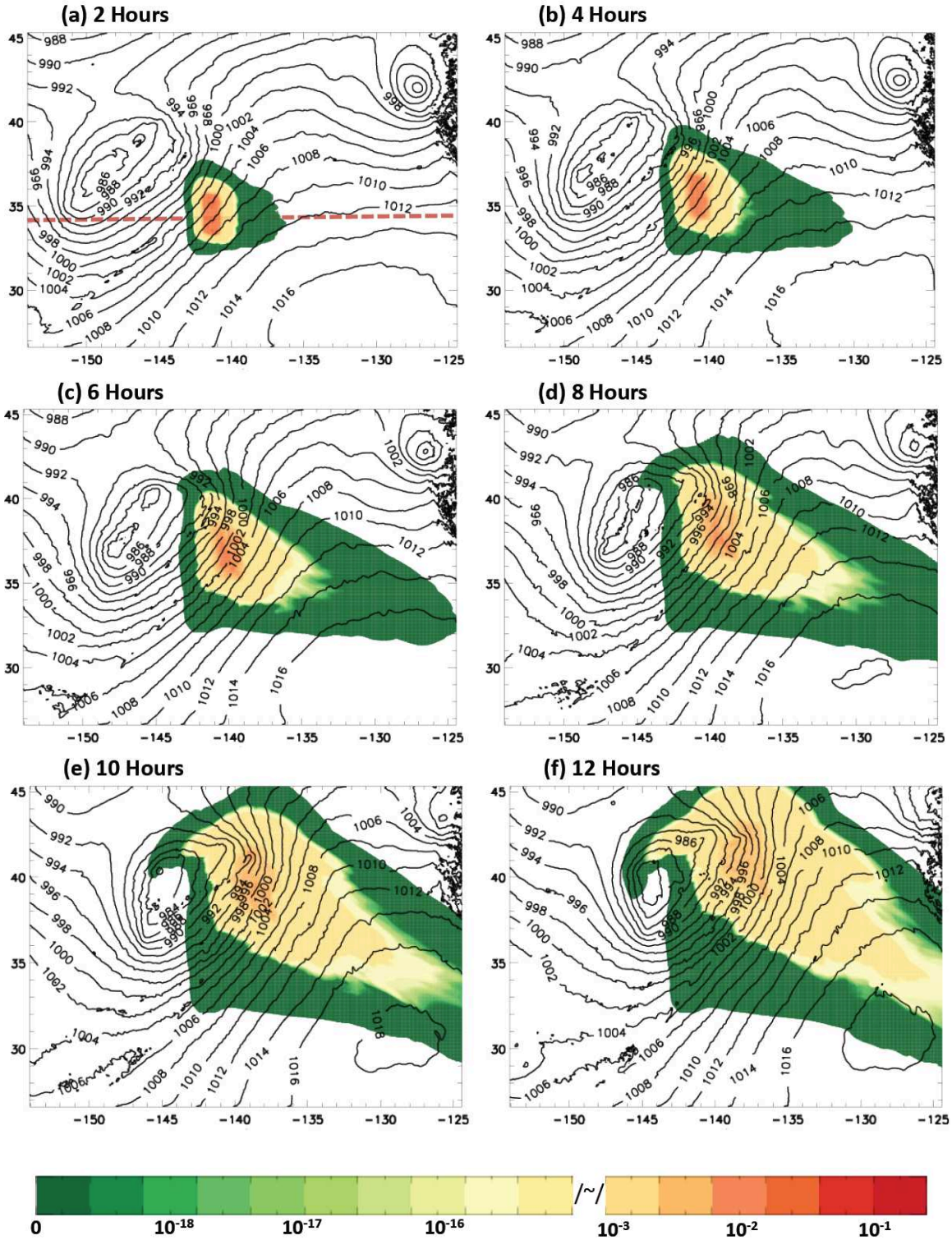

Figure 5.4: As for figure 5.1, but for the W3 tracer.

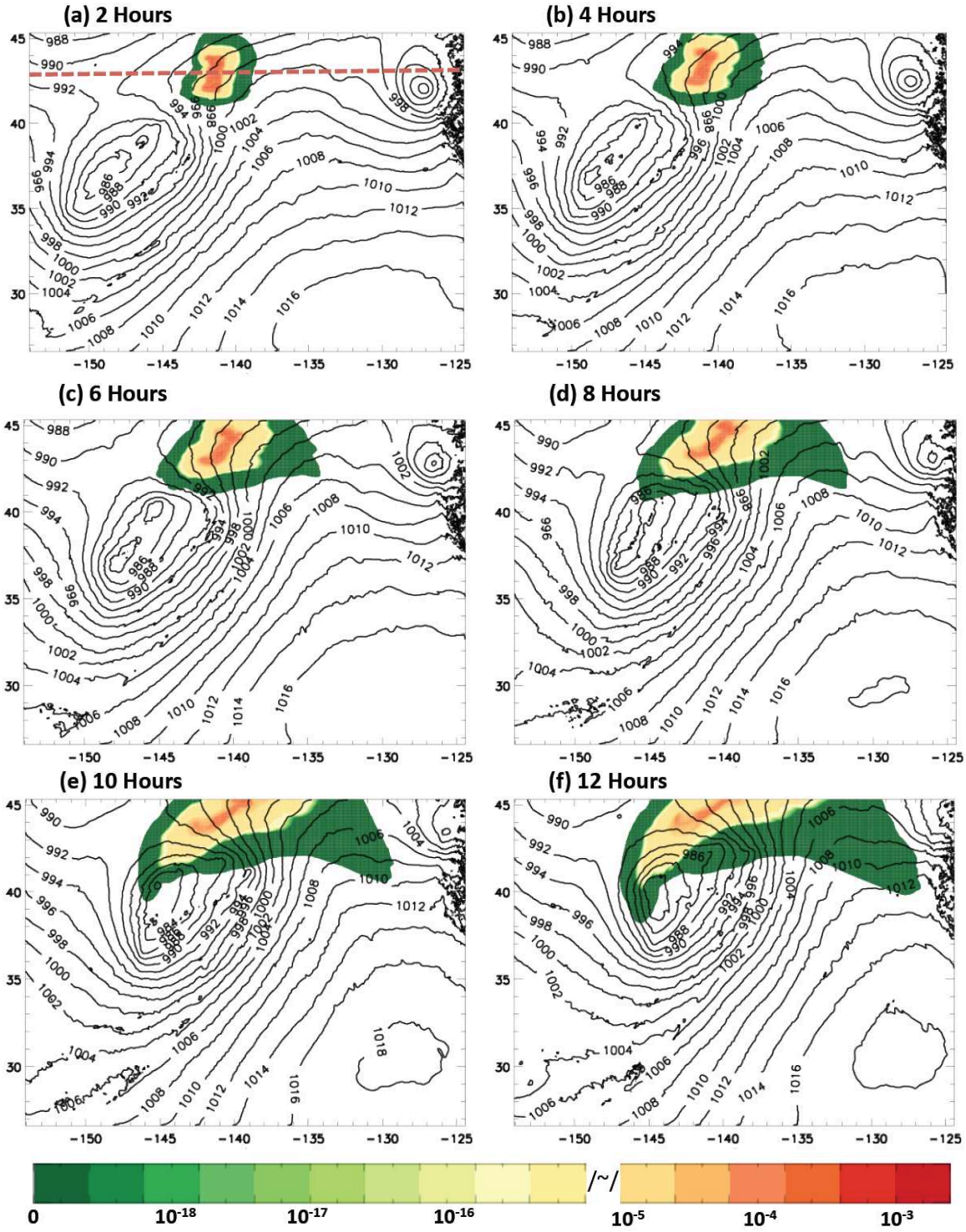

Figure 5.5: As for figure 5.1, but for the W4 tracer. A different contour scale from figure 5.1 has been used.

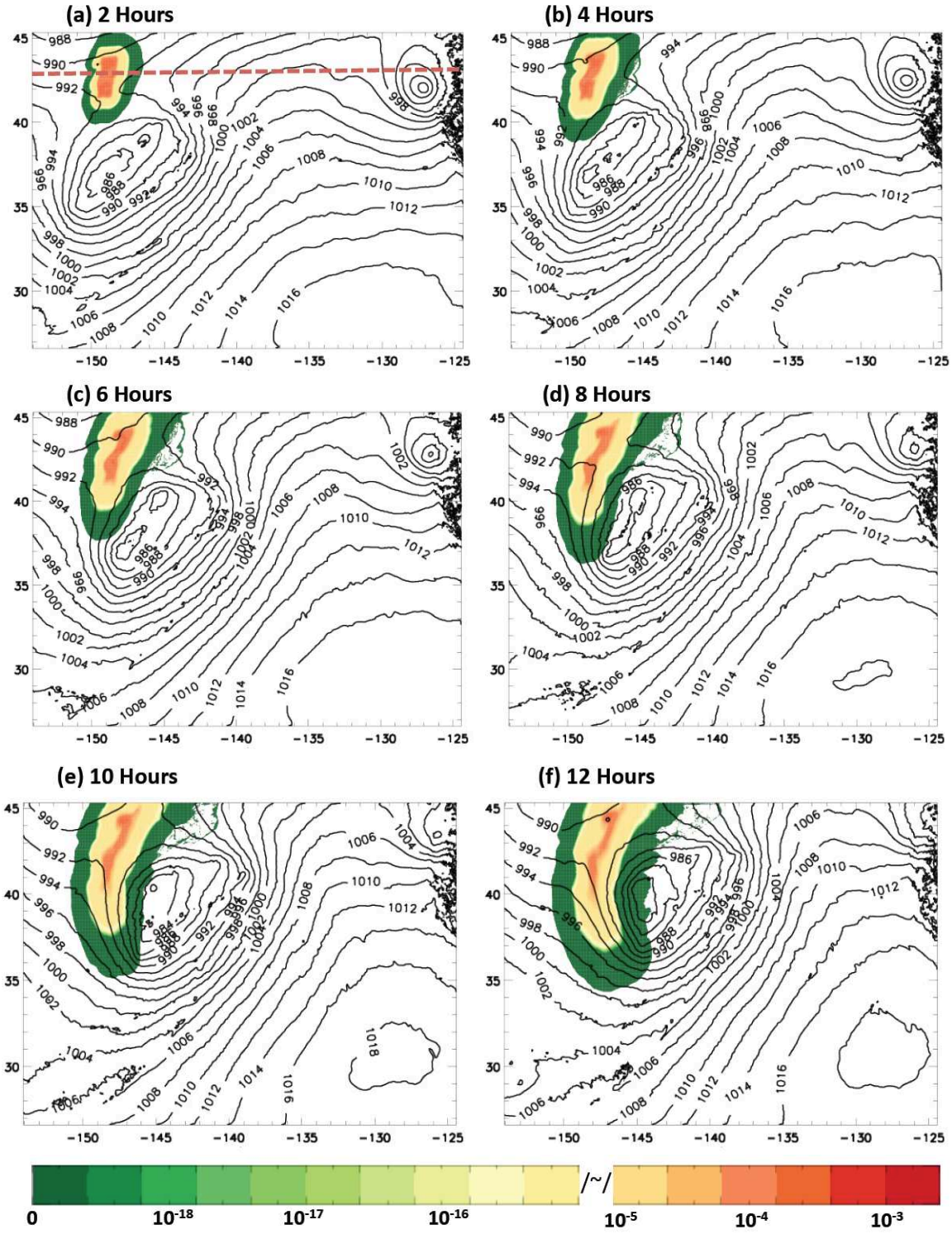

Figure 5.6: As for figure 5.1, but for the TR5 tracer. A different contour scale from figure 5.1 has been used.

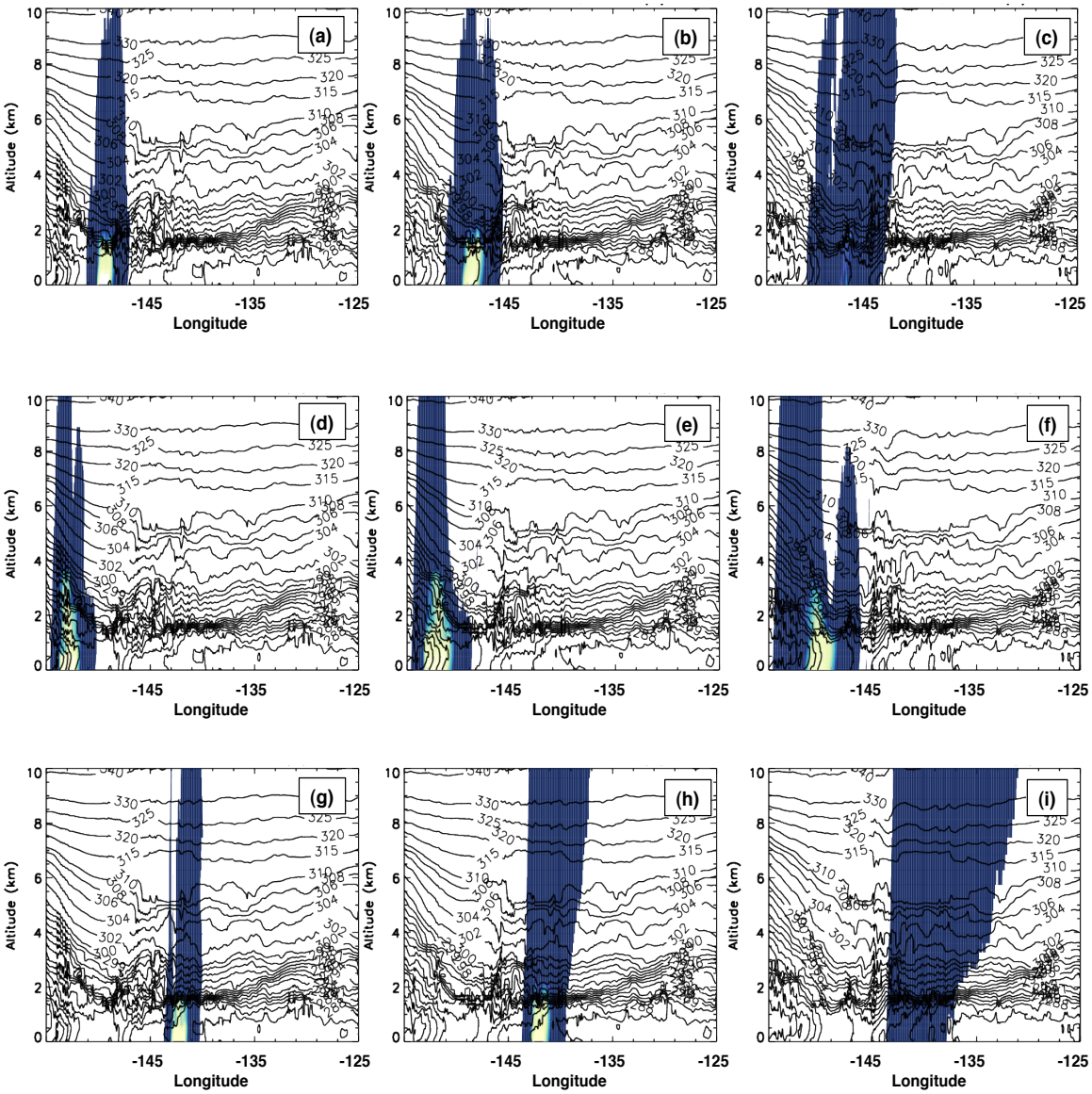
(a)
(b)
(c)
(d)
(e)
(f)
(g)
(h)
(i)
Altitude (km)
Longitude
-145
-135
-125
0
2
4
6
8
10

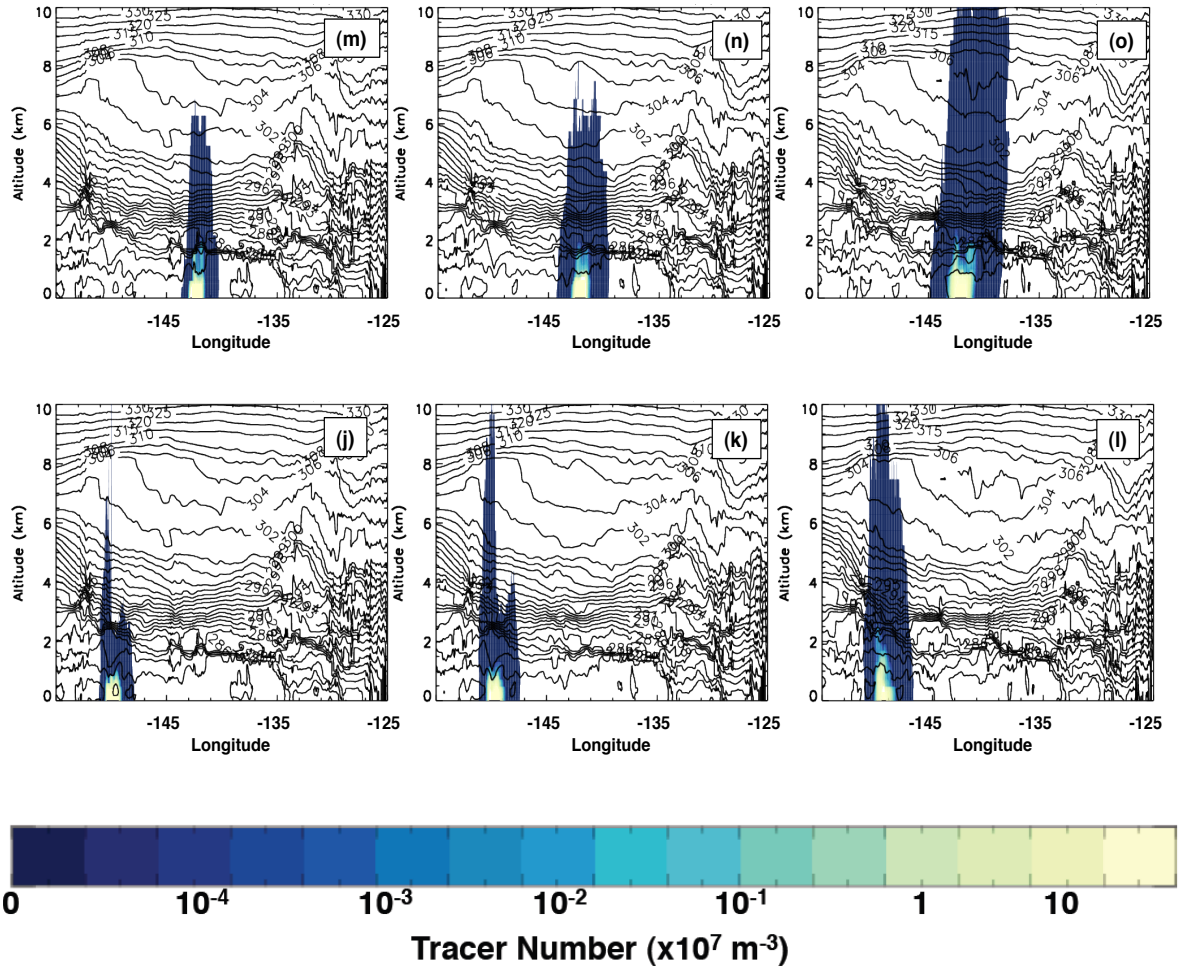

Figure 5.7: East-West cross sections of the (a-c) P1, (d-f) P2, (g-i) W3, (j-l) W4, and (m-p) TR5 tracer number per volume (x 10^7 m^{-3}) at each level (shaded) at 1, 2 and 4 hours after the introduction of the tracers, respectively. The y-axis is altitude while the x-axis is longitude. Black contours are potential temperature (K). The cross sections locations are marked on panel (a) of figures 5.1-5.2, 5.4-5.6.

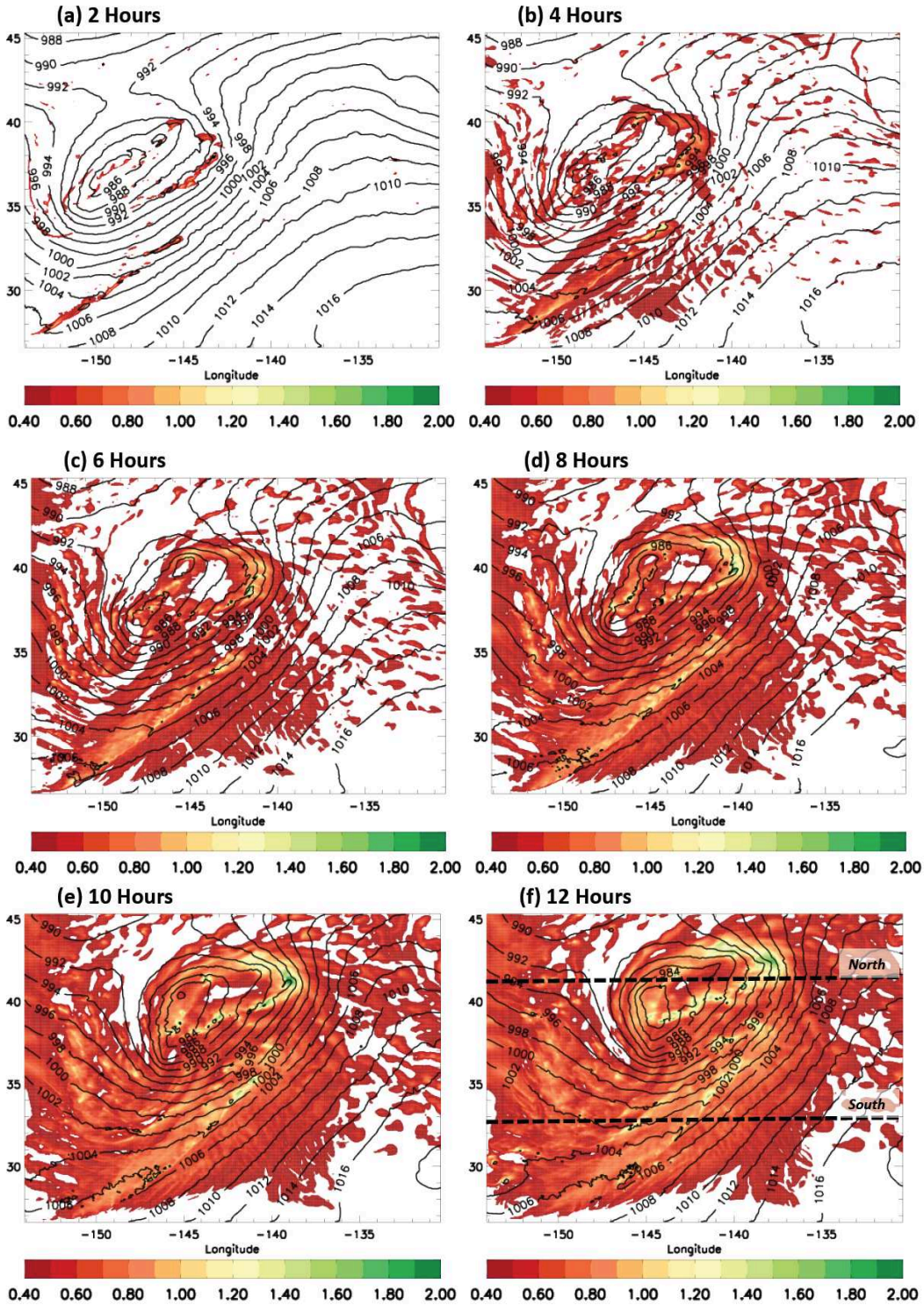

Figure 5.8: Horizontal plan view of vertically integrated number (x 10^{19}) of SFC-TRACER from the CL simulation in each atmospheric column at each grid point (shaded) with sea level pressure (thin black contour, hPa) (a) 2, (b) 4, (c) 6, (d) 8, (e) 10, and (f) 12 hours after introduction of the tracer. Dashed lines on panel (f) are the cross section locations in figure 5.9.

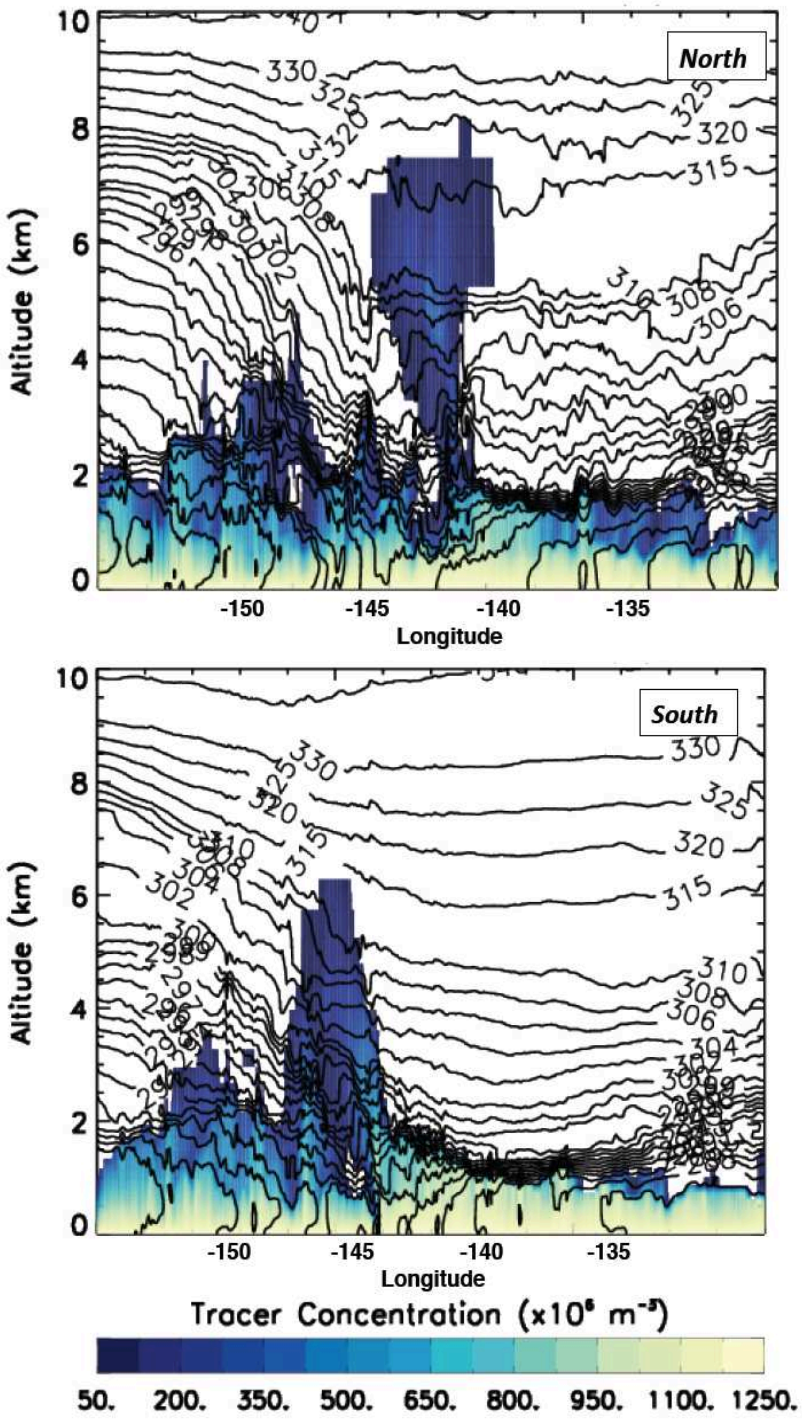

Figure 5.9: West-East cross-sections of the SFC-TRACER tracer number per volume (x 10^6 m^{-3}) at each level (shaded) at 12 hours after introduction of the tracers from the CL simulation. Black contours are potential temperature (K). The cross section locations (North, South) are marked on figure 5.8(f).

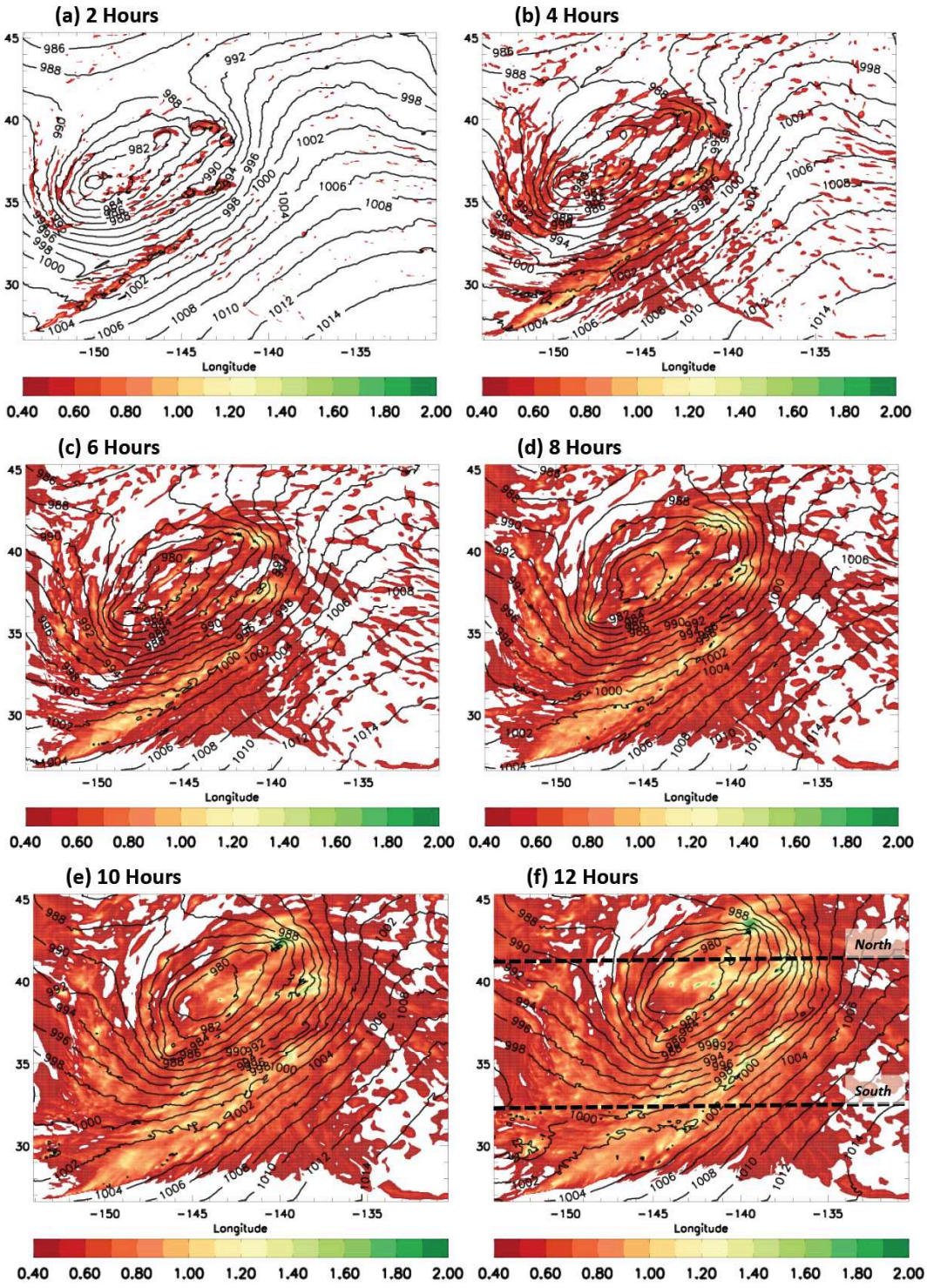

Figure 5.10: As for figure 5.8, but for the +2KCL simulation. Dashed lines on panel (f) are the cross section locations in figure 5.11.

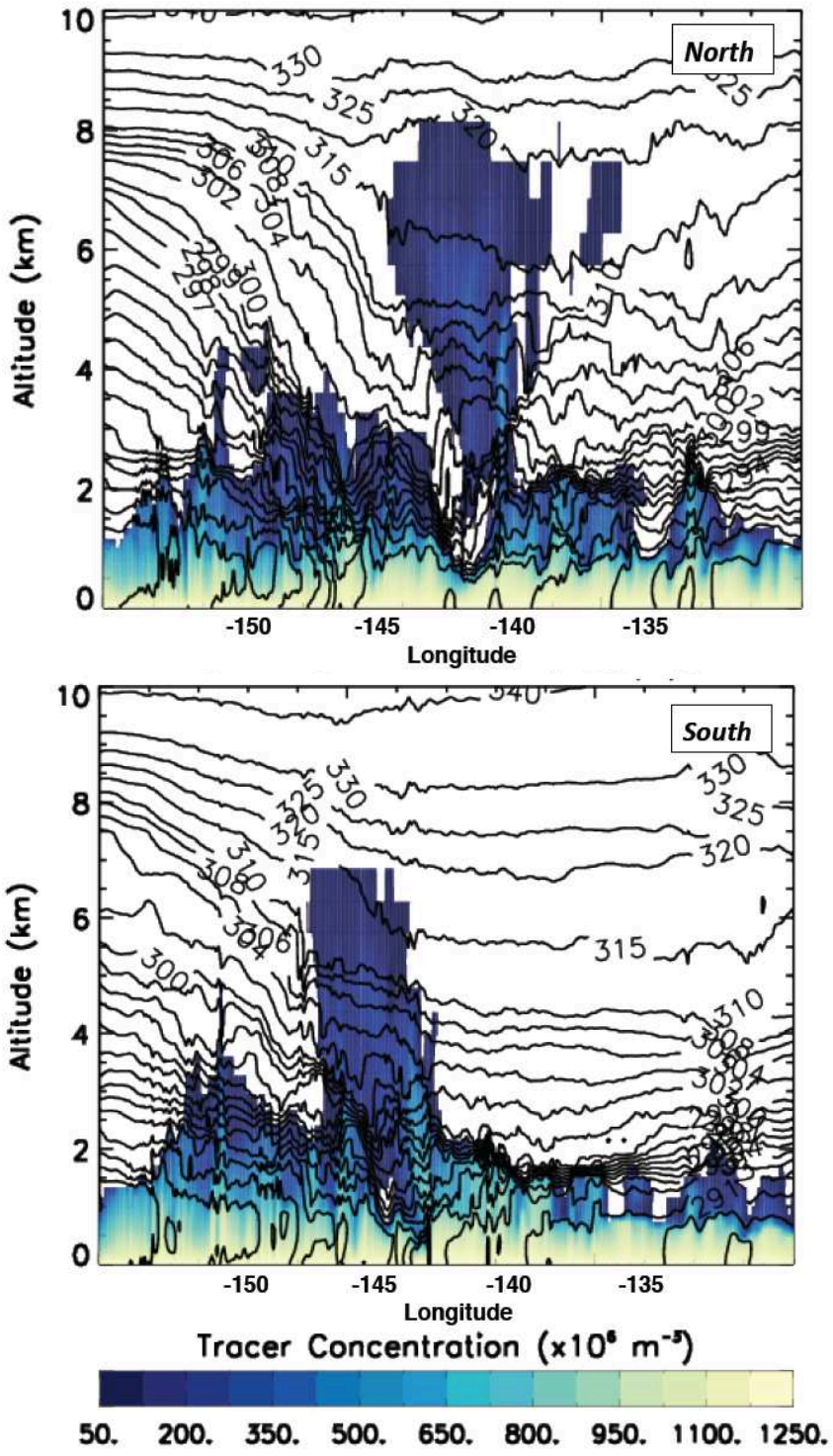

Figure 5.11: As for figure 5.9, but for the +2KCL simulation. The cross section locations (North, South) are marked on figure 5.10(f).

6. CONCLUSIONS

ETCs play a major role in the Earth's global moisture and energy budget, and are a major control of mid-latitude weather and climate. Our ability to forecast regional weather and climate is in part dependent on our understanding of ETCs. Recent studies (e.g. Field and Wood 2007) have found that ETCs in future climates may be fewer in number but more intense and storm tracks may shift. These changes will have large impacts on society, including hydrological and natural resources. Past research has focused not only on the synoptic scale features of ETCs (such as the WCB), but also on the mesoscale features, which can impact ETC development through latent heating and potential vorticity development (e.g. Posselt and Martin 2004). Climate models struggle to accurately represent the features of ETCs, in part due to representation of mesoscale and cloud scale processes (e.g. Ceppi et al. 2012). Here, we have shown the importance of considering the complex cloud scale processes with high spatial and temporal resolution simulations of an ETC.

Recent work has focused on the role of air-sea interactions and the BL in ETC dynamics (B10, B11). These studies produced a new conceptual model that included: (1) convergence from other ETC sectors to the WCB source region and (2) the cumulative impact of shallow convective moisture ventilation. Previous work has focused on the WCB as the primary eastward-poleward transporter of moisture by ETCs. But B10 and B11 showed that a boundary layer water vapor source to the WCB is dependent on the sea surface fluxes of the PCF region, and that the cumulus clouds of the PCF region are efficient vertical transporters of water vapor themselves. However, these previous studies used a global model with convective parameterizations and coarse resolutions (0.4^{o} degrees), which are insufficient to capture the

cloud-scale processes associated with the cumulus and cumulus congestus clouds that exist in this region.

In this study we have investigated the role of PCF clouds in the ETC moisture budget using a high temporal and spatial resolution CRM simulation of an ideal case study of a wintertime ETC over the Pacific Ocean. We investigated several science questions within this study including: (1) what are the microphysical, dynamical, and latent heating characteristics of PCF clouds and how do they vary with environmental conditions? (2) what is the impact of SST and cloud nucleating aerosol on the boundary layer ventilation of water vapor in the PCF cloud region of ETCs? and (3) how is water vapor that is ventilated by the PCF region transported throughout ETCs?

In Chapter 3, we analyzed the major PCF cloud characteristics and how they varied with environmental conditions. The major findings of Chapter 3 include the following:

- In the wintertime, maritime ETC simulated here, PCF clouds are primarily cumulus clouds controlled predominately by warm phase processes, although ice processes become more important if the clouds are able to penetrate above the boundary layer.
- The PCF cloud characteristics that determine their impacts on the water vapor field (i.e. updraft speed and precipitation) are highly sensitive to environmental conditions including the strength of frontal inversion, the boundary layer water vapor contents, the SST, and the aerosol loading, although to a lesser extent in the latter case. We defined the PCF boundary layer to include the atmosphere layer below the boundary layer inversion.
- A warm, moist boundary layer overlaid by a strong inversion, such as in PHASE-1, promotes more frequent boundary layer cumulus clouds, and only the strongest clouds can reach the free troposphere.

- Increasing the SST thermodynamically invigorated the PCF cumulus clouds and increased the number of deeper congestus clouds able to access mixed-phase processes; the precipitation rates were also increased.
- Aerosol-induced invigoration and warm rain suppression of PCF clouds is constrained by the shift in PCF cloud fraction between the numbers of precipitating cumulus versus congestus type clouds.

The results of chapter 3 extend the findings of B10 and B11 in terms of the PCF cloud structure, frequency, size, and precipitation rates, all of which will impact how the PCF clouds cumulatively process and redistribute water vapor. Additionally, we demonstrated that these PCF cloud characteristics are highly sensitive to environmental conditions, and in ways that can influence the PCF regional impacts on the vertical and horizontal water vapor distribution. The spatial and temporal variations and changes due to environmental conditions in the PCF cloud structure and cloud field not considered by B10 and B11 emphasize the need to better represent these complex cloud processes in global models. For example, while the environmental conditions of PHASE-1 are more typical of a PCF region (i.e. moist boundary capped by a dry free troposphere due to the dry conveyor belt), the development of a secondary cold front in the latter time periods of ETC development highlights the need to consider distinct environmental changes.

The water vapor budget of the PCF region was then analyzed in Chapter 4 where the following were found:

- The cumulus clouds within the PCF region result in a net positive upward flux of water from the boundary layer to the free troposphere, but most water vapor fluxes are constrained to the boundary layer. Vertical water vapor mass flux is enhanced by

increasing SST and by increasing the concentration of available cloud nucleating aerosol through enhancement of the boundary layer water vapor content in the former case, and the updraft speeds in the latter case.

- The net advection of moisture from the PCF region eastward was found to be primarily dependent on the balance between the surface precipitation rates and the sea surface evaporation source. The precipitation contributions were found to be the largest in magnitude, which together with the horizontal moisture flux divergence led to a drying of the PCF region in time.
- Proportionally less water vapor mass is available for horizontal transport from the PCF region with increasing SSTs due to the large amount of surface precipitation produced by PCF clouds over warmer SSTs, especially in PHASE-1. This effect may have been somewhat offset by the use of interactive SSTs.

Previous studies (B10; B11) examined the ventilation of PCF BL moisture by both the vertical cloud development and through divergence within the BL to other sectors of the ETC. Here we found that the vertical lofting of moisture is dependent on both (1) the cloud structure (cumulus versus congestus) and (2) the production of precipitation, both of which are in turn dependent on the local environmental conditions. The strongest control on the modification of the PCF moisture field was found to be SST, which enhanced the vertical moisture flux by clouds, but also increased surface precipitation rates. This resulted in less moisture advection from the PCF region to the ETC with increased SSTs, although a redistribution of water vapor throughout the boundary layer and to the free troposphere did occur.

Massless, passive tracers released from the surface were utilized to determine how PCF ventilated moisture is transported within an ETC, and how the long range transport of moisture from the PCF region compares to other sectors of the ETC. In Chapter 5, we found:

- PCF lofting of tracers by convection was present, but the majority of the tracers were confined to the boundary layer and were subsequently transported towards the larger-scale lifting features of the ETC.
- The distance behind the cold front of the PCF tracer's initial release determined the magnitude and mechanisms of vertical lofting of the surface based tracers, including more northerly versus southerly transport.
- The tracers released nearest to the primary cold front in the PCF region were lofted in comparable magnitudes to the WCB lofted tracers due to the dynamical motions associated with the ETC occlusion process.
- Increasing SSTs resulted in over 40% more tracers reaching the mid and upper levels of the domain.

While we showed that PCF convective lofting of tracers does occur as in B11, the greatest lofting of tracers released in the PCF region occurs in association with the primary cold front. This highlights the importance of within boundary layer horizontal transport away from the PCF region after the lesser modification of the vertical water vapor distribution in the PCF region. The vertical lofting of tracers away from the surface by PCF clouds but still within the boundary layer is similar to the level of maximum vertical lofting of water vapor shown in Chapter 4. Hence, while water vapor from the PCF region can reach the upper troposphere and achieve larger-scale transport on time scales and quantities similar to the WCB, there is a dependence on lofting mechanisms away from the PCF region to get above the boundary layer.

In summary, we have analyzed the development of PCF clouds and their role in the ETC water vapor budget. While previous studies (B10; B11) focused on the interaction of the boundary layer within different sectors of an ETC, they were limited by the use of a global model at coarse resolutions. Here, we have investigated the cloud microphysical and dynamical mechanisms responsible for PCF cloud processing of water vapor, including the features that impact vertical and horizontal water vapor mass flux at a cloud process scale. We highlighted that while vertical transport away from the surface is occurring in the PCF region, lofting into the free troposphere within the PCF region is small and counterbalanced by precipitation. Instead, larger scale lofting mechanisms are needed for long-range transport and to achieve lofting comparable to the WCB. We have also shown the role played by environmental conditions in determining the magnitude of these fluxes. While some environmental characteristics can increase the vertical flux of moisture, similar microphysical mechanisms can also enhance precipitation, a sink of water vapor. As Earth's climate is changing, improvements in representing cloud scale processes within global models is needed to accurately represent cloud development, their vertical and horizontal distribution, and impacts on and by the atmospheric thermodynamics. Lastly, we have shown the SST impacts on PCF cloud development to be greater than that of aerosol loading for the PCF region examined here. While this is a function of the sensitivity parameters chosen here, we have highlighted the importance of considering the thermodynamical conditions impact on PCF cloud and regional development and not just the variation in cloud updraft such as through aerosol indirect effects.

7. REFERENCES

Albrecht, B. A., 1989: Aerosols, cloud microphysics, and fractional cloudiness. *Science*, **245**, 1227-1230.

Arnold, F., J. Schneider, K. Gollinger, H. Schlager, P. Schulte, D. E. Hagen, P. D. Whitefield, and P. van Velthoven, 1997: Observation of upper tropospheric sulfur dioxide- and acetone-pollution: Potential implications for hydroxyl radical and aerosol formation. *Geophys. Res. Lett.,* **24,** 57–60.

Barnes, E. A and L. Polvani, 2013: Response of the Midlatitude Jets, and of Their Variability, to Increased Greenhouse Gases in the CMIP5 Models. *J. Climate*, **26**, 7117–7135.

Baldwin, D., E.-Y. Hsie, and R. A. Anthes, 1984: Diagnostic studies of a two-dimensional simulation of frontogenesis in a moist atmosphere. *J. Atmos. Sci.,* **41,** 2686–2700.

Bengtsson, L., K. I. Hodges, and E. Roeckner, 2006: Storm tracks and climate change. *J. Climate,* **19**, 3518–3543.

Bengtsson, L., K. I. Hodges, and N. Keenlyside, 2009: Will extratropical storms intensify in a warmer climate?. *J. Climate*, **22**, 2276–2301.

Berger, B. W., & C. A. Friehe, 1995: Boundary-layer structure near the cold front of a marine cyclone during ERICA. *Boundary-Layer Meteorology*, **73(3)**, 227-253.

Bjerknes, J., & H. Solberg, 1922: *Life cycle of cyclones and the polar front theory of atmospheric circulation*. Grondahl.

Bond, N. A., & R. G. Fleagle, 1988: Prefrontal and postfrontal boundary layer processes over the ocean. *Monthly Weather Review*, **116(6),** 1257-1273.

Boutle I. A., R.J. Beare, S. E. Belcher, A. R. Brown, R. S. Plant, 2010: The moist boundary layer under a midlatitude weather system. *Boundary-Layer Meteorol.* **134**, 367–386.

Boutle, I. A., S. E. Belcher, and R. S. Plant, 2011: Moisture transport in midlatitude cyclones. *Q.J.R. Meteorol. Soc.,* **137**, 360–373.

Browning, K. A., 1971: Radar measurements of air motion near fronts. *Weather*, **28**, 320-340.

Browning, K. A., 1986: Conceptual models of precipitation systems. *Weather and Forecasting*, **1**(1), 23-41.

Browning, K. A., 1997: The dry intrusion perspective of extra-tropical cyclone development. *Meteorological Applications*, **4(04),** 317-324.

Browning, K. A., N. M. Roberts, and A. J. Illingworth, 1997: Mesoscale analysis of the activation of a cold front during cyclogenesis. *Q.J.R. Meteorol. Soc.,* **123**, 2349–2374.

Carlson, T. N., 1980: Airflow Through Midlatitude Cyclones and the Comma Cloud Pattern. *Mon. Wea. Rev.*, **108**, 1498–1509.

Catto, J. L., L. C. Shaffrey, and K. I. Hodges, 2010: Can Climate Models Capture the Structure of Extratropical Cyclones?. *J. Climate*, **23**, 1621–1635.

Catto, J. L., C. Jakob, G. Berry, and N. Nicholls, 2012: Relating global precipitation to atmospheric fronts, *Geophys. Res. Lett.,* **39**, L10805.

Ceppi, P., Y-T. Hwang, D. W. Frierson, and D. L. Hartmann, 2012: Southern hemisphere jet latitude biases in CMIP5 models linked to shortwave cloud forcing. *Geophys., Res. Lett.*, **39**, L19708.

Chang, C. B., D. J. Perkey, and C. W. Kreitzberg, 1982: A numerical case study of the effects of latent heating on a developing wave cyclone. *J. Atmos. Sci.,* **39,** 1555–1570.

Cotton, W. R., and Coauthors, 2003: RAMS 2001: Current status and future directions. *Meteor. Atmos. Phys*., **82**, 5–29.

Cotton, W. R., G. D. Alexander, R. Hertenstein, R. L. Walko, R. L. McAnelly, and M. Nicholls, 1995: Cloud venting—A review and some new global annual estimates. *Earth Sci. Rev.,* **39,** 169–206.

Dacre, H. F., P. A. Clark, O. Martinez-Alvarado, M. A. Stringer, and D. A. Lavers, 2015: How do atmospheric rivers form?. *Bull. Amer. Meteor. Soc.*, **96**, 1243–1255.

Davis, C. A., 1992: A potential vorticity analysis of the importance of initial structure and condensational heating in observed cyclogenesis. *Mon. Wea. Rev.,* **120,** 2409–2428.

Dudhia, J.,1993: A nonhydrostatic version of the Penn State–NCAR mesoscale model: validation tests and simulation of an atlantic cyclone and cold Front. *Mon. Wea. Rev.*, **121**, 1493–1513.

Eckhardt, S., A. Stohl, H. Wernli, P. James, C. Forster, and N. Spichtinger, 2004: A 15-Year climatology of warm conveyor belts. *J. Climate*, **17**, 218–237.

Fan, J., L. R. Eung, P. J. DeMott, J. M. Comstock, B. Singh, D. Rosenfeld, J. M. Tomlinson, A. White, K. A. Prather, P. Minnis, J. K. Ayers, and Q. Min, 2014: Aerosol impacts on California winter clouds and precipitation during CalWater 2011: local pollution versus long-range transported dust. *Atmos. Chem. Phys.*, **14**, 81-101.

Feser, F., M. Barcikowska, O. Krueger, F. Schenk, R. Weisse, & L. Xia, 2015: Storminess over the North Atlantic and northwestern Europe—A review. *QJRMS*, **141**(687), 350-382.

Feingold, G., and A. J. Heymsfield, 1992: Parameterizations of condensational growth of droplets for use in general circulation models. *J. Atmos. Sci.,* **49**, 2325–2342.

Field P. R., and R. Wood, 2007: Precipitation and cloud structure in midlatitude cyclones. *J Climate*, **20**, 233–254.

Frierson, D. M. W., 2006: Robust increases in midlatitude static stability in simulations of global warming. *Geophys. Res. Lett.* **33**: L24816.

Graff, L. S. and J. H. LaCasce, 2012: Changes in the extratropical storm tracks in response to changes in SST in an AGCM. *J. Climate*, **25**, 1854–1870.

Graff, L. S. and J. H. LaCasce, 2014: Changes in cyclone characteristics in response to modified SSTs. *J. Climate*, **27**, 4273–4295.

Grandey, B. S., P. Stier, T. M. Wagner, R. G. Grainger, and K. I. Hodges, 2011: The effect of extratropical cyclones on satellite-retrieved aerosol properties over ocean. *Geophys. Res. Lett.*, **38**, L13805.

Gutowski W. J., and W. Jiang, 1998: Surface-flux regulation of the coupling between cumulus convection and baroclinic waves. *J. Atmos. Sci.*, **55**, 940–953.

Harrison, E. F., P. Minnis, B. R. Barkstrom, V. Ramanathan, R. D. Cess, and G. G. Gibson, 1990: Seasonal-variation of cloud radiative forcing derived from the earth radiation budget experiment. *J. Geophys. Res.,* **95,** 18 687–18 703.

Hartmann, D. L., 1994: *Global Physical Climatology*. International Geophysics Series, Vol. 56, Academic Press, 411 pp.

Held I. M., B. J. Soden, 2006: Robust responses of the hydrological cycle to global warming. *J. Climate* **19**: 5686–5699.

Heymsfield, A. J., and R. M. Sabin, 1989: Cirrus Crystal Nucleation by Homogeneous Freezing of Solution Droplets. *J. Atmos. Sci.*, **46**, 2252–2264.

Hobbs, P.V., and P. O. G. Persson, 1982: The mesoscale and microscale structure and organization of clouds and precipitation in mid-latitude cyclones, part V: the substructure of narrow cold-frontal rainbands. *J. Atmos. Sci.*, **32**, 280-295.

Hobbs, P. V., T. J. Metjka, P. H. Herzegh, J. D. Locatelli, and R. A. Houze, Jr., 1980: The mesoscale and microscale structure and organization of clouds and precipitation in midlatitude cyclones. Part I: A case study of a cold front. *J. Atmos. Sci.*, **37**, 568–596.

Houze Jr., R. A., and P. V. Hobbs, 1982: Organization and structure of precipitating cloud systems. *Adv. Geophys.*, **24**, 225-315.

Igel, A. L., S. C. van den Heever, C. M. Naud, S. M. Saleeby, and D. J. Posselt, 2013: Sensitivity of warm-frontal processes to cloud-nucleating aerosol concentrations. *J. Atmos. Sci.*, **70**, 1768–1783.

Igel, A.L., and S.C. van den Heever, 2014: The role of latent heating in warm frontogenesis. *Q. J. R. M. S.*, **140**, 139-150.

Inatsu, M., and B. J. Hoskins, 2004: The zonal asymmetry of the Southern Hemisphere winter storm track. *J. Climate*, **17**, 4882–4892.

IPCC, 2013: Climate Change 2013: The Physical Science Basis. Contribution of Working Group I to the Fifth Assessment Report of the Intergovernmental Panel on Climate Change [Stocker, T.F., D. Qin, G.-K. Plattner, M. Tignor, S.K. Allen, J. Boschung, A. Nauels, Y. Xia, V. Bex and P.M. Midgley (eds.)]. Cambridge University Press, Cambridge, United Kingdom and New York, NY, USA, 1535 pp, doi:10.1017/CBO9781107415324.

Johnson, R. H., Rickenbach, T. M., Rutledge, S. A., Ciesielski, P. E., & Schubert, W. H. 1999: Trimodal characteristics of tropical convection. *Journal of climate*, **12(8)**, 2397-2418.

Kaufman, Y. J., D. Tanré, & O. Boucher, 2002: A satellite view of aerosols in the climate system. *Nature*, **419**(6903), 215-223.

Knippertz, P., and J. E. Martin, 2007: A Pacific moisture conveyor belt and its relationship to a significant precipitation event in the semiarid Southwestern United States. *Wea. Forecasting*, **22**, 125–144.

Knippertz, P. and H. Wernli, 2010: A lagrangian climatology of tropical moisture exports to the Northern Hemispheric extratropics. *J. Climate*, **23**, 987–1003.

Kocin, P. J., & L.W. Uccellini, 1990: *Snowstorms along the northeastern coast of the United States, 1955 to 1985* (Vol. 22). American Meteorological Society.

Krishnamurti, T. N., 1968: A study of a developing wave cyclone. *Mon. Wea. Rev.,* **96,** 208–217.

Kuo, Y.-H., M. A. Shapiro, and E. G. Donall, 1991: The interaction between baroclinic and diabatic processes in a numerical simulation of a rapidly intensifying extratropical marine cyclone. *Mon. Wea. Rev.,* **119,** 368–384.

Kuo, H. L., 1974: Further studies of the parameterization of the influence of cumulus convection on large scale flow. *J. Atmos. Sci.* **31**, 1232-1240.

Lewis, E. R., and S. E. Schwartz (Eds.), 2004: Sea Salt Aerosol Production: Mechanisms, Methods, Measurements, and Models, Geophys. Monogr. Ser., vol. 152, AGU, Washington, D. C.

Martin, J. E. and J. A. Otkin, 2004: The Rapid Growth and Decay of an Extratropical Cyclone over the Central Pacific Ocean. *Wea. Forecasting*, **19**, 358–376.

Matejka, T. J., R. A. Houze Jr., and P. V. Hobbs, 1980: Microphysics and dynamics of clouds associated with mesoscale rainbands in extratropical cyclones. *Q. J. R. M. S.*, **106**, 29-56.

Meyers, M. P., Walko, R. L., Harrington, J. Y., & Cotton, W. R. 1997: New RAMS cloud microphysics parameterization. Part II: The two-moment scheme. *Atmospheric Research*, **45(1),** 3-39.

Meehl, G. A., C. Covey, K. E. Taylor, T. Delworth, R. J. Stouffer, M. Latif, B. McAvaney, and J. F. B. Mitchell, 2007: THE WCRP CMIP3 Multimodel Dataset: A new era in climate change research. *Bull. Amer. Meteor. Soc.*, **88**, 1383–1394.

Molinari, J., 1985: A general form of Kuo's cumulus parameterization. *Mon. Wea. Rev.*, **113**, 1411–1416.

Naud, C. M., A. D. Del Genio, M. Bauer, and W. Kovari, 2010: Cloud vertical distribution across warm and cold fronts in CloudSat–CALIPSO data and a general circulation model. *J. Climate*, **23**, 3397–3415.

Naud, C. M., D. J. Posselt, and S. C. van den Heever, 2015a: A CloudSat–CALIPSO view of cloud and precipitation properties across cold fronts over the global oceans. *J. Climate*, **28**, 6743–6762.

Naud, C. M., and B. H. Kahn, 2015b: Thermodynamic phase and ice cloud properties in the northern hemisphere winter extratropical cyclones observed by Aqua AIRS. *J. Climate*, in press.

Neiman, P. J., M. A. Shapiro, E. G. Donall, C. W. Kreitzberg, 1990: Diabatic modification of an extratropical marine cyclone warm sector by cold underlying water. *Mon Weather Rev*, **118**, 1576–1590.

Neiman, P. J., and M. A. Shapiro, 1993: The Life Cycle of an Extratropical Marine Cyclone. Part I: Frontal-Cyclone Evolution and Thermodynamic Air-Sea Interaction. *Mon. Wea. Rev.*, **121**, 2153–2176.

Newton, C. W., and E. O. Holopainen, Eds., 1990: *Extratropical Cyclones: The Erik Palmen Memorial Volume*. Amer. Meteor. Soc., 262 pp.

Posselt, D. J., and J. E. Martin, 2004: The Effect of Latent Heat Release on the Evolution of a Warm Occluded Thermal Structure. *Mon. Wea. Rev.*, **132**, 578–599.

Ralph, F. M., and co-authors, 2015: CalWater field studies designed to quantify the roles of atmospheric rivers and aerosols in modulating U.S. west coast precipitation in a changing climate. *Bull. Amer. Met. Soc.* (in press).

Reed, R. J., A. J. Simmons, M. D. Albright, and P. Unden, 1988: The role of latent heat release in explosive cyclogenesis: Three examples based on ECMWF operational forecasts. *Wea. Forecasting,* **3,** 217–229.

Reeves, H. D., and G. M. Lackmann, 2004: An investigation of the influence of latent heat release on cold frontal motion. *Mon. Wea. Rev.,* **132,** 2864–2881.

Remer, L. A., and co-authors, 2005: The MODIS aerosol algorithm, products, and validation, *J. Atmos. Sci.*, **62(4)**, 947–973.

Reutter , P., H. Su, J. Trentmann, M. Simmel, D. Rose, S. S. Gunthe, H. Wernli, M. O. Andreae, and U. Poschl, 2009: Aerosol- and updraft-limited regimes of cloud droplet formation: influence of cloud particle number, size, and hygroscopicity on the activation of cloud condensation nuclei (CCN). *Atmos. Chem. Phys.*, **9**, 7067-7080.

Ryan, B. F., 1996: On the global variation in precipitating layer clouds. *Bull. Amer. Met. Soc.*, **77**, 53-70.

Saleeby, S. M., and S. C. van den Heever, 2013: Developments in the CSU-RAMS Aerosol Model: emissions, nucleation, regeneration, deposition, and radiation. *J. Appl. Meteor. Climatol.*, **52**, 2601–2622.

Saleeby, S. M., S. R. Herbener, S. C. van den Heever, and T. L'Ecuyer, 2015: Impacts of cloud droplet–nucleating aerosols on shallow tropical convection. *J. Atmos. Sci.*, **72**, 1369–1385.

Salomonson V. V., W. L. Barnes, P. W. Maymon, H. E. Montgomery and H. Ostrow, 1989: MODIS: advanced facility instrument for studies of the earth as a system, *IEEE Trans. Geosci. Remote Sens.*, **27**, 145-153.

Sassen, K., 2002: Indirect climate forcing over the western US from Asian dust storms. *Geophys. Res. Lett.*, **29**(10), 103-1.

Schafler, A., and F. Harnisch, 2015: Impact of the inflow moisture on the evoluation of a warm conveyor belt, *QJRMS*, **141**, 299-310.

Schultz, D. M., 2001: Reexamining the cold conveyor belt. *Mon. Wea. Rev.,* **129,** 2205–2225.

Shapiro, M. A., & Grønås, S. (Eds.),1999: *The Life Cycles of Extratropical Cyclones*. American Meteorological Society.

Sheffield, A. M., S. M. Saleeby, and S. C. van den Heever, 2015: Aerosol-induced mechanisms for cumulus congestus growth, *J. Geophys. Res. Atmos.,* **120**, 8941-8952.

Sinclair, V. A., S. L. Gray, S. E. Belcher, 2008: Boundary-layer ventilation by baroclinic life cycles. *QJRMS*, **134**, 1409–1424.

Smagorinski, J., 1956: On the inclusion of moist adiabatic processes in numerical prediction

models. *Ber. Dtsch. Wetterdienstes,* **5,** 82–90.

Stephens, G. L., 2005: Cloud Feedbacks in the Climate System: A Critical Review. *J. Climate*, **18**, 237–273.

Stewart, R. E., K. K. Szeto, R. F. Reinking, S. A. Clough, and S. P. Ballard, 1998: Midlatitude cyclonic cloud systems and their features affecting large scales and climate. *Rev. Geophys.,* **36,** 245– 273.

Stohl, A., and T. Trickl, 1999: A textbook example of long-range transport: Simultaneous observation of ozone maxima of stratospheric and North American origin in the free troposphere over Europe. *J. Geophys. Res.,* **104,** 30 445–30 462.

Stohl, A., and Coauthors, 2003: A backward modeling study of intercontinental pollution transport using aircraft measurements. *J. Geophys. Res.,* **108**, 1984-2012.

Stoelinga, M. T., 1996: A potential vorticity-based study of the role of diabatic heating and friction in a numerically simulated baroclinic cyclone. *Mon. Wea. Rev.,* **124,** 849–874.

Tao, W. K., Chen, J. P., Li, Z., Wang, C., & Zhang, C. (2012). Impact of aerosols on convective clouds and precipitation. *Reviews of Geophysics*, **50(2).**

Thompson, G. and T. Eidhammer, 2014: A study of aerosol impacts on clouds and precipitation development in a large winter cyclone. *J. Atmos. Sci.*, **71**, 3636–3658.

Tracton, M. S., 1973: The role of cumulus convection in the development of extratropical cyclones. *Mon. Wea. Rev.,* **101,** 573–592.

Trenberth, K. E., 1991: Storm tracks in the Southern Hemisphere. *J. Atmos. Sci.*, **48**, 2159–2178.

Trenberth, K. E., J. M. Caron, D. P. Stepaniak, and S. Worley, 2002: Evolution of El Niño–Southern Oscillation and global atmospheric surface temperatures. *J. of Geophys. Res.*, **107(D8),** AAC-5.

Twomey, S., 1974: Pollution and planetary albedo. *Atmos. Env.*, **8.12**, 1251-1256.

van den Heever, S. C., G. L. Stephens, and N. B. Wood, 2011: Aerosol indirect effects on tropical convection characteristics under conditions of radiative–convective equilibrium. *J. Atmos. Sci.*, **68**, 699–718.

Wang, Y., M. Wang, R. Zhang, S. J. Ghan, Y. Lin, J. Hu, B. Pan, M. Levy, J. H. Jiang, M. J. Molina, 2014: Assess the effects of anthropogenic aerosols on Pacific storm track using a multiscale global climate model. *Proc. Natl. Acad. Sci.*, **111**, 6894-6899.

Wernli, B. H., & Davies, H. C., 1997: A lagrangian‐based analysis of extratropical cyclones. I: The method and some applications. *QJRMS*, **123(538**), 467-489.

Weusthoff, T., and T. Hauf, 2008: The life cycle of convective-shower cells under post-frontal conditions. *QJRMS*, **134(633**), 841-857.

Whittaker, J. S., and C. A. Davis, 1994: Cyclogenesis in a saturated environment. *J. Atmos. Sci.,* **51,** 889–907.

Woodcock, A. H. (1953), Salt nuclei in marine air as a function of altitude and wind force, *J. Meteorol.,* **10(5),** 362–371.

Yin, J. H., 2005: A consistent poleward shift of the storm tracks in simulations of 21st century climate. *Geophys. Res. Lett.,* **32,** L18701.

Zhu, Y., and R. E. Newell, 1994: Atmospheric rivers and bombs. *Geophys. Res. Lett.,* **21,** 1999–2002.